Opto-Electrical properties of the 2DEG at the Conducting Interface of $EuO\text{-}KTaO_3$

MANISH

A thesis submitted for the partial fulfillment of the degree of

Doctor of Philosophy

Institute of Nano Science and Technology (INST) Mohali, Knowledge City, Sector 81, SAS Nagar, Manauli, P.O. 140306, Punjab, India.

Indian Institute of Science Education and Research (IISER) Mohali, Knowledge City, Sector 81, SAS Nagar, Manauli, P.O. 140306, Punjab, India.

May 2023

Dedicated to my family,
friends and teachers
for their endless support
and encouragement

Declaration

The work presented in this thesis has been carried out by me under the guidance of Dr. Suvankar Chakraverty at the Institute of Nano Science and Technology Mohali. This work has not been submitted in part or in full for a degree, diploma or a fellowship to any other university or institute. Whenever contributions of others are involved, every effort has been made to indicate this clearly, with due acknowledgment of collaborative research and discussions. This thesis is a bonafide record of original work done by me and all sources listed within have been detailed in the bibliography.

Manish

Date:

In my capacity as the supervisor of the candidate's Ph.D. thesis work, I certify that the above statements by the candidate are true to the best of my knowledge.

Dr. Suvankar Chakraverty

Institute of Nano Science and Technology, Mohali

Date:

Acknowledgements

Throughout the course of my Ph.D., I have experienced numerous significant life events and transitions. I consider myself blessed to receive unwavering affection, enduring support, and encouragement from several people. Without the help and direction, I received from numerous people, the work that is presented in this thesis would not have been feasible. I would like to take this opportunity to show my gratitude to everyone who has supported me throughout my doctoral journey and has helped to shape my future.

First and foremost, I want to express my sincere gratitude to **Dr. Suvankar Chakraverty**, Associate Professor, Institute of Nano Science and Technology, Mohali, Punjab, India who supervised my thesis. He has the most charismatic personality I have ever encountered, and he is constantly passionate and committed to science and research. His knowledge of the subject, clear vision for carrying out research ideas, and upbeat and enthusiastic attitude made it easy for me to find solutions to all of my work's problems. His advice and our conversations together helped me get through obstacles at work and instilled a drive for the never-ending pursuit of knowledge in me. We will always remember the lab procedures we learned from him since they helped us grow in a very orderly way. He was always an inspiration to me and sparked my desire to learn more and more with his vast knowledge. I couldn't have asked for a greater mentor and advisor for my Ph.D. studies. I will be eternally grateful to him for his priceless advice, unwavering support, and unceasing assistance.

In addition, I would like to thank the members of my thesis and annual review committee, **Dr. Chandan Bera, Dr. Dipankar Mandal, and Dr. Kaushik Ghosh**, for their time, input, wise criticism, and support. I would also like to express my profound gratitude to **Dr. K.M. Rubi**, LANL, NHMFL US, for his insightful scientific discussions, leadership, and assistance with carrying out the experiments at high magnetic field measurement. Also, I would like to thank **Dr. Goutam Sheet** of IISER Mohali for allowing us to use their lab facilities whenever needed.

I also like to express my gratitude to **Dr. Debabrata Patra** and **Dr. Kaushik Parida** for their chats with us about both professional and personal matters during our time at INST.

My sincere thanks to **Director, INST** for providing us great working atmosphere and all the facilities required to complete our tasks during the Ph.D. tenure.

I appreciate the INST Faculty's assistance with learning how to handle instruments, their helpful teaching methods, and our warm interactions throughout class. My study path has been greatly enhanced by the fantastic experience of working with their organising teams for conferences and workshops.

Also at this time, I'd want to express my gratitude to the **INST-Administrative team**, which includes Dr. Mukesh, Mrs. Gurveen Kaur, Mr. Nimesh Kaushik, Mrs. Shweta, Ms. Reena, Mr. Ahuja, Mr. Rajat Chauhan, Mr. Rohit, Mrs. Suman, Mrs. Vibha, and Mr. Paramjeet for all the assistance, love, and attention they provided for me, which made my five years at INST seem to go by quickly. My acknowledgment would be lacking if I didn't bring up the INST non-administrative employees. My sincere gratitude to all of the NPDL-INST guards, gardeners, and others for their love, support, and care. Despite our ongoing interference, they always assisted us, making our time at INST extremely safe and comfortable.

The main reason I chose to major in physics in my higher education is because of my physics teacher, **Mr. Vijay Kumar**, whom I would also want to thank at this time. As a result of how much fun he made learning physics, I made it a point to pursue it early in life and use it to discover more about nature. He was an excellent teacher who enlightened many pupils like me, and I sincerely thank him for his encouragement.

Friends are the ones who can take on all of your burdens and give you fresh energy because the Ph.D. journey is frequently overwhelmed with work. During my time at INST, I had the good fortune to be surrounded by incredibly amazing people who helped me make even more pleasurable during my Ph.D. quest. I want to start by expressing my sincere gratitude to my dear friends Chirag Miglani, Rajat Gandhi, Priyanka Dalal, Komal Gill and so on. They have made it possible for me to conduct my research in the lab peacefully, regardless of unusual life circumstances. For that, I would want to express my sincere gratitude to them. This family would be incomplete without mentioning the other

important members Manish Chahal, Vibhav, Mayank, Ajit and Neeraj who have always been there for me in any situation.

I extend my thanks to my senior lab mates Neha Wadhera, Ruchi Tomar, Nand Kumar and Saveena Goyal for their continuous support and help in my research work during the initial days of my Ph.D. degree. Special thanks to my current lab mates Dr. Amit Vahsisth Anamika, Ripudaman, Anshu, Harsha, Shama, Bibek and Sharmistha for all the help and support during my PhD journey. I am also thankful to all the amazing students of INST, mentioning few of them from sports field are Rakesh, Chirag, Krishnakant, Khalid, Vikas, Devendra, Nand Kumar, Venu, Deepak and many more, for their unparalleled love and support.

In addition to the people, I have encountered professionally, I have also been incredibly fortunate personally, and I am eternally grateful to **Nisha Chahal**, my life partner and the source of my strength. She has been with me since the beginning of my journey and is a person of strong character and disposition. She is the only one who knows it better than I do. She was always a problem-solver for all of my issues, not just someone who would lend me her ears to listen to my worries. Throughout this time working on my Ph.D., her pragmatic approach to conducting research, consistent support, and encouragement greatly aided me. She has supported me throughout my pursuit of a scientific career, and I am eternally grateful to her.

Without a doubt, my entire family has contributed to the person I am today, so I want to thank them all. I consider myself extremely fortunate to have been raised in a family with many inspiring individuals. I have a strong sense of gratitude for my family, especially for my parents **Mr. Balwan Singh** and **Mrs. Murti Devi** who have always supported me, taught me to be an honest person, and inspired me to pursue my destiny and try new things in life. I really feel proud of my father, that despite having an agriculture background, he raised me facing all the difficulties and challenges and made me the person that I am today. They have always been a constant source of love and support for me. My inspiration for the rest of my life will come from their selfless act. Special gratitude to my beloved sister and brothers Monika, Vikas, Mahipal, and Vikrant for their unfailing support and unselfish love, which has helped me become a better and stronger person. Special thanks to my dearest uncle **Multan Singh** for so much of love and care.

He always encouraged and lighten my mind when it comes to understanding some realities in life. Lastly, I thank one and all involved in the completion of this work.

Finally, I ask the Almighty to continue leading me and supplying me with a river of wisdom and power so that I might devote my life to the cause of humanity.

MANISH

Abstract

Oxides are an exciting class of materials with a wide range of fascinating electrical, magnetic and optical properties, promising for constructing multifunctional devices. Till date silicon is the basis of conventional electronic and photovoltaic applications. Recently the interfaces and surfaces of oxide heterostructures have been gaining interest in scientific communities due to a rich variety of emergent phenomena that include the realization of high mobility two-dimensional electron gas, superconductivity, magnetism, ferroelectricity, quantum Hall effect, etc. Recent advances in creating complex oxide heterostructure, interfaces formed between two different transition metal oxides, have heralded a new era of materials and physics research, enabling a uniquely diverse set of coexisting physical properties to be combined with an ever-increasing degree of experimental control.

The heterostructure of oxides can be tuned by various external stimuli but the most effective stimuli are the back gating and light irradiation, where we can even change the state of a system from insulating to conducting. Strontium titanate (STO) is one of workhouses in the emerging technologies based on complex oxide interfaces and hetero-structures. STO has been the centre of attention among various oxides for more than half a century. In this thesis, we focus on a rather new member of the perovskite oxide family, $KTaO_3$ (KTO), which has properties similar to STO but in addition to them, has an order of magnitude higher spin-orbit coupling strength than that of STO. Recently, an unusual 2D superconductivity was found at interfaces between KTO (111) single-crystal substrates and other oxide films including $LaAlO_3$, EuO, $YAlO_3$, and TiO_X.

In the first part of the thesis, we have focussed on the optimization and standardization of the pulsed laser deposition (PLD) system. Thin film growth using PLD hinges on various parameters that decide the composition, structure, quality, and finally the physical properties of the films, interfaces, and superlattices. Here, it is demonstrated that how the growth conditions inside the chamber during the growth can be judged from the outside by combining in-situ and ex-situ techniques.

Further, the highly spin-polarized ferromagnetic semiconductor, EuO has been examined as a potential candidate for spintronics and optoelectronic applications and is chosen as a depositing material on KTO substrate. We optimized the EuO-KTO interface and then studied its opto-electrical properties at different temperatures. We have shown how the

photoconductivity changes with temperature, carrier density, and wavelength of light. In another part, we found up to 3 order changes in conductivity at room temperature when we simultaneously applied the light and electric field. Our results may provide a guideline to achieve higher performance in oxide-based memory devices and optical switches.

Finally, we will also present the high field (60 T) magneto-transport data at the EuO-KTO interface. High amplitude quantum Shubnikov de Hass (SdH) oscillations are observed at different tilt angles. Apart from detailed observation of the electronic properties of the KTO-2DEG, this study demonstrates a possible route of studying quantum transport in 2DEG based on 5d-oxides.

Contents

List of Figures

Chapter 1

Introduction

1.1 Background of Oxide electronics

Oxide thin films, interfaces, and heterostructures are emerging as an alternative to silicon-based conventional metal oxide semiconductor (CMOS) technology. An oxide is a chemical compound that contains at least one oxygen atom and one other element in its chemical formula. Oxides are abundant in nature, starting from granite and glass to ceramics, rust, and chalk. Oxides exhibit various interesting physical properties such as high-temperature superconductivity, colossal magnetoresistance, spin-charge coupling, ferroelectricity, metal-insulator transition, magnetism, and so on. These properties mainly emanate from the choice of the elements and are very sensitive to external stimuli such as light irradiation, electrostatic gate, magnetic field, etc., offering several routes to control and engineer functionalities for technological applications [1,2].

Among other forms of oxides, perovskite oxides with the chemical formula ABO_3 has received much attention in the last decade and appear as potential candidates for next-generation oxide electronics. Perovskite oxides have a simple cubic structure with B-atom sitting at the center of an octahedron of oxygen anions and A-atom at the unit cell corners, as depicted in **Fig. 1.1.**

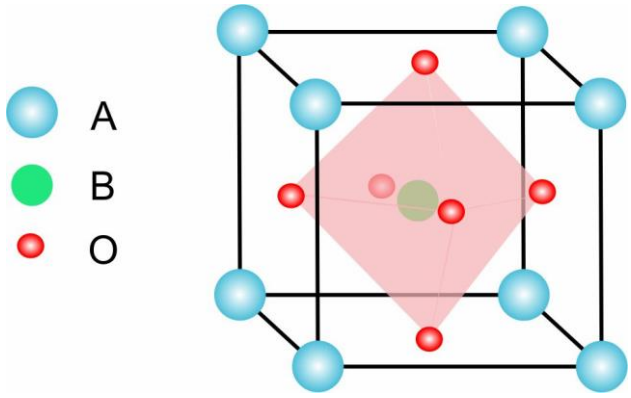

Figure 1.1: Crystal structure of ABO_3 perovskite oxide unit cell. The large A blue atoms at the corners are Rare-earth or alkali ions, the small B green atom at the center is a transition metal ion and the red face-centered O atoms are the oxygen ions.

The ideal cubic structure of these compounds is stable only within a minimal range of ionic radii. It undergoes different type of symmetry-lowering distortions depending on the size of the A and B cations. The rich properties in perovskite oxides originate from the strong correlation between spin, charge and orbital degrees of freedom of d-electrons of the transition metal ions. Further, when the interface and superlattices of these perovskite oxides are formed, they give rise to new or integrated physical properties that could be useful for future-generation spin-electronics devices. In 1994, pre-growth treatment on $SrTiO_3$ (STO) was done by M. Kawasaki, which was a big step forward toward the perovskite oxide thin-film technology [3]. Another phenomenal breakthrough came in this field of oxide in 2004, when conducting interface was realized at the interface of two insulating oxide materials, namely $LaAlO_3$ (LAO) and $SrTiO_3$ [4]. After this discovery, several interfaces have been explored that are found potential for application in spintronic devices [5-9]. Oxide thin films and interfaces are further fascinating compared to their bulk form because it gives the freedom of tailoring the physical properties through lattice deformation, electronics and structural reconstruction [10-13]. An electron moving in an electrical field experiences an effective magnetic field which acts on the electron magnetic moment (spin). The interaction of electron magnetic moment with the effective magnetic field is called the spin-orbit interaction. There are two distinguished classes of effects, which are originated from the spin-orbit interaction are: class 1: the enhancement of the external magnetic field. The effect cause by this are perpendicular magnetic anisotropy, magnetostriction, g-factor and fine structure. Localized electrons and atoms of atomic gas experience this class of effects. Here the time-inverse symmetry is broken by external magnetic field.class2: creation of spin polarization by an electrical current. The effects in this class are 1. Spin-Hall effect 2. Inverse spin Hall effect 3. Spin relaxation. Conduction electrons experience this class of effects. Here the time inverse symmetry is broken by the electrical current. Breaking of orbital symmetry and time inverse symmetry are two critical factors, which determines the magnitude of the spin orbit interaction. So, designing and stabilizing suitable perovskite oxide thin films, interfaces and superlattices are extremely important for the next generation of oxide-based spin electronics and optoelectronics. In the next section, we will discuss the importance of thin film and how we can design a highly epitaxial crystalline thin film for device applications.

1.2 Thin Film Technology for Optoelectronics

Thin-film technologies are processes for depositing and processing thin layers of materials ranging from a few microns thick down to individual atomic layers. They surround us in our everyday lives: memory chips and processors on silicon wafers for modern microelectronics, anti-reflective coatings on glasses, antibacterial metal coatings on medical devices, flexible solar cells, or even layers for food packaging and medicines on miles of foil, etc. are a few examples of the same. Advances in thin-film growth techniques result in an extended list of applications and methods to explore the fundamental properties of the materials. The exciting properties of oxide combined with the advancement in thin film growth techniques like molecular beam epitaxy (MBE) and pulsed laser deposition (PLD) provide an intense research platform for the betterment of oxide-based electronics. Thin-film growth by PLD or MBE gives a wide variety of advantages over bulk counterparts. The atomic-level control of film growths by these techniques helps in the realization of new functionalities of the materials that are absent in their bulk form. Another important property is the possibility to achieve high-quality single-crystal surfaces, which in turn help to realize various surface actuated phenomena and stabilization of high-quality defect-free thin film samples that enable in determining detailed unusual/engineered electronic band dispersion, which is not possible in bulk samples due to the defect associated with the growth mechanism. Stoichiometry during deposition plays a vital role in determining the physical properties of the thin film. These deposition techniques allow us to control the physical properties of the deposited material or interface through the control of the stoichiometry of the deposited films. Another parameter that we can control is the material's crystal structure, that, further controls the thin film's physical properties. This can be done by controlling the epitaxial strain during the growth [14]. PLD has been proven to be a valuable thin film deposition technique for oxide materials with control on the atomic level. The first part of this thesis mainly revolved around the pulsed laser deposition technique. In this optimization process of the PLD chamber, we have demonstrated how the exact growth conditions inside the chamber during the growth can be judged from the outside without disturbing the chamber's vacuum. In addition, we have demonstrated how thin film growth using PLD hinges on various parameters that decide the composition, structure quality and finally, the physical properties of the film.

1.3 Materials

For the investigation and identification of interface effects in heterostructures, it is important to know the bulk properties of the constituting materials. So, in the subsection of this part of the thesis, we will mainly discuss all the essential oxides used in the experiments. In the optimization and standardization experiment of the PLD chamber, we have taken two different systems STO-STO interface and the $LaVO_3$ (LVO)-STO interface, as a case study. For the electrical and optical tuning experiment, we have used the EuO-KTO interface. So, we will briefly introduce all these perovskite and non-perovskite oxide materials such as STO, KTO and EuO. Finally, we will discuss the conducting interface of europium oxide (EuO) and potassium tantalate oxide (KTO). EuO is one of the ferromagnetic insulating oxide materials. KTO is an interesting material that has high spin-orbit coupling strength and high dielectric constant. KTO is now considered a new kid for the oxide-based spintronics devices with many rich properties that could be the building block element for the oxide electronic industry.

1.3.1 Strontium Titanate Oxide ($SrTiO_3$)

STO plays an essential role as a standard substrate for many oxides material and has been well-investigated during the past decades. It is possible to grow perovskite oxides exhibiting colossal magnetoresistance, high-temperature superconductors [15], or ferroelectrics epitaxially on STO due to the similar lattice constant and structure. In this thesis, STO has been used in the standardization and optimization of the PLD system with respect to the growth temperature and laser fluence. A homoepitaxial growth of STO thin film on STO has been chosen as the first deposition in the chamber. STO is cubic at room temperature (space group $Pm\bar{3}m$) with a lattice constant of 3.905 A°. The TiO_6 octahedra have a perfect 90° angle. Stoichiometric STO has a large indirect bandgap of 3.25 eV. Therefore, it can be viewed as a band insulator or semiconductor. STO does in fact have a lattice constant and structural similarity with a number of other significant oxides, enabling epitaxial growth. It is also chemically inert, and it typically does not interact with the materials that have been deposited on it. An insulating STO can be doped into a superconducting state by introducing oxygen vacancies [16, 17] or doping a suitable material [18-20]. In single crystals or even thin films, the oxygen vacancy concentration can be precisely regulated. Oxygen deficiency in STO single crystal can be easily generated in different ways, such as either by heating to more than nearly 800° C in low

oxygen partial pressure ≤ 10^{-6} mbar or by high-energy ion bombardments. STO has interesting dielectric properties. It is an incipient ferroelectric [21] and remains paraelectric for T = 0 K. It can be used as a gate dielectric material in field effect setups due to its high dielectric constant. One of the exceptional properties of the STO is that it can be grown easily on Si [22]. This makes easy to integrate oxide-based devices into the microelectronics industry. Under stress or change of temperature, the STO lattice can deform from the ideal cubic structure. The most relevant distortions for STO are: 1. Ferroelectric type (FE) displacement: polar displacement between cations and anions, resulting in a built -in polarization. 2. Antiferrodistortive (AFD) rotation: antiphase rotation of neighbouring oxygen TiO_6 octahedra. Perovskite with larger tolerance factor (t >1), such as t =1.063 for $BaTiO_3$ favor FE displacement and are often found to be ferroelectric. On the other hand, perovskite with smaller (t <1), such as t=0.946 for $CaTiO_3$, favor AFD rotation. The tolerance factor for STO is nearly close to 1. So, it is not surprising that both FE and AFD are relevant in phase diagram of STO. STO is one of the few known systems to exhibit quantum paraelectricity-a phase in which quantum fluctuations between degenerate lower symmetry configuration supress ferroelectric ordering. At room temperature, the static dielectric constant of STO is large nearly 300. As the temperature decreases, this value increases and saturating at 14 K, and can be as large as 30000 depending on strain, field and sample quality. While the bulk of STO is paraelectric, the surface can be ferroelectric. It has a direct band gap of 3.75 eV. Upon introduction of oxygen vacancies, the color of STO changes from transparent to blue. Upon the application of an electric field at elevated temperature, the oxygen vacancies migrate, resulting in a gradient of color. STO was the first complex oxide found to be superconducting.

1.3.2. Europium Oxide (EuO)

For optoelectronic applications, EuO has led a milestone due to the strong interaction of light with its magnetic properties [23]. The enrichment of Eu in EuO also adds many exciting properties like the transition of semiconducting to metallic behavior at the temperature where the magnetic transition occurs [24]. EuO is a highly spin-polarized ferromagnetic semiconductor with potential application in future spintronic devices. EuO (europium oxide) crystallizes in a NaCl structure with a lattice constant of 5.14 A° at room temperature [25], which reduces to 5.127 A° below 10 K. EuO consists of the rock

salt crystal structure, which is characterized by alternating europium and oxygen atoms in each of the three dimensions on a face center cubic (FCC) lattice as shown in **Fig. 1.2**. Because it is not as densely packed as an FCC lattice, europium metal adopts the body center cubic (BCC) crystal structure. The FCC europium sub lattice's tighter packing results in a larger density of europium atoms in EuO than in Eu metal, despite the presence of oxygen atoms taking up space.

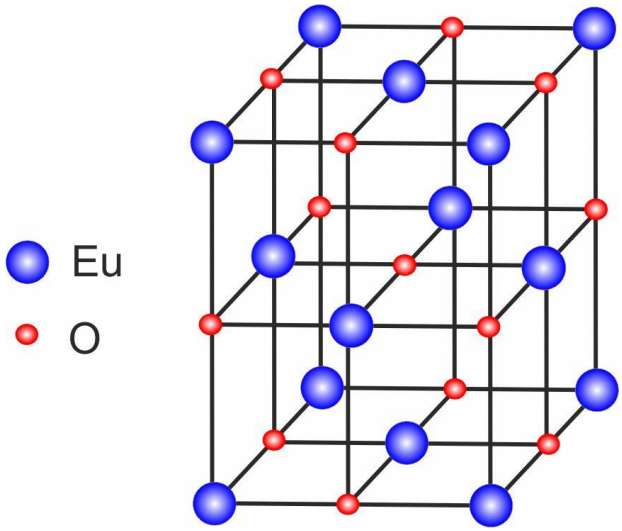

Figure 1.2: Crystal structure of EuO single-crystal unit cell showing the cubic symmetry of its rock salt structure.

Bulk EuO is formed either by melting together EuO and Eu_2O_3 [26,27] or by reducing Eu_2O_3 at a temperature of 1500 °C in a hydrogen environment. High oxygen flow control and deposition rate are essential for EuO thin film deposition. It was shown that EuO films could be obtained by reactive evaporation of Eu metal at a low oxygen pressure while heating the substrate to nearly 400 °C [28]. It is crucial to prepare and preserve the samples under ultra-high vacuum conditions because of the reactive nature of Eu atoms with oxygen or water to form Eu_2O_3 or $Eu(OH)_3$. But with the advancement in the thin film deposition technique, many groups have successfully grown the stable thin film of EuO using MBE or PLD [13,29,30]. EuO has an ionic Eu^{2+} O^{2-} character, such that the electronic configuration of europium is [Xe] $4f^7$ $5d^0$ $6s^0$ and that of oxygen is $1s^2$ $2s^2 2p^6$. Two electrons moved from the 6s orbital of Eu metal to the p orbital of the oxygen atom, which makes Eu^{2+} and O^{2-} atoms and also is the origin of its insulating nature. The magnetic properties of EuO are due to the presence of unpaired electrons in the 4f orbital of the Eu atom. EuO possesses 1.1 eV of the energy bandgap [31]. The optical characteristics of EuO, which may be altered by adding a magnetic field or lowering the

temperature, are used to examine the electronic structure. The transition of the 4f orbital optical spectrum contains a gap of 1.15 eV across the conduction band due to the transition from the 4f orbitals to the 5d 6s. The refractive index n of EuO is reduced by the temperature at the absorption edge.

Stoichiometric EuO is ferromagnetic below the curie temperature of T_c = 69.3 K. This transition temperature can be increased by various methods such as electron doping, biaxial strain to heteroepitaxial EuO thin films by underlying substrates. A model system for electron doping in EuO is substitution of Eu^{2+} by Gd^{2+}, thereby one 5d electron is provided. In a similar way, the curie temperature could be increased by La doping up to 200K due to comparable effects. Extra electrons are also provided by oxygen vacancy sites in EuO_{1-X}. For an oxygen vacancy one Eu ion provides two conduction electrons to the crystal. Decreasing the lateral lattice parameters of EuO is an ideal method to increase the curie temperature T_C due to enhanced nearest neighbour coupling. EuO brings unique benefits for a possible application as spin functional tunnel contact to silicon. From the electron configuration of EuO $4f^7$, seven unpaired spins are located in the outer shell and lead to l = 0 and s = 7/2. If EuO fully magnetizes, then a saturation moment of M_s = 7 μ_B/f.u. is expected. EuO is a band insulator and considered an ideal Heisenberg ferromagnet, due to the fact that l = 0 and only spin-spin interactions govern the magnetic properties

1.3.3. Potassium tantalate oxide ($KTaO_3$)

In the last few years, $KTaO_3$ (KTO) has attracted researchers' attention due to its various fascinating properties. It has an order of higher magnitude spin-orbit coupling strength compared to STO [32]. High permittivity and less dielectric loss make it a promising candidate for future spintronics devices. KTO can host two-dimensional electron gas(2DEG) with different oxide materials such as LTO/KTO, a-LAO/KTO, LVO/KTO, EuO/KTO [29,33-35], etc. KTO is a typical cubic perovskite with lattice constant a= 3.989 A° at room temperature [36]. It is a polar oxide with an alternating layer of KO and TaO_2 having -1 and +1 charges and remains in the cubic paraelectric phase down to at least 4.2 K [37]. To avoid the polar catastrophe in KTO, M. Setvin *et al*. used scanning probe microscopies and density functional theory to study the changes in the polar surface of this perovskite. They observed several structural reconstructions as the surface cleaved in a vacuum was heated to higher temperatures. Hydroxylation after exposure to water

vapor also stabilized the surface [38]. Bulk KTO is a wide gap insulator with a bandgap of 3.64 eV [39]. The electrical properties of the insulating KTO can be tuned over a wide range by adding impurities or by electron doping which turns KTO to become metallic and even superconducting. Doping KTO with Fe, Mn, Cr and Nb lead to ferroelectric and magnetic properties with different transition temperatures [40-42]. KTO is a quantum paraelectric, i.e., it does not show a ferroelectric phase transition even at shallow temperatures, as quantum fluctuations prevent the condensation of a low-lying transverse optic mode. Ferroelectricity can be induced in KTO by applying stress as well as by doping or causing defects [43-46]. The simple cubic crystal structure and wide bandgap of KTO make it an exciting candidate for exploring its optical properties. There are reports where people have studied the photo effect on bulk and doped sample of KTO [47-49]. KTO-based heterostructures can be the potential candidate for optoelectronic device applications. Recent studies on Ar+ bombarded KTO and its heterostructures with LVO or EuO have shown that even at room temperature, KTO exhibits large photoconductivity [50-52]. Single crystal of electron doped KTO show good thermoelectric response. KTO dielectric constant values grows to greater than 4500 upon cooling to low temperatures. It was reported that ionic liquid gating could be used to tune the KTO (001) surface into a weak superconducting state with T_C = 47mK. The electronic states near the Fermi level in electron doped KTO are derived from Ta 5d states in particular d_{xy}, d_{zx}, d_{yz} orbitals in the t_{2g} manifold. KTO spin orbit coupling strength (400 meV) is 20 times higher than the STO (17 meV). Owing to the large spin orbit coupling, the interfacial electron gas at KTO (111) interfaces is also expected to host complex spin textures in momentum space.

1.3.4. EuO-KTO interface

As presented before, the bulk properties of both KTO and EuO, the building blocks of the heterostructure, are well known. This section will now introduce the EuO-KTO interface system. The investigation of the observed new effects and properties of this interface, which are not found in the bulk properties of the constituting materials, is the central topic of this work.

The bulk EuO phase crystallizes in a cubic structure with a lattice constant of 5.145 A°. KTO is also cubic with a lattice constant of 3.989 A°. Due to the large lattice mismatch,

epitaxial growth was not possible. So, to get an epitaxial growth on KTO, the EuO lattice will rotate along the (001) axis by 45°, as shown in **Fig. 1.3**.

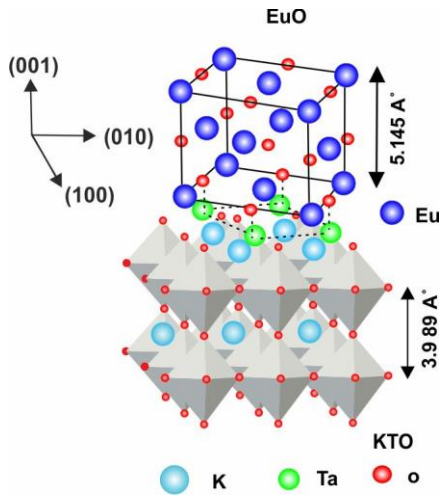

Figure 1.3: Crystal structure of EuO on KTO with 45° rotation along the (001) axis.

The 2DEG at this interface (grown by MBE) was observed for the first time in 2018 by H. Zhang et al. [30]. They found that this 2DEG was highly spin-polarized with Hall mobility of 116.6 cm^2 /Vs at 2 K. They analyze that the magnetic EuO strongly affects KTO, driving the interfacial layer into the ferromagnetic state. This interface shows many interesting properties and was first grown by the PLD system in 2020 by N. Kumar et al. [29]. They reported detecting non-trivial π-Berry's phase in the conducting heterostructure of EuO-KTO via analysis of Shubnikov-de Hass oscillations (SdH) for the first time. KTO-based interfaces are attractive because of all the ingredients of the Rashba system: SOC, relativistic conduction electrons and its polar crystal structure. Later two-dimension superconductivity at this interface (EuO/KTO (111)) was observed with a superconducting transition temperature as high as 2.2 K [13], which is about one order of magnitude higher compared to the well-explored LAO/STO interface. In this thesis, we will report a detail study on the effect of light illumination and electrostatic gate on this interface. We will see how the photoconductivity changes with wavelength at different temperatures for different carrier density samples.

1.4 Tuning interface conductivity using external stimuli

Among the large spectrum of attractive properties and emergent phenomena at oxide heterointerfaces, some of the fascinating properties are tuned upon light illumination, electrostatic gating, external magnetic field, stress, etc. [5, 53-57]. Among them, tuning the conductivity of 2DEG interface using light and electrostatic gating has attracted considerable interest in promising optoelectronic device applications. Light illumination generates electron-hole pairs, which contribute to the conductivity and affect the diffusion of oxygen vacancies and, therefore, significantly modify the transport properties. Similarly, applying an electric field through gating is another method to tune the various physical properties such as band occupation and carrier density, electron mobility, superconductivity, spin-orbit coupling, magnetism, etc. In this thesis, we will be discussing the light effect and combined effect of light and back gate on the EuO/KTO interface.

1.4.1. Effect of light illumination

Light illumination at the oxide interface is one of the powerful external stimuli by which charge carriers can manipulate conductivity. The light-illuminated transport properties revealed fundamental physics for potential application, which has recently attracted a lot of attention [58,59]. Transient photoconductivity (TPC) and persistent photoconductivity (PPC) play an essential role in optoelectronic and memory-based devices. When the system is illuminated with light, its conductivity changes, but after the removal of light, the system does not retain its original state or some persistent photocurrent still remains there, this is termed as PPC. The effect of light on the STO surface showed interesting photo-conductivity properties. STO is a band insulator; when irradiated by light with photon energy higher than 3.25 eV, the insulator-to-metal transition is observed [60]. Above six-order change in resistance is observed at room temperature as shown in **Fig. 1.4 (a).** The annealed STO sample shows a large PPC effect at room temperature, as shown in **Fig. 1.4 (b).** A giant PPC effect was observed at LAO-STO interface in 2012 by Tebano *et al*. [56]. Similarly, an enhancement in the photo-response was observed by Chan et al. using palladium nanoparticles. They found a giant optical switching behavior (750 %) due to the Pd-nanoparticle catalytic effect and surface/interface charge coupling [61]. Because of the similar physical properties and crystal structure, it is expected that

KTO could be one of the promising candidates in the next generation of novel UV photodetectors [62].

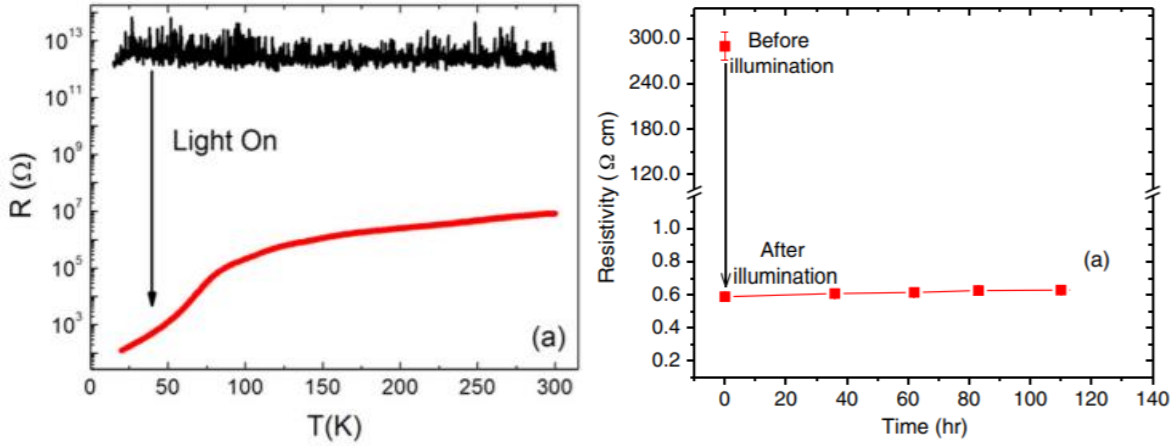

Figure 1.4: (a) The temperature dependence of the resistance of bare STO single crystals with and without light irradiation. (b) The resistivity of the annealed sample before and after illumination.

1.4.2 Effect of electrostatic gate

The oxide-based heterostructure's transport properties and interface conductivity can be tuned by varying the deposition conditions during the growth of the top oxide thin film [63-65]. However, it is also possible to electrostatically modulate the interfacial properties of KTO and STO-based heterostructure by applying an external electric field using a gate. This tuning pathway is of great importance because it is the primary operational principle of most electronic devices available today. The most commonly used configuration for gating is back gating, where KTO or STO substrate serves as a gate dielectric. Other gating configurations are available, such as top gating, ionic liquid gating, and conducting AFM tip on the top of the film [66]. There are issues with this type of top-gating because this can lead to electric breakdown through defects in the gate dielectric, which can further prevent tuning of the charge carrier density and other properties. Thiel et al. are the first to demonstrate the effect of gating on LAO/STO heterostructure. They have shown the possibility of the reproducible bipolar and non-volatile insulator-to-metal transition at room temperature, as shown in **Fig. 1.5** [5].

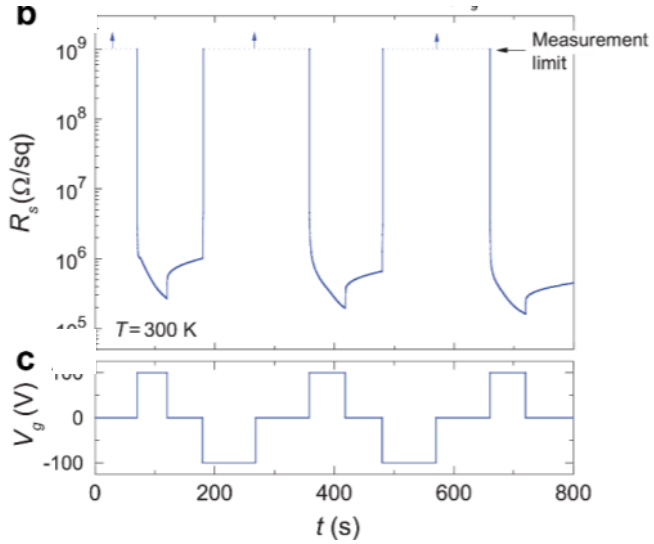

Figure 1.5: The sheet resistance (R_s) of an LAO-STO heterostructure with 3unit cells LAO is changed by more than four orders of magnitude at 300 K upon cycling the back-gate potential (V_g).

After that, many studies have been done to tune this STO-based heterostructure's conducting and insulating interfaces. The newly discovered superconducting LAO/KTO (111) interface has been tuned by back gating at low temperatures. It is observed that carrier density changes by nearly one order of magnitude if voltages sweeps from +150V to -150V [67].

1.4.3 Combined effect of light illumination and electrostatic gate

Light illumination and electrostatic gate are two independent and most commonly used external stimuli to tune the various properties of the oxide heterostructures. Some unusual conductivity changes are observed if both external stimuli are applied simultaneously at the interface. In 2014, Lei et al. were the first to explore LAO/STO heterostructure to see the combined effect of light illumination and electrostatic gate [58]. They observed a giant enhancement in the resistance of the sample when the negative gate voltage was applied under visible light illumination. They found that light illumination decreases rather than increases the carrier density of the gas when the interface was negatively gated through the STO layer, and the density drop was 20 times as large as that caused by the conventional capacitive effect, as shown in **Fig. 1.6.**

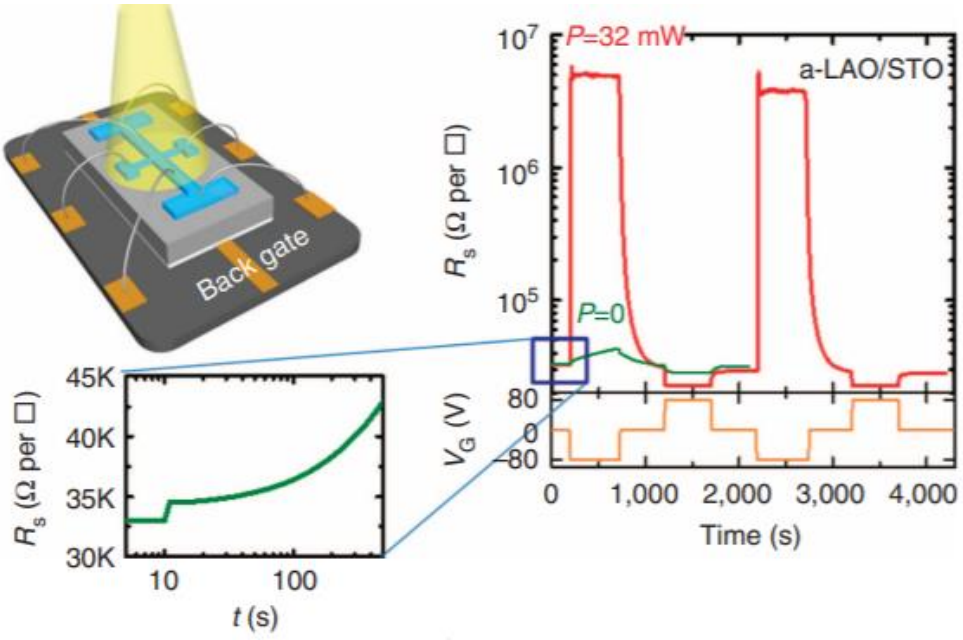

Figure 1.6: Sheet resistance of a-LAO/STO, recorded in the presence/absence of light of power = 32 mW (532 nm) while V_g switches among -80, 0 and 80 V.

Further, the temperature-dependent combined effect at this interface was studied by Yang et al. [68]. Cheng et al. have studied the photo-gating tuning of spin-orbit coupling for the STO-based heterostructure, which opens a pathway to design optically controlled spintronic devices [69]. KTO-based heterostructures are not explored well in terms of the combined effect of light and gate except in a couple of reports. Zhang et al. have studied the effect of optical gating on the amorphous LAO/KTO interface for the first time in 2019 [70]. In this thesis, we have studied the combined effect of light and gate on the EuO/KTO interface that has not been explored so far. We will show how carriers' dynamics change under the combined effect of light illumination and back gating.

1.5 Outlook of the Thesis

One of the central motivations of the thesis is to identify the method to standardize the PLD chamber and prediction of the internal growth condition without breaking the vacuum. Then, we have performed magneto-opto-electrical experiments on the conducting interface of EuO-KTO that may have application in the future optoelectronic and storage devices. **The first chapter** gives a glimpse of the oxide material and the

importance of thin-film technology for future oxide optoelectronic and spintronic devices. It highlights the oxide materials used in different research experiments and gives a brief review of how the tuning of oxide interfaces takes place using light and electrostatic gate as external stimuli. T**he second chapter** describes the various experimental techniques used to carry out the work. It includes the thin film growth by PLD and different characterization techniques such as physical property measurement system (PPMS), Photo Hall measurement setup, Atomic Force Microscopy (AFM), the four-probe cryogenic station for I-V measurement with light, etc. **The third chapter** deals with the optimization and standardization of the PLD system. Here, we will show how a PLD system is optimized and the exact growth condition of that system can be judged from outside using examples of two heterostructure STO on STO and LVO-STO. **The fourth chapter** focuses on the photoconductivity of the EuO-KTO interface. We will demonstrate how the photo-effect changes with the temperature, intrinsic carrier density of the system and wavelength of the illuminated slight. **The fifth chapter** deals with the optical and electrical tuning of the conducting interface of EuO-KTO at room temperature. We will demonstrate how the carrier density of the system changes with the combined effect of light and electrostatic back gate. In **the sixth chapter**, high-field magnetotransport measurement has been done at lower temperatures, where clear quantum oscillations in the magnetoresistance are observed with high amplitude. **The seventh chapter** summarizes the whole work done in this thesis and its future scopes for oxide electronics and optoelectronic devices.

Bibliography

[1]. Y. Tokura and H. Y. Hwang, *Nature Mater.,* **7**, 694 (2008).

[2]. J. Heber, *Nature Mater.,* **459**, 28 (2009).

[3]. M. Kawasaki, K. Takahashi, T. Maeda, R. Tsuchiya, M. Shinohara, O. Ishiyama, T. Yonezawa, M. Yoshimoto and H. Koinuma, *Science,* **266**, 5190 (1994).

[4]. A. Ohtomo and H. Y. Hwang, *Nature*, **427**, 423 (2004).

[5]. S. Thiel, G. Hammerl, A. Schmehl, C.W. Schneider and J. Mannhart, *Science,* **313**, 1942 (2006).

[6]. K. Ueno, S. Nakamura, H. Shimotani, A. Ohtomo, N. Kimura, T. Nojima, H. Aoki,Y. Iwasa and M. Kawasaki, *Nature Mater.,* **7**, 855 (2008).

[7]. K. Ueno, S. Nakamura, S. Shimotani, H. T. Yuan, N. Kimura, T. Nojima, H. Aoki, Y. Iwasa and M. Kawasaki, *Nat. Nanotechnol*., **6**, 408 (2011).

[8]. C. H. Ahn, J. M. Triscone and J. Mannhart, *Nature*, **424**, 1015 (2012).

[9]. H. Y. Hwang, Y. Iwasa, M. Kawasaki, B. Keimer, N. Nagaosa and Y. Tokura, *Nature Mater.*, **11**, 103 (2012).

[10]. H. Guo, R. Zhao, K. J. Jin, L. Gu, D. Xiao, Z. Yang, X. Li, L. Wang, X. He, J. Gu, Q. Wan, C. Wang, H. Lu, C. Ge, M. He and G. Yang, *ACS Appl. Mater. Inter.,* **7**, 2944 (2015).

[11]. Y. Liang, W. Li, S. Zhang, C. Lin, C. Li, Y. Yao, Y. Li, H. Yang and J. Guo, *Scien. Rep.,* **5**, 10634 (2015).

[12]. S. Chakraverty, T. Matsuda, H. Wadati, J. Okamoto, Y. Yamasaki, H. Nakao, Y. Murakami, S. Ishiwata, M. Kawasaki, Y. Taguchi, Y. Tokura and H. Y. Hwang, *Phys. Rev. B*, **88**, 220405 (2013).

[13]. C. Liu, X. Yan, D. Jin, Y. Ma, H.-W. Hsiao, Y. Lin, T. M. Bretz-Sullivan, X. Zhou, J. Pearson, B. Fisher, J. S. Jiang, W. Han, J.-M. Zuo, J. Wen, D. D. Fong, J. Sun, H. Zhou and A. Bhattacharya, *Science*, **371**, 716 (2021).

[14]. Y. Konishi, Z. Fang, M. Izumi, T. Manako, M. Kasai, H. Kuwahara, M. Kawasaki, K. Terakura and Y. Tokura, *J. Phys. Soc. Jpn*., **68**, 3790 (1999).

[15]. P. Chaudhari, R.H. Koch, R.B. Laibowitz, T.R. McGuire, and R.J. Gambino, *Phys. Rev. Lett.*, **58**, 2684 (1987).

[16]. H.P.R. Frederikse, W.R. Thurber and W.R. Holser, *Phys. Rev.*, **134**, A442 (1963).

[17]. W. Luo, W. Duan, S.G. Louie and M.L. Cohen, *Phys. Rev. B*, **70**, 214109 (2004).

[18]. J.F. Schooley, W.R. Hosler and M.L. Cohen, *Phys. Rev. Lett*., **12**, 474 (1964).

[19]. J.F. Schooley, W.R. Hosler, E. Ambler, J.H. Becker, M.L. Cohen and C.S. Koonce. *Phys. Rev. Lett.*, **14**, 305 (1965).

[20]. G. Binnig, A. Baratoff, H.E. Hoenig and J.G. Bednorz, *Phys. Rev. Lett.*, **45**, 1352 (1980).

[21]. K.A. Muller and H. Burkard, *Phys. Rev. B*, **19**, 3593 (1979).

[22]. L. V. Goncharova, D. G. Starodub, E. Garfunkel, T. Gustafsson, V. Vaithyanathan, J. Lettieri and D. G. Schlom, *J. Appl. Phys.*, **100**, 014912 (2006).

[23]. M. W. Shafer, *J. Appl. Phys.*, **39**, 588 (1968).

[24]. O. Massenet, Y. Capiomont and N. Van Dang, *J. Appl. Phys.*, **45**, 3593 (1974).

[25]. D. B. Mcwhan, P.C. Souers and G.Jura, *Physical Review*, **143,** 385 (1996).

[26]. J.Schoenes and P. wachter, *Physical Review B*, **9, 7** (1974).

[27]. O.W. Dietrich, A. J. Henderson and H.Meyer, *Physical Review B*, **12**, 7 (1975).

[28]. O. Massenet, Y. Capiomont and N. Van Dang, *J. Appl. Phys*., **45**, 3593 (1974).

[29]. N. Kumar, N. Wadehra, R. Tomar, Shama, S. Kumar, Y. Singh, S. Dattagupta and S. Chakraverty, *Adv. Quantum Technol.*, **4**, 2000081 (2021).

[30]. H. Zhang, Y. Yu, X. Zhang, H. Zhang, Y. ma, X. Yan, F. Wang, G. Li, R. Li, T. Khan, Y. Chen, W. Liu, F. Hu, B. Liu, B. Shen, W. Han and J. Sun, *Phys. Rev. Lett*., **121**, 116803 (2018).

[31]. P. Wachter, Handbook on the Physics and Chemistry of Rare Earths. *Elsevier*, (1972).

[32]. H. Nakamura and T. Kimura, *Phys. Rev. B,* **80**, 121308 (2009).

[33]. N. Wadehra, R. Tomar, R. M. Varma, R. K. Gopal, Y. Singh, S. Dattagupta and S. Chakraverty, *Nat. Commun*., **11**, 874 (2020).

[34]. K. Zou, Sohrab Ismail-Beigi, Kim Kisslinger, Xuan Shen, Dong Su, F. J. Walker, and C. H. Ahn, APL Mater., 3, 036104 (2015).

[35]. H. Zhang, X. Yan, X. Zhang, Q. Zhang, J. Zhang, F. Han, L. Gu, B. Liu, Y. Chen, B. Shen and Y. Sun, *ACS Appl. Mater. Interfaces*, **9**, 36456 (2017).

[36]. P. Vousden, *Acta Crystallogr.*, **4**, 373 (1951).

[37]. S. H. Wemple, *Phys. Rev.*, **137**, A1575 (1965).

[38]. M. Setvin, M. Reticcioli, F. Poelzleitner, J. Hulva, M. Schmid, L. A. Boatner, C. Franchini and U. Diebold, *Science* **359**, 6375 (2018).

[39]. G. E. Jellison, I. Paulauskas, L. A. Boatner and D. J. Singh, *Phys. Rev. B,* **74**, 155130 (2006).

[40]. I. Golovina, B. Shanina, S. Kolesnik, I. Geifman and A. Andriiko, *Phys. Status Solidi Basic Res*., **249**, 2263 (2012).

[41]. I. S. Golovina, S. P. Kolesnik, V. P. Bryksa, V. V. Strelchuk, I. B. Yanchuk, I. N. Geifman, S. A. Khainakov, S. V. Svechnikov and A. N. Morozovska, *Phys. B Condens. Matter.*, **407**, 614 (2012).

[42]. E. A. Eliseev, A. N. Morozovska, M. D. Glinchuk and R. Blinc, *J. Appl. Phys*., **109**, 094105 (2011).

[43]. V. Skoromets, S. Glinšek, V. Bovtun, M. Kempa, J. Petzelt, S. Kamba, B. Malič, M. Kosec and P. Kužel, *Appl. Phys. Lett.*, **99**, 052908 (2011).

[44]. I. T. Bae, T. Ichinose, M. G. Han, Y. Zhu, S. Yasui and H. Naganuma, *Sci. Rep.*, **8**, 1 (2018).

[45]. X. Fan, W. Zheng, X. Chen and D. J. Singh, *PLoS One*, **9**, 3 (2014).

[46]. Y. Yang, C. S. Lin, J. F. Chen, L. Hu and W. D. Cheng, *J. Appl. Phys.*, **116**, 153709 (2014).

[47]. M. L. Scullin, J. Ravichandran, C. Yu, M. Huijben, J. Seidel, A. Majumdar and R. Ramesh, *Acta Materialia*, **58**, 457 (2010).

[48]. R. S. Klein and G. E. Kugel, *Phy. Rev. B*, **50**, 9721 (1994).

[49]. Z. Zhou, G. Huang, J. Shen, S. Gong, P. Zhou, L. Yin, R. Zhao, G. Liu, J. Zhang, Y. Li, C. Ma, and Y. Jiang, *Ceram. Int*., **47**, 7425 (2021).

[50]. S. Goyal, N. Wadehra and S. Chakraverty, *Adv. Mater. Interfaces*, **7**, 2000646 (2020).

[51]. R. Tomar, N. Wadehra, S. Kumar, A. Venkatesan, D. D. Sarma, D. Maryenko and S. Chakraverty, *J. Appl. Phys.*, **126**, 035303 (2019).

[52]. S. Goyal, R. Tomar and S. Chakraverty, *ACS Appl. Electron. Mater*., **3**, 905 (2021).

[53]. A.D. Caviglia, S.Gariglio, N. Reyren, D. Jaccard, T. Schneider, M. Gabay, S. Thiel, J. Mannhart, J.M. Triscone and G. Hammerl, *Nature*, **456**, 7222 (2008).

[54]. Y.Z. Chen, J. L. Zhao, J. R. Sun, N. Pryds and B.G. Shen, *Appl. Phys. Lett*., **97**, 123102 (2010).

[55]. Y. Xie, Y. Hikita, C. Bell and H. Y. Hwang, *Nat. Commun*., **2**, 494 (2011).

[56]. A. Tebano, E. Fabbri, D. Pergolesi, G. Balestrino and E. Traversa, *ACS Nano*, **6**, 2 (2012).

[57]. K. Au, D. F. Li, N. Y. Chan and J. Y. Dai, *Adv. Mater*., **24**, 19 (2012).

[58]. Y. Lei, Y. Li, Y. Z. Chen, Y. W. Xie, Y. S. Chen, S. H. Wang, J. Wang, B. G. Shen, N. Pryds, H.Y. Hwang and J. R. Sun, *Nat. Commun*., **5**, 5554 (2014).

[59]. S. Goyal, A. Singh, R. Tomar, R. Kaur, C. Bera and S. Chakraverty, *Solid State Commun.*, **316-317**, 113930 (2020).

[60]. K. X. Jin, B. C. Luo, Y. F. Li, C. L. Chen and T. Wu, *Journal of Applied Physics*, **114**, 033509 (2013).

[61]. N. Y. Chan, M. Zhao, N. Wang, K. Au, J. Wang, L. W. H. Chan and J. Dai, *ACS Nano*, **7**, 8673 (2013).

[62]. J-thing Yang, C. Ge, K. Jin, H. L and G. Yang, *Appl. Optics*, **55**, 9, (2016).

[63]. M. P. Warusawithana, C. Richter, J. A. Mundy, P. Roy, J. Ludwig, S. Paetel, T. Heeg, A. A. Pawlicki, L. F. Kourkoutis, M. Zheng, M. Lee, B. Mulcahy, W. Zander, Y. Zhu, J. Schubert, J. N. Eckstein, D. A. Muller, C. S. Hellberg, J. Mannhart and D. G. Schlom, *Nat. Commun*., **4**, 2351(2013).

[64]. D. V. Christensen, Y. Frenkel, P. Schütz, F. Trier, S. Wissberg, R. Claessen, B. Kalisky, A. Smith, Y. Z. Chen and N. Pryds, *Phys. Rev. Appl.*, **9**, 054004 (2018).

[65]. C. Xu, C. Bäumer, R. A. Heinen, S. Hoffmann-Eifert, F. Gunkel and R. Dittmann, *Sci. Rep.*, **6**, 22410 (2016).

[66]. D.V Christensen, F. Trier, W. Niu, Y. Gan, Y. Zhang, T. S. Jespersen, Y. Chen and N. Pryd, *Adv. Mater. Interfaces*, **6**, 21 (2019).

[67]. Z. Chen, Y. Liu, H. Zhang, Z. Liu, H. Tian, Y. Sun, M. Zhang, Y. Zhou, J. Sun and Y. Xie, *Science*, **372**, 6543 (2021).

[68]. Z. Yang, Y. Chen, H. Zhang, H. Huang, S. Wang, S. Wang, B. Shen and J. Sun, *Appl. Phys. Lett.*, **111**, 231602 (2017).

[69]. L. Cheng, L. Wei, H. Liang, Y. Yan, G. Cheng, M. Lv, T. Lin, T. Kang, G. Yu, J. Chu, Z. Zhang and C. Zeng, *Nano Lett.*, **17**, 6534 (2017).

[70]. H. Zhang, X. Yan, X. Zhang, S. Wang, C. Xiong, H. Zhang, S. Qi, J. Zhang, F. Han, N. Wu, B. G. Liu, Y. Chen, B. Shen and J. Sun, *ACS Nano*, **13**, 609 (2019).

Chapter 2

Experimental techniques for growth and characterization

2.1 Substrate preparation

The substrate commonly used in this thesis are (001) oriented single-crystalline STO and KTO. These substrates were bought from the MTI Corporation and typical dimensions are 10x10x1 mm^3 and 5x5x1 mm^3. Commercially available substrate crystals usually come with mechanically polished surfaces of low miscut angle, typically less than 0.1°. (High miscut substrates are also available separately.) Miscut angle is the angle between the normal to the substrate surface and to the crystallographic plane. Along the (001) direction, a perovskite ABO_3 crystal consists of an alternate stacking of AO and BO_2 layers, and the surface of as-received substrates is always composed of a mixed layer of AO and BO_2. Depending upon the oxidation state of metallic elements, the ideal topmost surface layer would be either polar or non-polar. This can be easily understood from **Fig. 2.1**, where STO atomic arrangement is shown in (001) orientation.

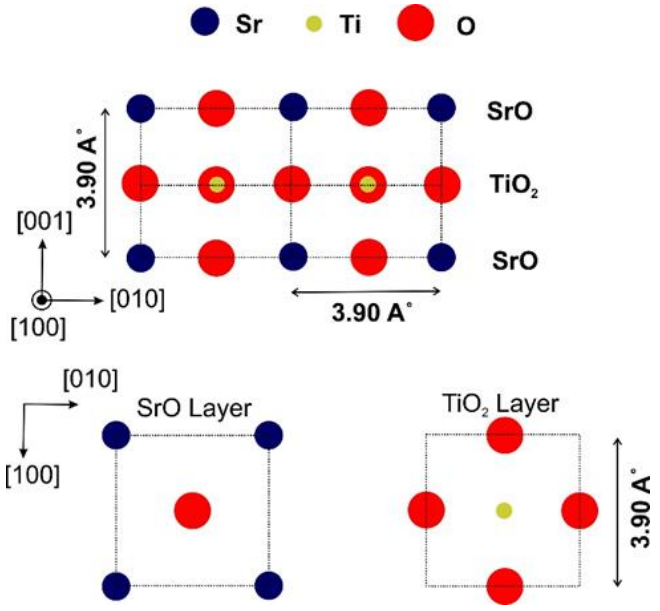

Figure 2.1: Alternating layer of STO in (001) direction having the total charge 0 at SrO and TiO_2 plane.

Here SrO is AO layer, where we have only one Oxygen atom and 4 Strontium atom at the corner of the square have a sharing of ¼ atom in a unit cell. So, we get one Sr and one O atom in total at this plane and due to two equal charges on both the atoms, we get a neutral charge layer. Similarly, in the TiO_2 layer or that is BO_2 plane, B cation can exhibit in B^{+4} state while two oxygen atoms will have a state O^{-4}. So, the total charge on the layer neutralizes to 0. Again, this can be understood from the TiO_2 layer plane from **Fig. 2.1**, where there is existence of only one Ti atom at the centre and each oxygen atom at the edge have a contribution of only half atom in a unit cell. So, we have only two atoms of the oxygen with total charge of O^{-4} and one Ti atom with charge Ti^{+4}. These charges again give a neutral layer of TiO_2. So, we have alternating neutral layer of SrO and TiO_2. Hence $SrTiO_3$ is a non-polar perovskite compound. Similar features of mixed termination with different chemical compositions are found for substrates with other (hkl) orientations.

These commercially available single-crystal substrates are usually in the form of mixed-surface termination so a proper treatment is required to make them single-terminated. To achieve a single termination step-like surface in STO, these substrates were annealed at 900 °C for 2 hours. The annealing leads to a step and terrace-like surface with some agglomerated SrO particles on the surface as confirmed by the AFM images [1]. These particles can be removed by further ultrasonication in DI water at 60 °C followed by another annealing at 1000 °C. AFM confirms the step and terrace-like surface of STO (TiO_2 terminated) with one unit cell height ~ 0.4 nm.

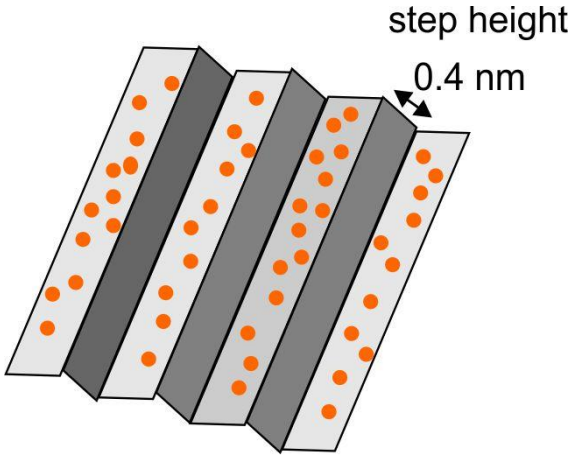

Figure 2.2: Schematic of the step and terrace-like surface of the STO crystal with step height nearly 0.4 nm (one unit cell).

Similarly, to achieve single termination in KTO, we annealed them at high temperature (600 °C) and further etching of KO layers with deionized water at 60 °C. When annealed at high temperature, there is always chances of potassium vacancies being created in KTO because potassium is a volatile material. So, two KTO substrates were annealed simultaneously with one on the top of other by maintaining a gap between them with the help of sapphires. By this process, we get the step and terrace-like surface of KTO [1].

The Hall effect is the production of a potential difference (Hall Voltage) across an electrical conductor that is transverse to an electric current in the conductor and to an applied magnetic field perpendicular to the current. It was discovered by Edwin Hall in 1879.

1. **Ordinary Hall Effect**: When a non-ferromagnetic metallic sample is exposed to a perpendicular external magnetic field B, the Lorentz force acting on the current carriers gives rise to a transverse voltage in the plane of the sample. The transverse component of the resistivity, ρ_{xy} depends on the magnetic field through the relationship $\rho_{xy} = R_O B$, where $R_O = 1/ne$ is known as the Hall coefficient. n is the carrier density, and e is the electron charge. This phenomenon whose entire explanation is classical is known as normal Hall effect.

2. **Anomalous Hall Effect**: In ferromagnetic materials, the transverse resistivity acquires an additional term independent of the magnetic field, which is often proportional to the magnetization M of the sample, and becomes constant once the sample has reached its saturation magnetization. This effect is referred to as Anomalous Hall Effect (AHE). The ordinary Hall effect of classical physics requires an external magnetic field, the anomalous Hall effect requires only a magnetization, and it was soon realized that ferromagnets display a spontaneous Hall conductivity in the absence of an external magnetic field. This effect has been observed in a multitude of system, including transition metals and their oxides, in materials that exhibit colossal magnetoresistance, ferromagnetic semiconductors, topological insulators, and a host of other topological materials.

3. **Topological Hall Effect:** This effect generally occurs in magnetic materials with topological properties, as a consequence of non-uniform and non collinier magnetization as well as special chirality. Its mechanism and properties are different from the conventional anomalous Hall effect induced by uniform magnetization. When the spins in magnets do not align in one direction, but smoothly vary in position space, the case is different from the ordinary and anomalous Hall effects. The varying spin textures give rise to a new Hall signal that is known as the topological Hall effect (THE). The existence THE only needs topologically protected spin texture, not the spin-orbit effect.

   Electrons injected in to conductive magnetic single layer or heterostructure with spatially varying spin textures, no collinier spin and spin chirality due to either bulk or interfacial Dzyaloshinskii-Moriya interaction (DMI) as well as frustrated effect, pick up an additional Hall signal apperaring as bumps or dips in Hall resistance curves. Because of the strong exchange coupling between spins of conduction electrons and local magnetic moments, the electron spin are enforced adiabatically to follow the spin texture. In consequence, the conduction electrons accumulate a Berry phase that is sensitive to the topology of the spin texture.In analogy to the ordinary Hall effect and Aharonov Bohm effect(AB) effect associating with real magnetic field, it is useful to introduce a fictitious magnetic field (b^z) for a phenomenological explanation of the THE. The field could be estimated from the berry curvature in the real space (position space). AHE describes the contribution of the magnetization and THE describes the topological contribution to Hall signals. AHE arises from the momentum space fictitious magnetic field, while THE signal originates in real space fictitious magnetic field that is related to the topology of spin textures and can be expressed by topological number /charge:

   $P_{THE} = Pb^z /en$, where P stands for the spin polarization of the carriers, e for the electron charge and n for the carrier density.

   The total Hall signal including OHE, AHE and THE contributions is expressed as:

   $$\rho_H = R_O B + R_S M + PR_O b^z$$

2.2 Epitaxial oxide film deposition by PLD

For most of the devices based on the epitaxial perovskite-type thin films and heterostructures, high and defect free crystallinity, atomically flat surface and atomically well-defined interfaces are usually the prerequisite for good device performance. Therefore, deposition of high-quality film and understanding its growth mechanism is very important. The epitaxial thin film fabrication of complex oxide materials are mostly done by physical vapor deposition techniques such as sputter deposition, pulsed laser deposition and Molecular beam epitaxy. Among them, pulsed laser deposition technique is one of the most largely used one, because of its unique features such as control over rate of deposition, ablated species stoichiometry and kinetic energy of the deposited particles. In this thesis, we will focus on the epitaxial thin film and related interfaces grown by PLD technique. During the growth of thin film, RHEED (write the full form first) technique equipped with our PLD system is used to study the mechanism and film surface processes. Growth rate control on an atomic level as well as *in-situ* growth studies at the typical oxygen pressure during deposition is possible with the help of high pressure RHEED.[2] The detail working principle of RHHED is explained below.

2.2.1 Principle and advantages of thin film growth by PLD

In the PLD technique, a pulsed high-energy laser beam is used to melt, evaporate and ionize material from the surface of a target resulting in the ablation of material. The removal of atoms from the bulk material is done by vaporization of the bulk at the surface region in a state of non-equilibrium. In this, the incident laser pulse penetrates into the surface of the material within the penetration depth. This dimension is dependent on the laser wavelength and the index of refraction of the target material at the applied laser wavelength and is typically in the region of 10 nm for most materials. The strong electrical field generated by the laser light is sufficiently strong to remove the electrons from the bulk material of the penetrated volume. This process occurs within 10 picoseconds of a nanosecond laser pulse and is caused by non-linear processes such as multiphoton ionization which are enhanced by microscopic cracks at the surface, voids, and nodules, which increase the electric field. The free electrons

oscillate within the electromagnetic field of the laser light and can collide with the atoms of the bulk material thus transferring some of their energy to the lattice of the target material within the surface region. The surface of the target is then heated up and the material is vaporized. So, a dense layer of vapor is formed and energy absorption during this time causes both the pressure and temperature of the vapor to increase resulting in the partial ionization. Thus, due to high pressure, this layer expands from the target and forms the so called 'plasma plume' and further expands rapidly away from the target surface towards the substrate to form thin layer of the material [3]. During this expansion, the internal thermal and ionization energies are converted into the kinetic energy of the ablated the particles. Attenuation of this energy take place as the particle expands towards substrate due to the thermalization occurs at large ambient gas pressure (mass and pressure determine the interaction with the particles).

This wide range in kinetic energy (low at high ambient pressure and high in vacuum) is one of the unique features of PLD and can be used to modify the thin film growth. Another interesting feature of the PLD is deposition rate that can be as high as 10^2 - 10^5 nm/sec [4,5]. This is orders of magnitude higher compared to other PVD techniques, which is typically in the range of 10^{-2} -10^{-1} nm/sec. There are various parameters that control the deposition rate such as laser energy density at the target, pulse energy, ambient gas properties and distance between target and substrate.

The crystal quality and stoichiometry of the thin film depends mainly on the absorption, diffusivity [6,7] and energy of the particle on the surface. Depending on the deposition parameters, the kinetic energy of the ablated particles can be controlled and there by the surface diffusivity and absorption or desorption probability [8] of the adatoms arriving at the substrate or film surface can be controlled. It is possible to use inert and reactive background gases like O_2, O_3, Ar, N_2 etc. in the main deposition chamber of PLD.

2.2.2: Experimental set-up

For thin film growth, we used a combinatorial pulsed laser deposition system, Mobile-Combi-Laser MBE by Pascal, consists of a load lock chamber and main deposition

chamber. Load lock chamber is used to transfer the substrate and target to main chamber from atmosphere, before deposition. They are transferred into the main chamber with the help of a rod without breaking the vacuum of the main chambers. Thin film deposition is done in the main chamber kept at ultra-high vacuum base pressure of $\sim$ $1x10^{-9}$ Torr. The substrate is heated by an infrared laser (IR) of wavelength 809.5 nm via a SiC plate.

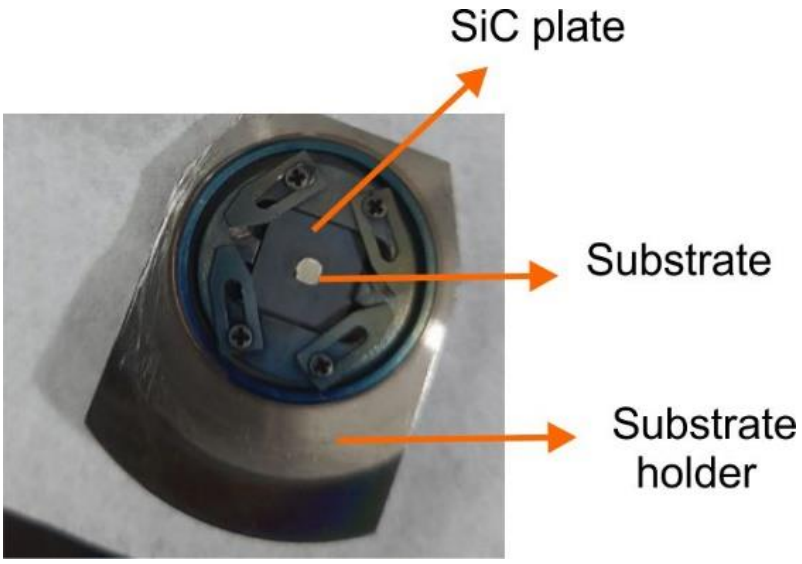

Figure 2.3: Real picture of the sample pasted on SiC plate on the substrate holder.

The substrate is heated using an infrared laser. The shape and size of this heating laser profile on the backside of the substrate holder plate can be changed through a combination of lens assembly. By adjusting the lens position the laser beam can either be focused or defocused to create temperature gradient or uniform temperature. We will discuss in detail about the combinatorial temperature gradient technique in the next chapter of this thesis. The substrate can be heated using a focussed lens for developing a temperature gradient across the length of the substrate or by using a lens of higher focal length for uniform heating of the substrate. The temperature of the substrate is estimated with the help of a pyrometer from the opposite side of the heating laser. It is placed outside the chamber and measure the temperature through a quartz viewport. The function and working of these pyrometers will be discussed in detail in the next chapter where we have done the optimization of the PLD system. Turbo-molecular pump (TMP) and rotary pumps are used to evacuate these both chambers.

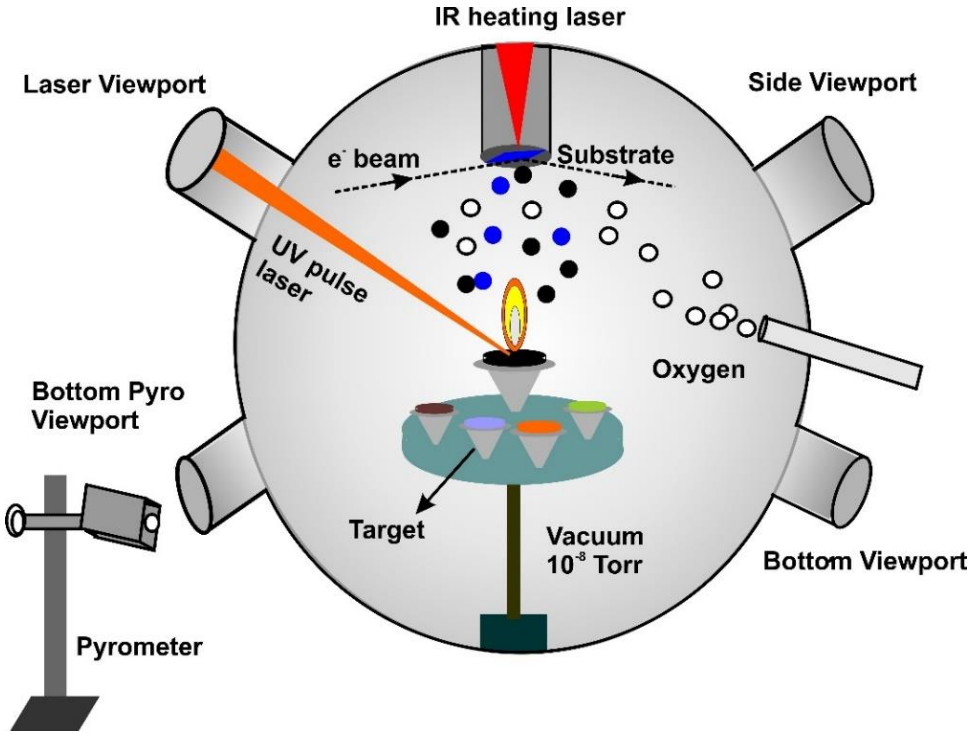

Figure 2.4: Schematic of inside view of the main deposition chamber of our PLD system.

The main chamber is equipped with six target holders and two masks that are operated by motor, are used for combinatorial thin film growths. For ablating the target materials, a 248 nm KrF excimer laser (Complex Coherent) with a pulse duration of 20 ns is used, which is guided by a combination of optics to fall on the target. The spot area of the laser beam on target can be controlled by focussing the motor operated lens. Thin film growth and thickness can be controlled with the RHEED system discussed in the next section.

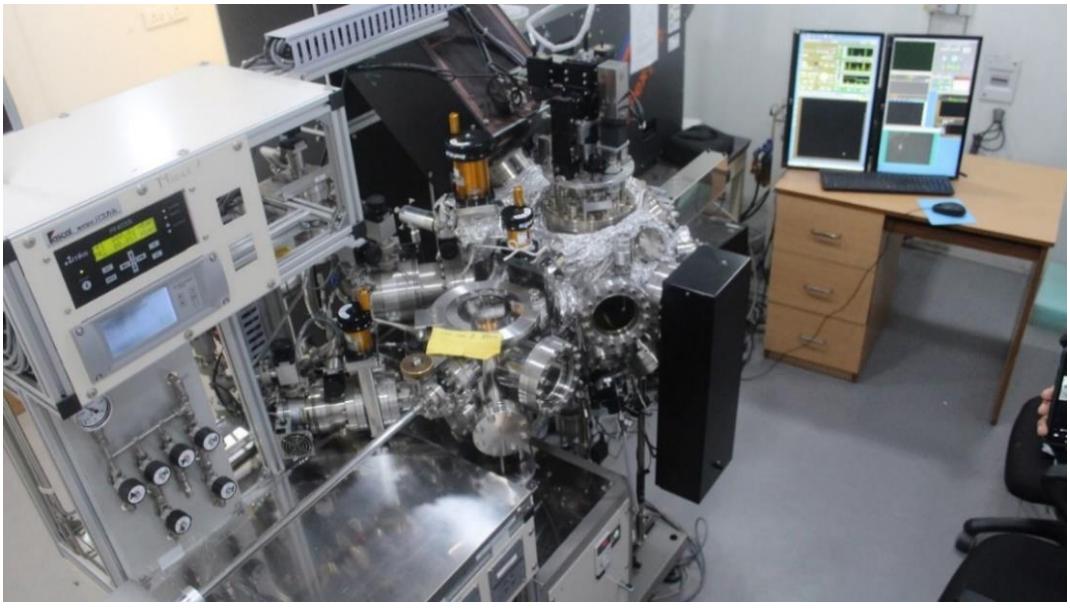

Figure 2.5: Picture of our PLD system, Mobile-Combi-Laser MBE at INST Mohali.

2.3: Structural Characterization methods

To have clear understanding of the thin film growth and achieve optimized growth condition, thorough analysis of the crystal structure and surface morphology is necessary. With the help of RHEED technique, the morphology of the surface can be monitored during and after the growth of thin film. Also, quality of the surface can be analyzed with the atomic force microscopy (AFM) technique.

2.3.1: Reflection high energy electron diffraction (RHEED)

RHEED is a powerful technique used as an *in-situ* probe to monitor the growth of thin films both in research and industry. Being compatible with the ultra-high vacuum deposition condition, It unable the direct exploration of the growth dynamics and surface morphology [9]. It is a widely used and preferred technique for fabrication of thin films. Here diffracted electrons by the surface atoms gives idea about the periodic arrangement of the surface atoms.

In the set-up of RHEED, an accelerated mono-energetic electron beam (10-50 keV) incidents on the sample surface with a glancing angle (< 3°) and is reflected. Here due to the low glancing angle, a few atomic layers are probed only, that is the reason for the high surface sensitivity of RHEED [10]. The diffracted electrons are collected on a phosphor screen (detector) and forms a diffraction pattern as shown in the schematic **Fig. 2.6.**

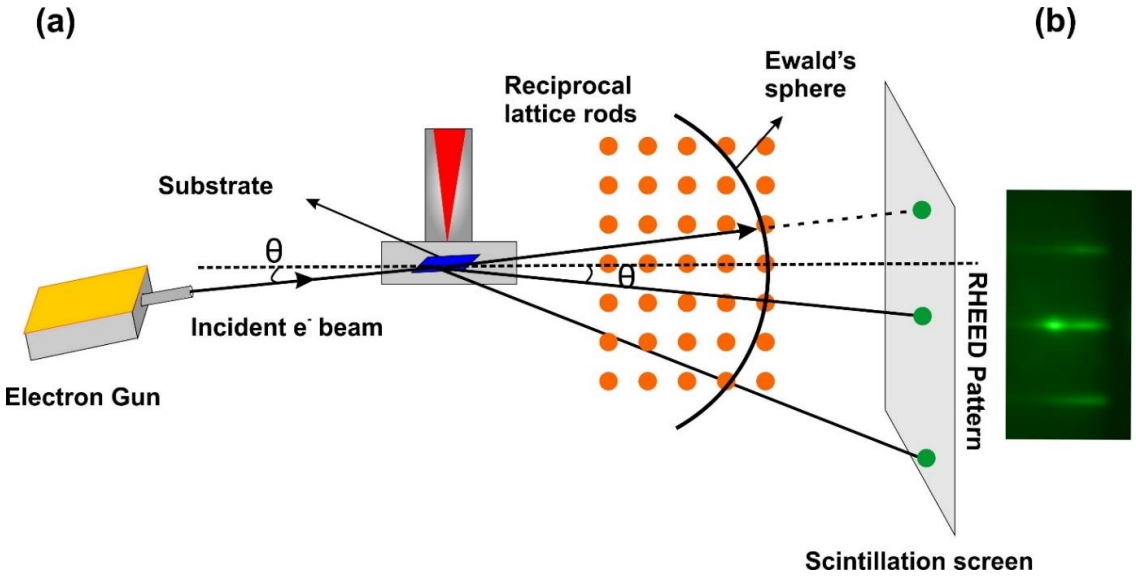

Figure 2.6: (a) Schematic of RHEED measurement geometry and construction of Ewald's sphere. (b) RHEED pattern of the surface after deposition.

This pattern is used to explain the surface structure of the film or sample. If the surface is atomically flat, then sharp RHEED spots are seen and if surface is rough, then RHEED pattern is more diffused. The growth rate of thin film is determined by the oscillations in the RHEED intensity during the growth. One oscillation in the intensity confirms the formation of one monolayer or one unit cell (~0.4 nm). The periodicity in the oscillations confirms the layer-by -layer growth of the film. **Figure 2.7** shows that how a monolayer formation take place during the growth process of film.

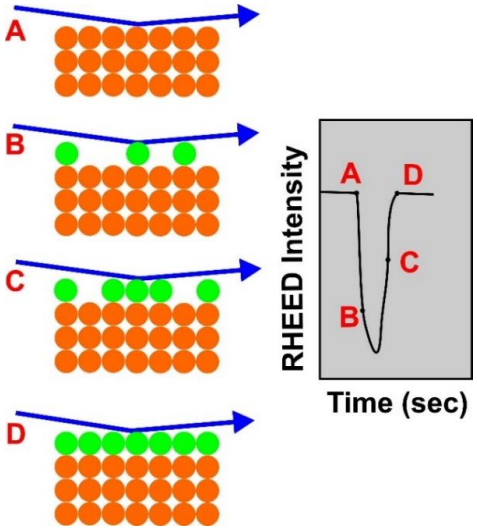

Figure 2.7: Schematic of the atomic layer formation confirmed by RHEED intensity oscillation.

When the electron beam is diffracted from the crystalline surface of the substrate, the intensity is maximum (at A) as shown in **Fig. 2.7.** As the ablated material starts to deposit then intensity starts to decrease due to the scattering by deposited material (at B). But as the complete layer starts to forming, the intensity again starts to rise due to the less scattering by atoms (at C). One complete layer is formed when intensity reaches to initial state at point D. This continues with time and we get the periodic oscillations with the increase in the thickness of the film. In the RHEED set-up, the phosphor screen and electron source are located far from sample to avoid interference with the deposition process. In our study, we have used RHEED to monitor number of monolayers of LVO and STO on STO, EuO over KTO substrate under the optimized conditions. Actual samples are not always ideal like atomically flat surface or polycrystalline surface. RHEED pattern always suffer modification due to various imperfections of the samples. In the below **Fig. 2.8**, we have discussed some cases with different surface morphology with their corresponding RHEED pattern.

(a) Flat and single-crystalline surface

When the sample has an atomically flat surface and a perfect single-crystalline structure as shown in **Fig. 2.8 (a),** its reciprocal rods are very sharp without intensity modification along the rods under an assumption that the RHEED detects the topmost atomic layer only. Then the diffraction pattern is a reflection type in which all diffraction spots are on the Laue zones and have the same intensity. In reality, however, the electron beam penetrates into several atomic layers below the surface. Then the intensity is modulated along the reciprocal rods, resulting in that some diffraction spots are stronger and others are weaker. This is due to interference among waves scattered from different atomic layers.

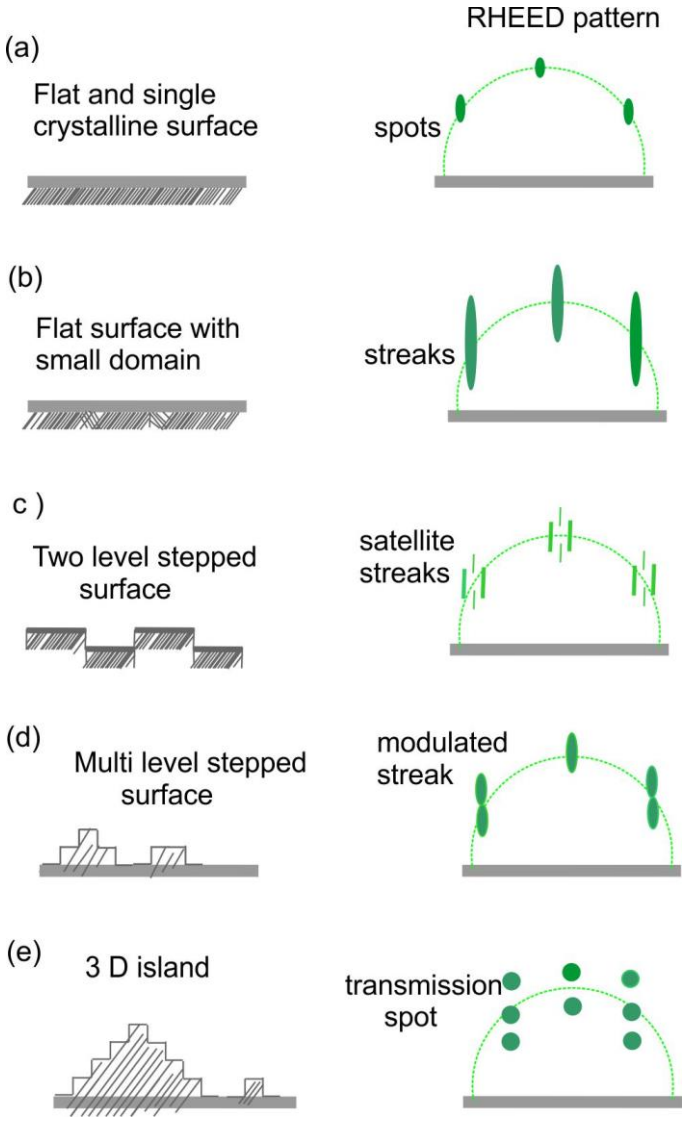

Figure 2.8: Schematics of various kinds of realistic surfaces real-space morphology, and their RHEED patterns.

(b) Flat surface with small domain

As shown in Figure 2.8(b), when the surface is composed of small out-of-phase domains whose size is smaller than the coherence length of electron beam, the reciprocal rods are broader due to effect of the Laue function for finite sample sizes. The width of the reciprocal rods is inversely proportional to the average size of the domains. Then, the intersections between the Ewald sphere and the reciprocal rods become larger ellipses, resulting in elongated and broader diffraction spots (streaks) in the RHEED pattern. Inversely, from the width and length of the streaky spots, we can estimate the average size of domains.

(c) Two-level stepped surface

As shown in **Fig. 2.8 (c),** when the surface is rough by two-level terraces with one-atomic height difference, the reciprocal rods become a bit complicated. Under the on-Bragg condition where the electron waves reflected from the lower and upper terraces interfere with each other constructively, the electron beam does not "see" the two-level roughness, so the reciprocal rods are sharp as those of the atomically flat surfaces. On the other hand, under off-Bragg conditions where the waves reflected from the lower and upper terraces interfere destructively, the intensity of the diffracted beam is weak. The intensity is proportional to the difference in area fraction between the lower and upper terraces. And the reciprocal rods are split into two, of which lateral spacing is proportional to the average width of terraces: the terraces act as a grating for the electron wave. As a result, the diffraction spots are also split into satellite spots/ streaks. From the spacing of the satellite streaks, we can estimate the average terrace width.

(d) Multilevel stepped surface

As shown in **Fig. 2.8(d),** when the surface is rough with multilevel terraces of different widths, the reciprocal rods are modulated because they are regarded as superpositions of those in **Fig. 2.8(c)** with various spacing of split rods at the off-Brag conditions. Then, the reciprocal rods have sharp "nodes" with strong intensity at the on-Bragg points, while they become broader and weaker at the off-Bragg portions. This produces RHEED patterns having elongated streaks with intensity modulation in the perpendicular direction.

(e) 3D island surface

If the surface is sufficiently rough, a so-called transmission pattern will be obtained. Electrons passing through the asperities(roughness) will see the additional periodicity of the atomic planes below the surface. As a result, the reciprocal lattice will be an array of points instead of rods. The regular array of spots of a transmission pattern is shown in **Fig.2.8(e).**

2.3.2: Atomic Force Microscopy (AFM)

Surface morphology study of the oxide films was done by using Bruker Multimode-8 AFM which is capable of doing both contact mode and tapping mode surface scans. For the normal height profile scans, SiN tips of force constant value around 40 N/m were used. Surface quality was analyzed by the roughness value of the film surface.

The Atomic Force Microscope is a kind of scanning probe microscope in which a topographical image of the sample surface can be achieved based on the interactions between a tip and a sample surface.

A typical AFM consists of a cantilever with a small tip (probe) at the free end, a laser, a 4-quadrant photodiode and a scanner (Piezo transducer) as shown in the schematic **Fig. 2.9**.

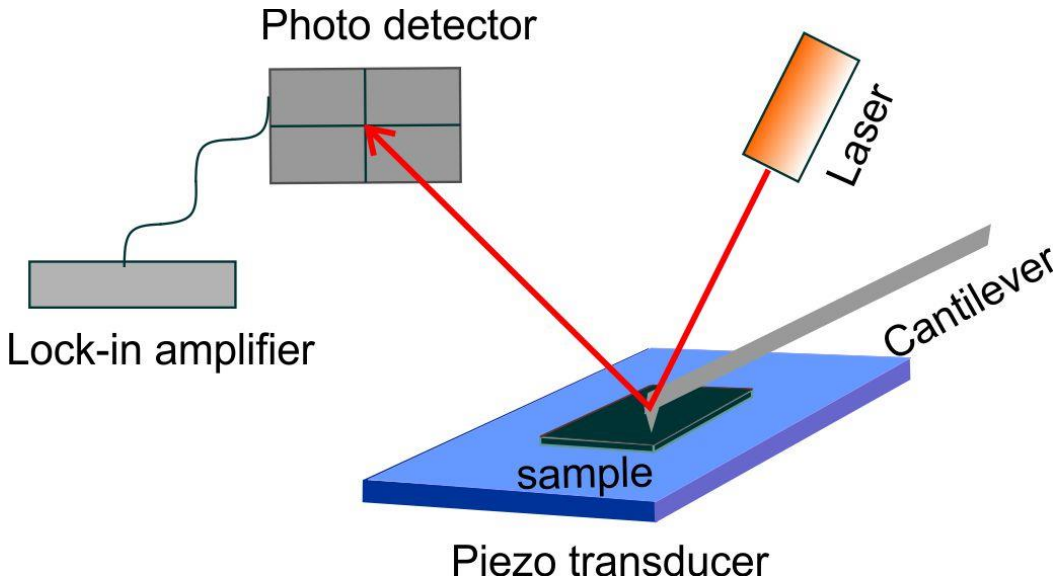

Figure 2.9: AFM set up with different assembly for the surface morphology of the sample.

Surface characteristics can be explored with very accurate resolution in a range of 100 μm to less than 1 μm. In AFM, a tip is used for imaging. It is generally made of silicon or silicon nitride (Si_3N_4). It approaches the sample in a range of interatomic distances (around 10 Å). The tip is commonly 3-15 microns in length. It is attached to the end of the spring cantilever. The cantilever is around 100-500 microns in length.

When the tip, which is attached to the free end of the cantilever, come very close to the surface attractive and repulsive forces due to the interactions between the tip and the sample surface cause a negative or positive bending of the cantilever. This bending is detected by the help of a laser beam. The cantilever can be thought of as a spring. The quantity of the generated force between the tip and the surface depends on the spring constant (stiffness) of the cantilever and the distance between the tip and the surface. This force can be characterized with Hooke's Law.

$$F=-k\cdot x$$

Where F = Force, k = spring constant, x = cantilever deflection. If the spring constant of the cantilever is less than surface, a bending occurs in the cantilever and this deflection is monitored. As the tip travels across the sample, it moves up and down according to the surface properties of the sample. These fluctuations are sourced by the interactions (electrostatic, magnetic, capillary, Van der Waals) between the tip and the sample. The displacement of the tip is measured and a topographical image is obtained.

AFM has different operation mode such as contact mode, tapping mode and non-contact mode. In our work, we have used the tapping mode operation for the roughness measurement of the sample surface.

2.4: Electrical and magnetic measurements

The transport measurements of the conducting two-dimensional interface were done using a physical properties measurement system (PPMS, Quantum Design Dynacool).

Figure 2.10: Picture of the PPMS facility at INST Mohali lab.

This system is capable of temperature scans from 350 K down to 1.8 K. To find the carrier density and mobility from the hall measurement, magnetic field scans from -14 T to 14 T was done.

The electrical contacts on the sample were made with the help of an ultrasonic wire bonder using Al wire. The schematic shows the resistivity and Hall bar geometry for the I-V measurement.

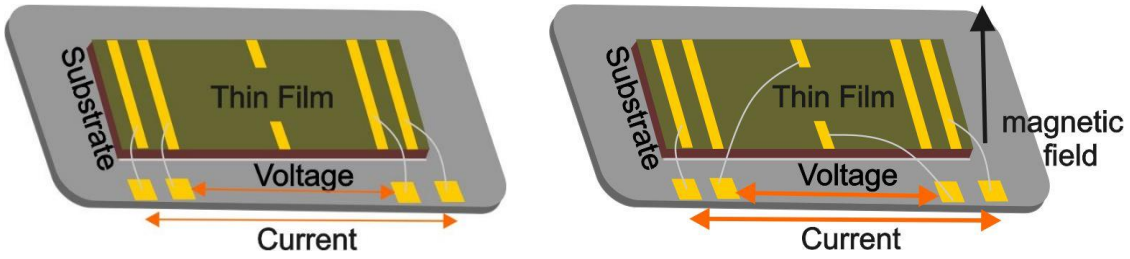

Figure 2.11: Schematic shows the resistivity and Hall bar geometry.

The linear behavior of the I-V curve before the measurement showed the contact to be ohmic. For the resistivity measurement in the PPMS, we use the AC transport measurement (ACT) type. In ACT four terminal measurement, two leads pass a current through the sample, two separate leads are used to the potential drop across the sample, and Ohm's law is used to calculate the sample resistivity. The voltage leads draw ideally

no current, so the current through the sample and potential drop across the sample can be known to a high degree of accuracy, virtually eliminates the effect of lead and contact resistance.

Here, ACT option can supply an AC bias current from 1Hz to 1kHz and can therefore provide greater measurement sensitivity than DC instruments because signal filtering can be employed. In this mode, current can be supplied in the range of 0.02 μA to 2 A depending upon the resistance of the sample.

2.5 Photoconductivity and Photo-Hall measurement

For the photo-gating study, three DPSS lasers having wavelength 405, 532 and 635 nm with variable power were used. The standard four probe method was employed for electrical measurement by using Keithley 2450 and 2635B source meter.

To see the photo-effect on samples at low temperature, a Cryogenic Four Probe Station (Janis Research) **Fig. 2.12** was used. Here the sample chamber was cool down using liquid nitrogen gas. The temperature can be controlled by an incorporated temperature controller that can be varied from 76 K to 1100 K.

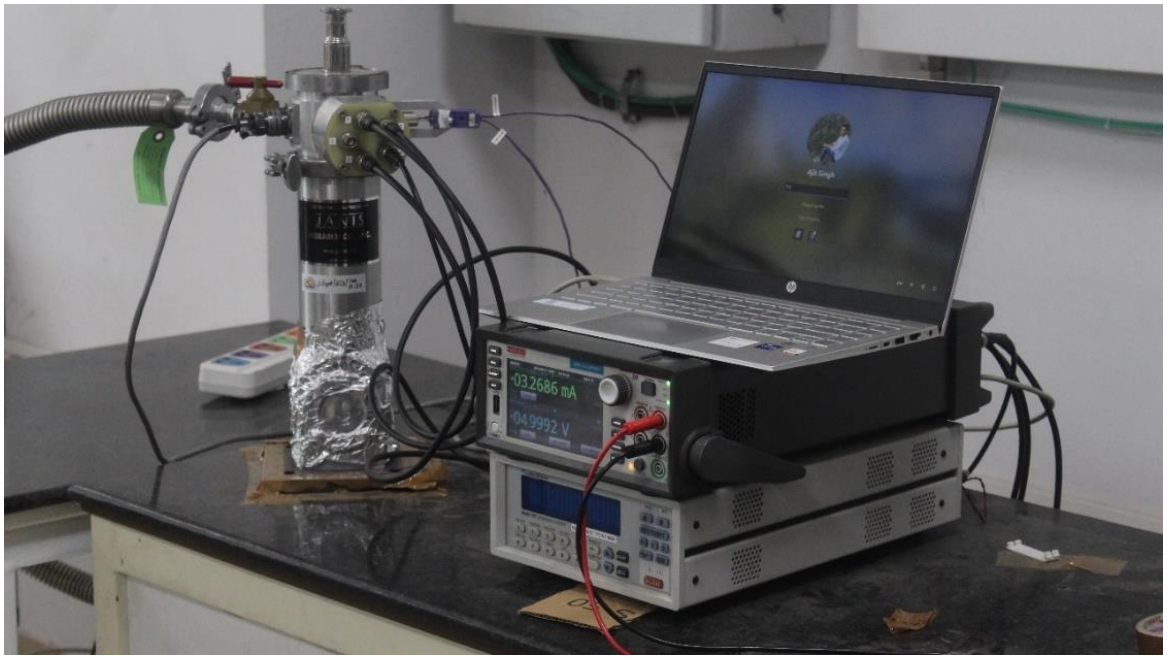

Figure 2.12: Picture of the Cryogenic four probe station in our lab at INST, Mohali

Bibliography:

[1]. R. Tomar, N. Wadehra, V. Budhiraja, B. Prakash and S. Chakraverty, *Appl. Surf. Sci.,* **427**, 861 (2017).

[2]. A.J.H.M.Rijnders, G.Koster, D.H.A.Blank and H.Rogalla, *Appl.Phys. Lett*. **70**, 1888 (1997).

[3]. R. Eason, *John Willey and sons, inc., Hoboken, New Jearsy* (2007).

[4]. D.B. Geohegan and A.A. Puretzky, *Appl. Phys. Lett*. **67**, 197 (1995).

[5]. M.Y. Chern, A. Gupta and B.W. Hussey, *Appl. Phys. Lett.* **60**, 3045 (1992).

[6]. B. Dam and B. Stäuble-Pümpin, *J. Mat. Sci.: Mat. in Elec*. **9**, 217 (1998).

[7]. Dave H.A. Blank, Guus J.H.M. Rijnders, Gertjan Koster and Horst Rogalla, *Appl. Surf. Sci.* **138-139**, 17 (1999).

[8]. M. Tyunina, J. Levoska and S. Leppävuori, *J. Appl. Phys*. **83**, 5489 (1998).

[9]. L. Daweritz, *Superlattices and Microstructures*, **9**, 141 (1991).

[10]. W. Braun, *Springer Verlag, Berlin*, (1999).

Chapter 3

A case study to address: “Is your pulsed laser deposition chamber clean?”

3.1 Introduction:

Thin-film growth methods allow one to make new materials by creating artificial superstructures. The surfaces of single-crystal substrates provide atomic templates that can be used to constrain atomic positions and thereby stabilize epitaxial films in crystal structures that are metastable. In this way, thin films can be locked into structures that cannot be achieved by bulk processing methods near thermodynamic equilibrium. Pulsed laser deposition (PLD) is one such deposition technique that is particularly attractive for the formation of artificially layered oxides because the material can be transferred stoichiometrically in the presence of reactive background gases such as oxygen.

Pulsed laser deposition (PLD) is a widely used and important technique for oxide thin film growth. Thin-film growth in a PLD system is drastically influenced by various parameters such as substrate-target distance, ablation flux, substrate temperature, background gas pressure, laser fluence, repetition rate and pulse duration, etc. The substrate temperature affects the kinetic of the ablated particles and ad-atoms [1]. The PLD outstands the other physical vapor deposition techniques as here the ablated particles reach the substrate surface with very high kinetic energy and we can also maneuver the growth of thin films by controlling the energy and deposition rate during each laser pulse as the diffusion constant is dependent on the ablated particles [2].

PLD has several characteristics that distinguish it from other film growth methods and provide special advantages for the growth of oxides and other chemically complex materials. Congruent transfer of the material is possible using PLD. Here, films have the same composition as the target when the focused laser energy density is chosen properly. It sets PLD apart from incongruent transfer methods such as thermal evaporation or

sputtering. Here, ambient gases can be used because no electron beams or hot filaments are needed in the chamber. Energetic species in the plasma plume react readily with gas molecules to form simple compounds (oxides, nitrides and hydrides). Growth of multilayered epitaxial heterostructure is also possible with PLD system. In these thin film structures, adjacent layers have different compositions, but all layers share a common, continuous crystal structure.

A fundamental difference of PLD with a rather expensive and sophisticated deposition technique, molecular beam epitaxy (MBE) is that, in case of MBE the film stoichiometry can be tuned by properly adjusting the molecular flux. In contrast, in the case of PLD, a single target of the compound is used, upon the shining of a pulsed laser, the target components do not evaporate congruently, the volatile component comes out first from the target. This not only affects the film stoichiometry but also creates a non-stoichiometry at the target surface. It has been reported that the laser fluence can be tuned to successfully control the (non) stoichiometry of the film [3-9]. All parameters in PLD such as laser fluence, substrate temperature, oxygen partial pressure, substrate-target distance and pulsed laser repetition rate play an important role in stoichiometry, crystalline quality and substrate morphology of the grown films [10-17].

PLD is widely used in combinatorial material science, as it enables rapid fabrication of different composite materials. Nevertheless, this method was usually limited to small substrates, since PLD deposition on large substrates area results in severe lateral inhomogeneity. A few technical solutions for this problem have been suggested, including the use of the different design of masks, which were meant to prevent inhomogeneity in the thickness and density of a layer, while only the composition is allowed to change. With this, one may grow different materials that too with the varying thickness on a single substrate with a single growth process. Combinatorial pulsed laser deposition (C-PLD) rapidly emerged, the basic idea being to grow on a single substrate, in a single deposition run, a film with continuous in-plane chemical modulation with different growth temperatures if and when desired. In this way, a wide range of chemical compositions are produced within the same sample and can be quickly scanned to identify compounds with optimum target properties. The concept of combinatorial research, initially introduced in the pharmaceutical industry, aims at synthesizing a large number of

compounds with complex and systematically varied compositions in a single batch. C-PLD has been used before to vary chemical compositions across C-MOS transistors [18]. Two types of combinatorial growth can be done with our Mobile Combi-Laser MBE as shown in **Fig. 3.1(a) and (b)**.

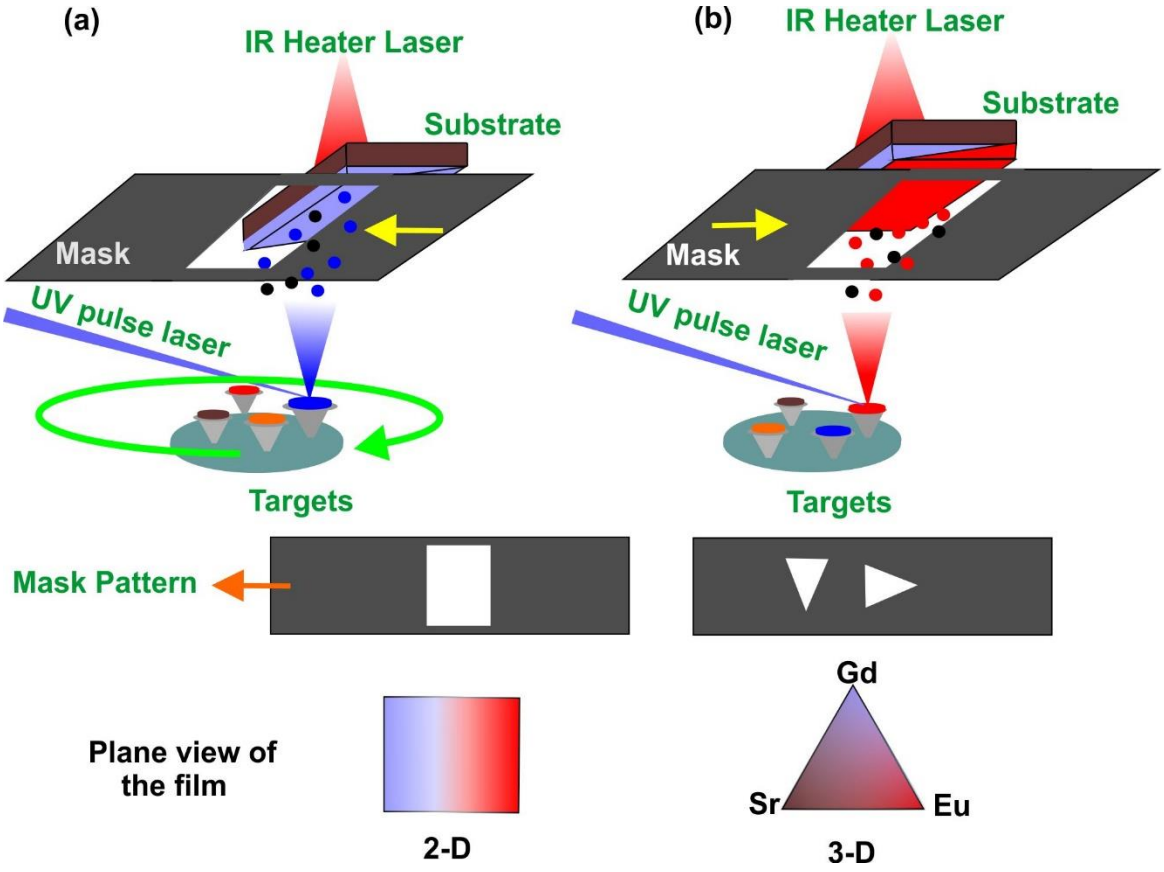

Figure 3.1: (a) and (b) shows that by moving the position of the mask and rotating the targets, we can grow superlattices of different materials with varying thicknesses.

By precise movement of the mask board patterned with rectangles or triangles at a close position of the substrate during thin film deposition, composition gradient thin film patterns can be formed on one piece of substrate. **Figure 3.1 (a) and (b)** shows that using a mask, we can grow superlattices with varying thicknesses on a single substrate. Here, we have shown that using a rectangular mask pattern a superlattice can be achieved with desired thickness. Similarly using triangular mask, composition gradient thin film can be grown as shown in **Fig. 3.1.** The 2D and 3D view is shown at the bottom part of the schematic **Fig. 3.1.**

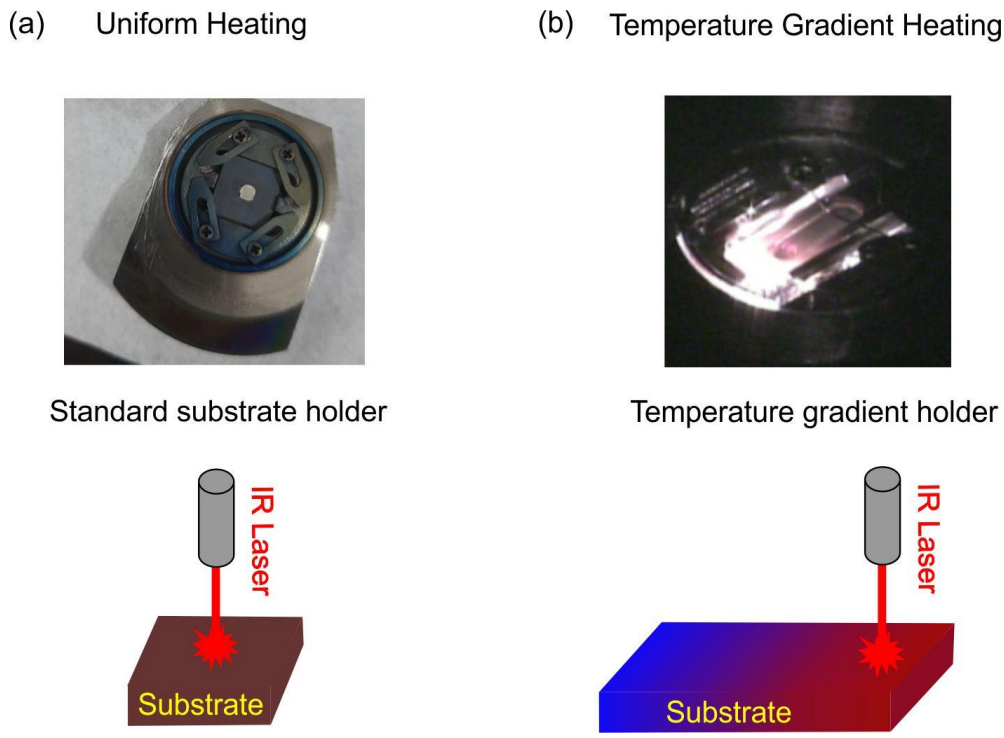

Figure 3.2: (a) Standard substrate holder for uniform heating of the sample. (b) Temperature gradient sample holder for combinatorial growth.

A combinatorial temperature deposition can also be done using PLD system. **Figure 3.2 (a) and (b)** is showing the real substrate holder picture for uniform heating and temperature gradient heating method. A temperature gradient can also be constructed on a single substrate to achieve different growth temperatures during a single growth process. We will study in detail in the next section of this chapter about temperature gradient growth technique. A combinatorial method is a powerful tool not only for the optimization of the growth temperature but also for a systematic investigation of the growth dynamics, composition effect and interface analysis [19].

With the successive range of depositions, reproducibility is the prime concern due to the contamination on the viewports, ablation laser energy on the target and the substrate temperature possessing an influential impact. Here, we have explored the aging effect of a C-PLD on the growth of various samples. In this chapter, we demonstrate how the growth conditions inside the chamber during the growth can be judged from the outside by combining *in-situ* and *ex-situ* techniques. This study gives a prior indication of the deposition chamber condition. By deploying a combined process of resistivity

measurement and homo-epitaxial growth of $SrTiO_3$ (STO) on a temperature gradient STO substrate, we have standardized the actual temperature of the substrate. A correlation between actual laser energy on the target surface and RHEED is set up to see the effect of multiple growth events of the pulsed laser viewport and hence, on the film properties. We have given an example of the growth of the $LaVO_3$ (LVO) -$SrTiO_3$ interface to elucidate the effect of repetitive growth on the chamber condition and hence on the reproducibility of the physical properties of the samples. Our experiments suggest a noticeable change in transport properties with successive deposition processes.

3.2 Experimental details:

In chapter 2, we had already discussed in brief the various component of the PLD system that plays an important role in the growth of the thin film. Here, in this section, details of the deposition chamber will be discussed. In the present C-PLD system, the substrate is heated with an infrared laser (IR) from the top of the deposition chamber. The temperature of the substrate is estimated by using a pyrometer at the bottom left side as shown in schematic **Fig. 3.3.**

In this schematic, we have shown the main chamber of a PLD deposition chamber consisting of all the components: Excimer laser viewport (V1), Infrared (IR) laser substrate heating unit, multiple target manipulator, RHEED gun-camera and pyrometer for substrate temperature detection. The main chamber (having a diameter of Φ = 260 mm) capacitates to deposit thin films in a wide pressure range by an ultra-high vacuum (UHV) pumping unit and process gas feeder (about 90 mm from the substrate) launch the process gas-like oxygen and argon to the main chamber. We have a krypton fluoride (KrF) ablation laser with a wavelength of 248 nm. This laser is guided through various lenses and mirror combinations to fall on the target via viewport V1 as depicted in **Fig. 3.3**. It is worth mentioning that the distance between the laser viewport and the target is 275 mm, the distance between the pyrometer viewport and substrate is 217.5 mm, and the distance between the heating laser viewport and the substrate is 202.9 mm.

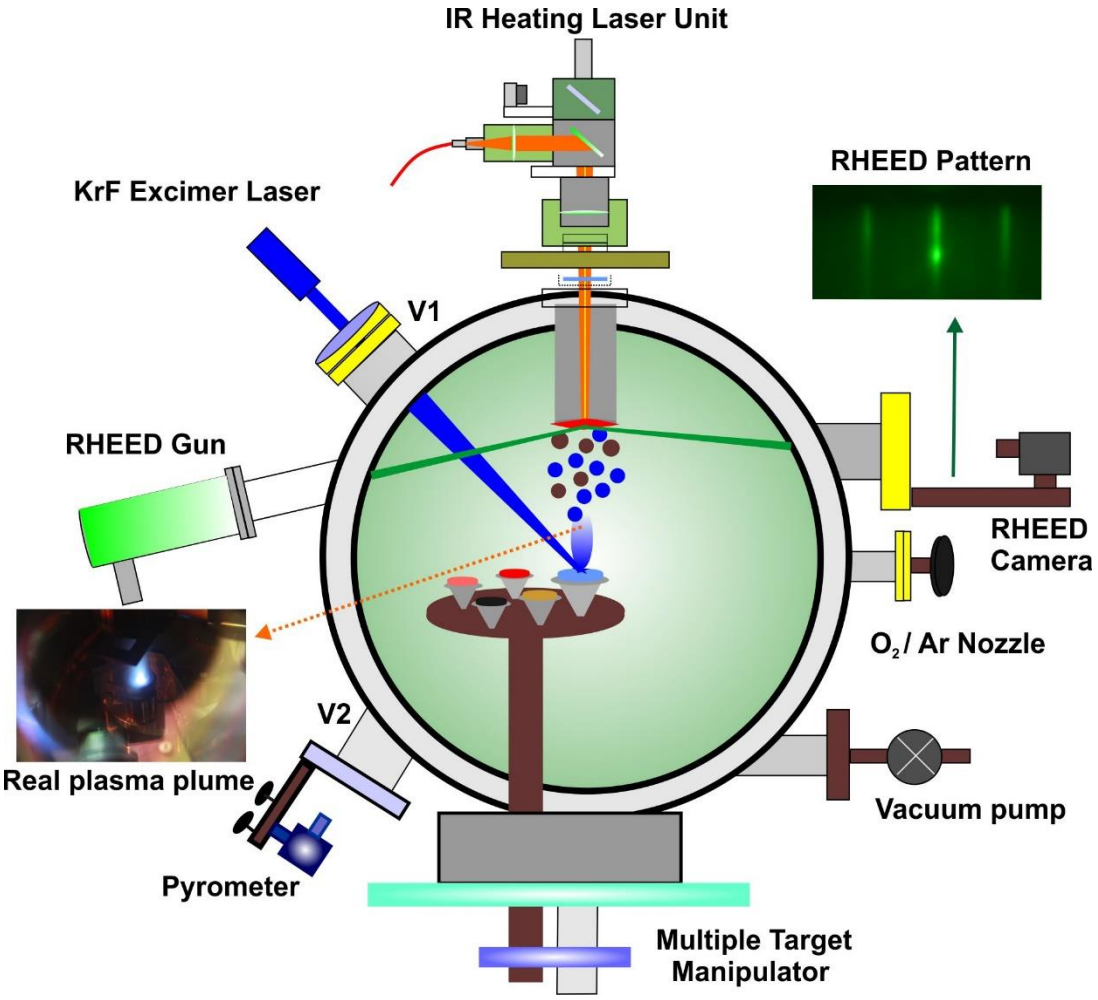

Figure 3.3: Schematic of the Pulsed laser deposition system consisting of different components. Real plasma plume and RHEED pattern is shown for STO-STO growth. Multiple target manipulator is attached at the bottom side to select the desired target material. Viewport V1 and V2 are for laser ablation on target and to sense the temperature of the substrate respectively. A diffracted electron beam is detected by the RHEED camera to give the RHEED pattern. The nozzle is shown to pass the desired gas in the chamber. IR heating laser unit is shown at the top side of the chamber.

The real picture of the plume formed when the high-energy laser beam is made to fall on the target is shown by a dotted arrow at the bottom side of this schematic. The substrate heater unit is installed on the top side of the PLD chamber. An IR laser beam route behind the substrate is made with the lens optics. These lens optics can be adjusted to achieve the desired size of the heating laser spot on the substrate. A pyrometer is placed at the viewport (V2) to sense the temperature of the substrate. For the reproducible ablation of materials, the spot area on the surface of the target

needs to be determined precisely for computing the energy density (fluence) of the laser beam. At the focused position of the lens, the spot area on the target is 0.03 cm^2. Since there are many independent parameters for PLD growth, to reduce the complexity we have kept the lens fixed at the focus position for all depositions. A target stage is used exactly opposite to the substrate, where target holders are placed on a cone-shaped convex cup. With help of the adjuster, we can arrange the vertical position of the target stage. The multiple targets carrousel permits a number of materials to be deposited on the substrate in a single go. For *in-situ* monitoring of the growth of the film and the surface morphology, RHEED is used which is equipped with this deposition chamber. In this schematic, we have shown RHEED gun on the left side and a camera on the right side to detect the RHEED pattern. Here in this chapter of the thesis, we will mainly discuss the effect of viewports V1 and V2 on the growth of thin films.

Before deposition, the prepared TiO_2 terminated STO substrates as explained in chapter 2, were cleaned in an ultrasonic bath with acetone followed by ethanol and later dried with the nitrogen blower to avoid any contamination such as dust particles etc. Substrates were pasted on the substrate holder with silver paint and to ensure good thermal contact as well as mechanical fixation, it was dried on a hot plate for 10 minutes at 200 °C.

The substrate to target distance was kept at 50 mm. After the deposition, sample resistance was measured as a function of growth temperature. Another important parameter for thin-film growth using PLD is laser fluence, defined as laser energy per unit laser spot area. The condition of the laser viewport can significantly influence the laser fluence. A dirty viewport not only reduces the laser fluence (by reducing the energy at the target surface) but also changes the laser spot profile on the target. In this work, we will demonstrate a convenient way to judge the laser fluence situation on the target without disturbing the chamber. We will also demonstrate that multiple deposition events drastically affect the laser viewport cleanliness as well as thin-film reproducibility. An investigation of deposition time as a function of laser fluence was performed, where several samples of STO/STO were grown at various laser fluences (1.0, 1.5, 2.0, 3.0 J/cm^2) at oxygen pressure 1 ×

10^{-6} Torr. The deposition time was estimated from RHEED intensity oscillations. We plotted deposition time as a function of laser fluence. We found that after multiple deposition events, the deposition time increases although the measured laser energy before the laser viewport remains the same. This indicates a decrease in laser fluence on the target due to the dirtiness of the laser viewport. To further confirm these results on STO/STO system, heterostructures of 50 Monolayers LVO/STO at different fluence were grown at an oxygen pressure of 1×10^{-6} Torr and the growth temperature was kept at 600 °C. We found that after the multiple growths take place inside the deposition chamber, the sample which was grown at some fixed laser fluence and growth temperature is no more reproducible.

3.3 Results and discussion:

The pyrometer is placed outside the chamber and measures the temperature through a quartz viewport (V2). Here, the optical pyrometer is used. It is a non-contact type temperature measuring device. It works on the principle of matching the brightness of an object to the brightness of the filament which is placed inside the pyrometer. The accuracy of the measured temperature depends on the cleanliness of this viewport. Since the ablated atoms move in all directions, they can make this viewport dirty, and the measured temperature can easily be underestimated in compare to the actual temperature of the substrate. The aging of the viewports due to the deposition of ablated atoms is one of the major concerns for the reproducibility of the samples. We have done a thorough investigation of the two prime parameters influencing the nature of the thin films, namely, growth temperature and laser fluence. The measured sample growth temperature depends on pyrometer viewport (V2) and laser fluence, laser intensity on the target depends on the viewport (V1) through which excimer ablation laser passes as shown in **Fig. 3.4**. Both of these viewports play crucial roles in the growth of thin films. Here, we demonstrate a simple way to keep the temperature calibrated and hence know the status of the pyrometer viewport and ablation laser viewport

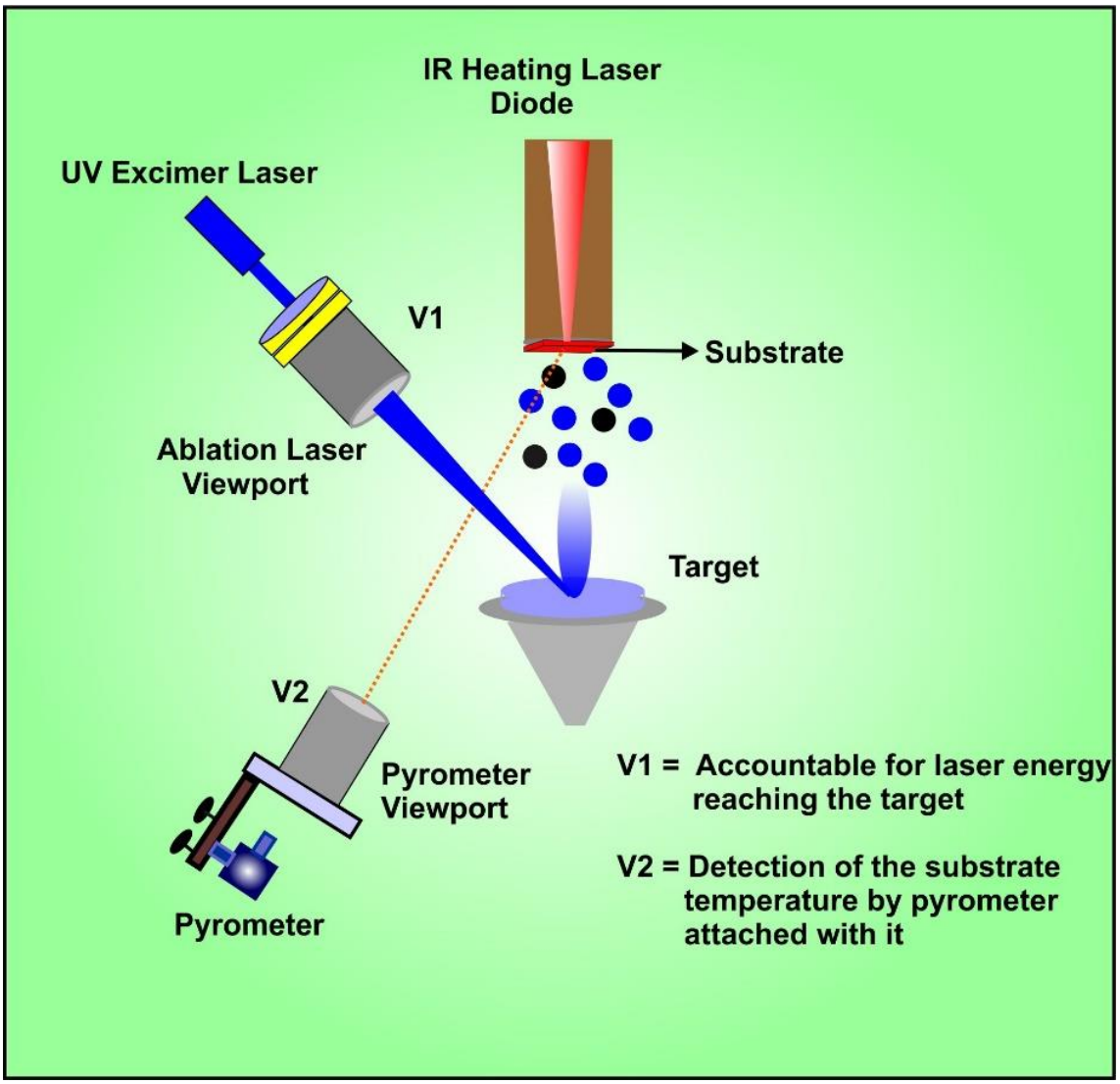

Figure 3.4: Schematic of the ablation laser viewport (V1) and pyrometer viewport (V2) that got contaminated after multiple depositions and play an important role to reproduce samples.

Here, we have done three different case studies to know the exact *in-situ* and *ex-situ* growth parameters for thin film depositions as follows:

3.3.1 STO-STO Combinatorial growth

3.3.2 STO-STO Homoepitaxial growth

3.3.3 LVO-STO Heteroepitaxial growth

3.3.1 STO-STO Combinatorial growth

A growth of temperature gradient STO-STO deposition was performed. The IR heating laser was focused at one end of the substrate and the temperature at this end was raised to 830 °C, as schematically shown in **Fig. 3.5 (a)**. We have shown a schematic and real picture of a 10 x 2 mm STO sample. Due to thermal conduction, the other end of the substrate gets heated up and the temperature of this end was measured to be 630 °C. The temperature of the substrate was measured by focusing the pyrometer on the substrate and identifying the measurement position with the help of guiding laser light.

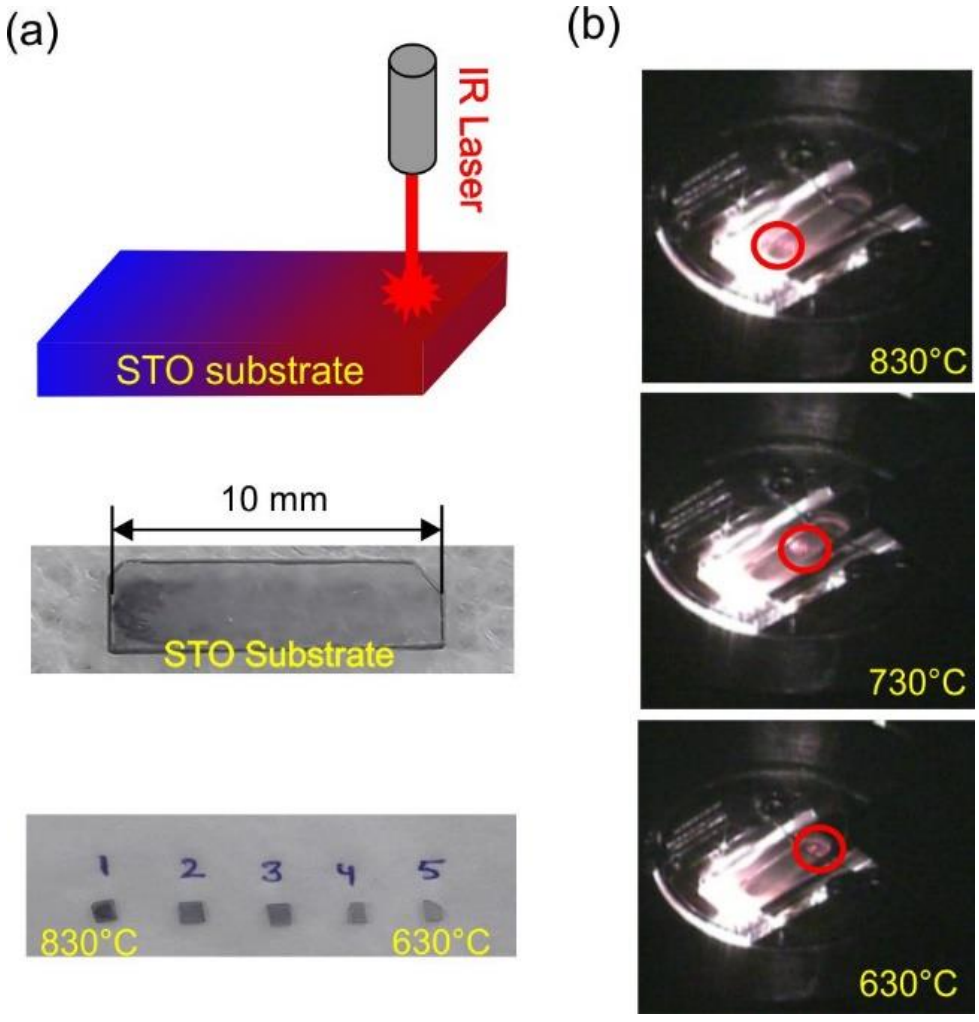

Figure 3.5: (a) Schematic and real picture of the temperature gradient combinatorial growth on STO substrate with a temperature difference of 200°C from one edge of the substrate to the other. (b) The solid line circle with red color shows the position of the pyrometer laser light for temperature detection throughout the sample.

Forty monolayers of STO on TiO_2 terminated STO (001) substrate (10 mm × 2 mm) were grown using laser fluence of 1.8 J/cm^2 and oxygen partial pressure (PO_2) 3.6 × 10^{-6} Torr. The laser beam was kept a bit off-centered on the STO target with a spot area 0.03 cm^2, to avoid continuous ablation from the same place. The resistance of the substrate was checked by making its 5 parts, each of 2 mm in length as shown in **Fig. 3.5 (a)**. The variation in the growth temperature with the distance from one end of STO sample to the other end is shown in **Fig. 3.6.**

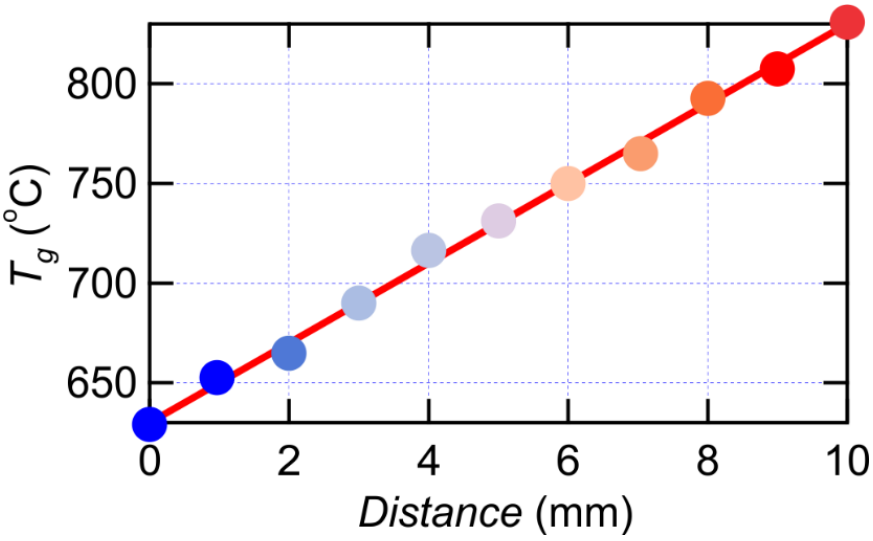

Figure 3.6: Scaling of the growth temperature from one edge of the substrate to another edge.

Next, we have done the electrical and optical study of these different samples. We measure the electrical resistance of the sample by using a multi-meter and UV-VIS is done to find the optical band gap energy. **Figure 3.7 (b)** shows the resistance measured at different positions on the sample, the different points of the sample correspond to different growth temperatures. Our measurements clearly indicate that at around 770 °C, there is a sharp decrease in resistance and that is the transition temperature. The green and purple shaded areas show low and high resistance, respectively. The band gap values come out to be 3.03, 3.02, 2.99, 2.98 and 2.85 eV at growth temperatures 630, 680, 730, 780, and 830 respectively.

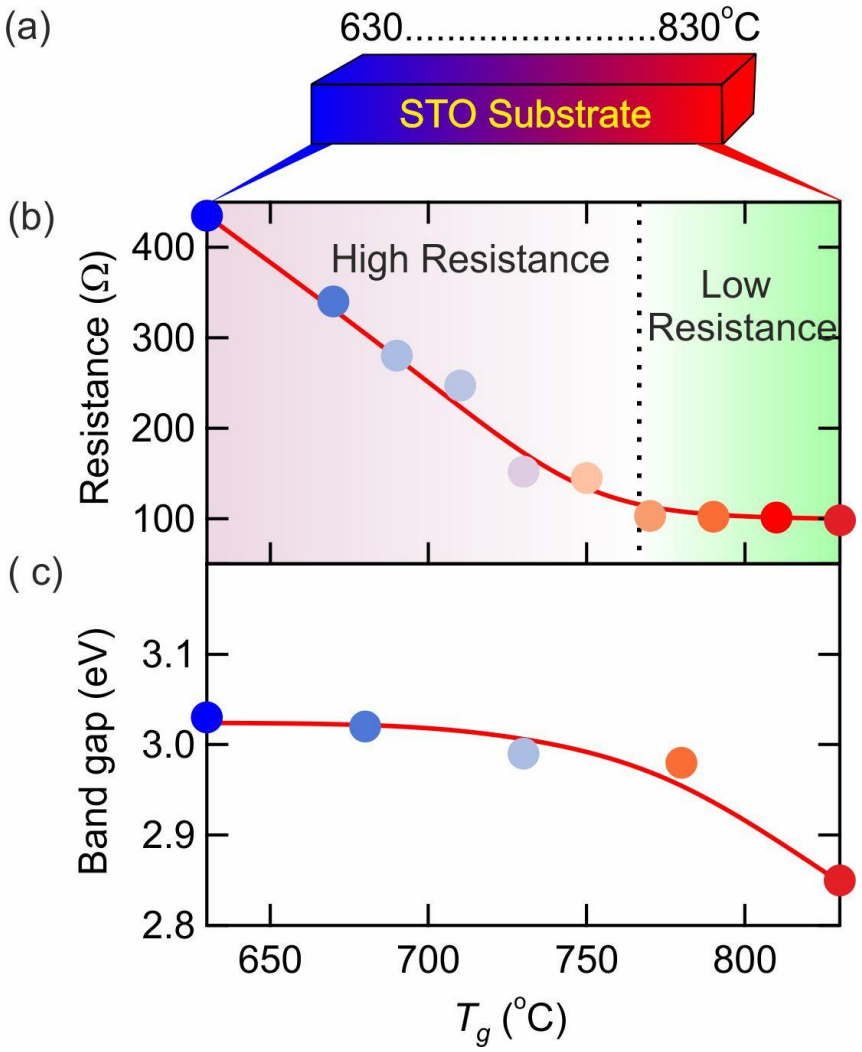

Figure 3.7**:** (a) Schematic of the temperature gradient STO-STO sample (b) Resistance vs growth temperature (T_g) plot of STO on (001) oriented STO substrate by the single shot film growth method. The black dotted line shows the transition temperature @770 °C. (c) Optical band gap vs growth temperature curve for these STO-STO samples.

As the sample becomes higher conducting with growth temperature, the energy band gap starts decreasing. From this temperature gradient combinatorial study, we are able to find the growth temperature for STO-STO deposition. We will fix this growth temperature for our next study of STO-STO fluence-dependent homoepitaxial growth.

3.3.2. STO-STO Homoepitaxial growth

To standardize and optimize the system with respect to the growth temperature and laser fluence, a homo-epitaxial growth of STO thin films on STO has been chosen as the first deposition in the chamber. There are several advantages of choosing this particular homo-epitaxial growth. First of all, STO-STO growth is well documented in the literature and

hence, easy to compare [20-23]. It is reported that by tuning the ablation laser energy, the growth mode deposition time can be tuned. This growth rate can be used as a scale to identify the laser energy on the target surface. Also, by increasing the growth temperature, a transition from high resistance(insulating) to a low resistance(conducting) STO film can be achieved [24-28]. The growth temperature at which this transition occurs can be taken as a characteristic temperature of that deposition chamber [29-30].

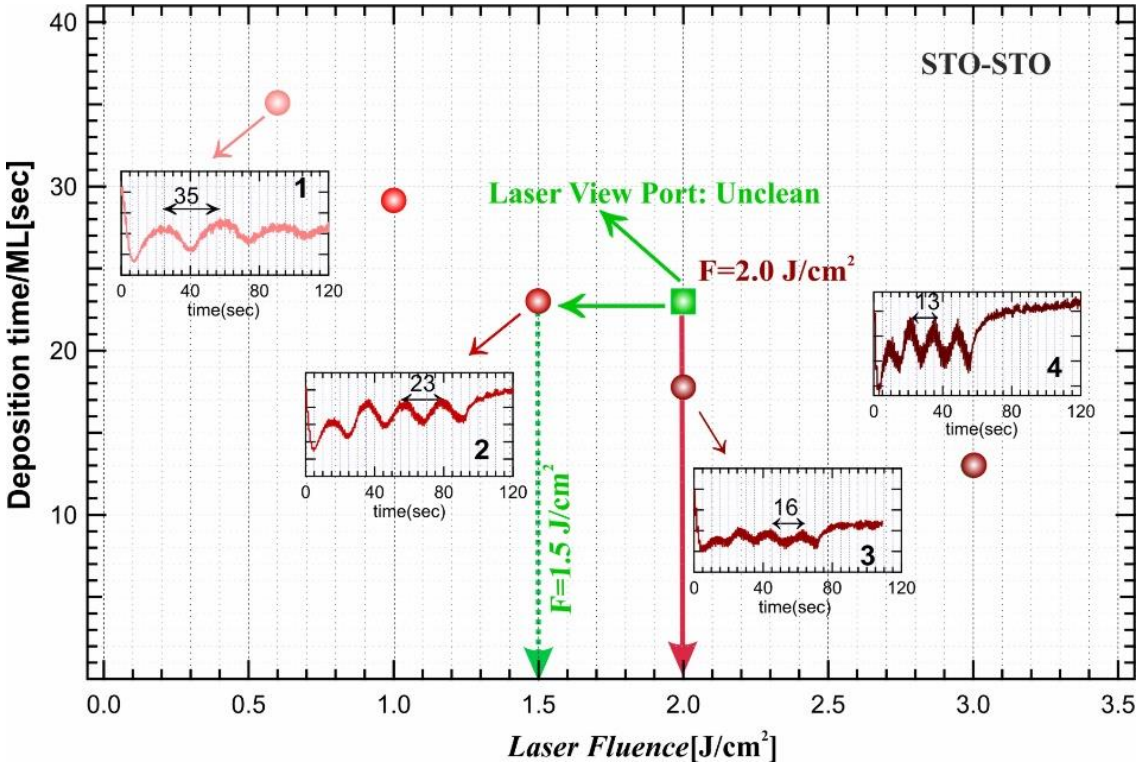

Figure 3.8: Deposition time per monolayer as a function of laser fluence for STO-STO system.The circles denote the deposition time per monolayer for this system when viewport was clean.The insets 1, 3 and 4 show the RHEED oscillations for the samples grown at 0.5, 2.0 and 3 J/cm^2, respectively.The green square represents the deposition time per monolayer for the sample grown at 2 J/cm^2 when the viewport gets unclean. Inset 2 shows the RHEED oscillations for the same which shows that time for the one monolayer is increased.

Here, we have deposited STO thin films on STO substrate at different laser fluences, keeping the deposition temperature (770 °C) constant. The fluence was varied by changing the laser energy while the spot size was kept constant. We have plotted the deposition time per monolayer for all the samples grown at different laser fluences. **Figure 3.8** shows the deposition time as a function of laser fluence suggesting a decrease

in deposition time as the laser fluence is increased. In the inset from 1 to 4 of Figure 3.8, the RHEED intensity oscillations vs time plot is shown. Here, the deposition time per monolayer (sec) increases with the decrease in fluence because, at low fluence, the particles are being ablated with low kinetic energy so it takes more time to form a complete atomic monolayer. To reconfirm this, we have grown samples for selected fluences for 40 minutes and fixed it for all the growths.

After the deposition, an AFM scan was performed near the boundary that provides us with the estimation of film thickness. The line scan is also presented adjacent to the AFM image as shown in **Fig. 3.9**. We found that with the increase in laser fluence the surface morphology changes. For these samples, we have covered half part of the substrate with a mask during deposition. To identify this region after the growth, we made a mark on the other side of the substrate.

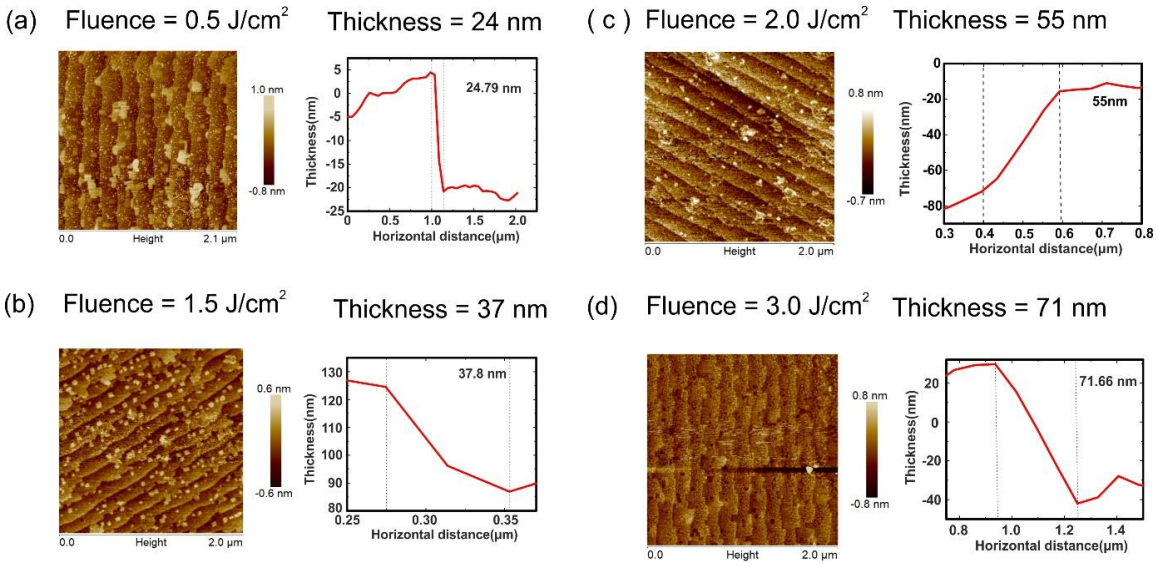

Figure 3.9: (a), (b), (c) and (d) are the AFM images of the STO-STO samples grown at laser fluences 0.5, 1.5, 2 and 3 J/cm^2 respectively with adjacent height profile of thin film.

Thicknesses are found to be around 24, 37, 55 and 71 nm for the fluences 0.5, 1.5, 2.0 and 3.0 J/cm^2 respectively. The growth rate at a particular laser fluence was recalculated from this data and found to be very similar to that revealed from RHEED intensity oscillations. Now, after around sixty thousand pulses of depositions of different materials in the chamber if we try to reproduce the STO-STO sample with the same growth parameters then it was observed that this curve of deposition time per monolayer vs fluence shifts upward as shown in **Fig. 3.8** with the green square box. This observation suggests that

even if we fix a fluence of 2 J/cm^2, the deposition time is now increased to that corresponding to the laser fluence 1.5 J/cm^2. This suggests that the energy that was fixed outside is not the same as inside the main chamber, but rather lower. The reason for the decrease in energy is that the ablation laser viewport (V1) is getting dirty due to the deposition of ablated atoms. Such a situation clearly demands a need to clean this viewport to achieve reproducible samples.

From the resistance vs growth temperature curve in **Fig. 3.10**, the data for the clean viewport shows the transition temperature at 770 °C. After around sixty thousand pulses of depositions in the PLD chamber, we performed the same deposition with the same growth parameters. We have seen that the transition temperature is now moved to a lower value of measured growth temperature nearly 720 °C as shown with the blue square box in **Fig.3.10.**

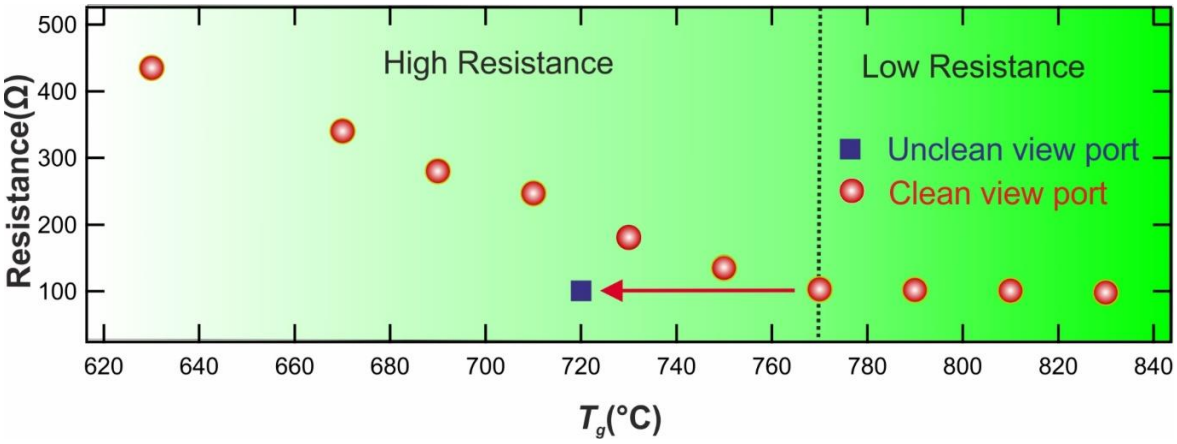

Figure 3.10: Temperature dependence of resistance with a clean and unclean viewport for the STO-STO system. The black dotted line shows the transition growth temperature for this system.

The reason for this shift is the contamination of the pyrometer viewport (V2). During the deposition process, ablated species scatter throughout the main chamber and make the viewports dirty. Therefore, the sensor of the pyrometer is not able to detect the actual temperature of the substrate and underestimates it. So, from this study, we have analyzed a way to know the exact growth parameters inside the main deposition chamber of the PLD system. We have devised a way that at what time we need to clean our PLD system or how we can manipulate the exact growth parameters without breaking the high vacuum of the chamber.

3.3.3 Heteroepitaxial growth (LVO-STO)

Next, we had taken a heteroepitaxial system, where LVO thin films are grown on TiO_2 terminated (001) oriented STO single crystal substrate. This is an important heterostructure of a Mott-insulator LVO and band-insulator STO, where the interface hosts a high mobility 2DEG. Initially, an optimization of laser energy is performed to realize the conducting interface of LVO and STO. **Figure 3.11 (a)** represents the deposition time per monolayer vs fluence for the LVO thin film growth. As the fluence is increased from low to high, the system shows insulating to metal transition. The laser fluence of 1.2 J/cm^2 is the fluence where this transition takes place and above this fluence, the system remains conducting in nature. Here, circles and squares represent the deposition time at different laser fluences when the viewport is clean and unclean due to around seventy thousand laser pulse depositions inside the chamber, respectively. The insets from 1-3 show the RHEED oscillations. M_b is the sample grown with fluence 1.2 J/cm^2 depicts the conducting behavior with a clean viewport. We found that after a larger number of depositions in the chamber, with the same growth conditions at which metallic samples were realized, is now producing an insulating sample and is marked as I_a, suggesting an effective decrease in laser energy on the target surface due to the deposition of ablated species on the viewport. Inset 4 shows the RHEED oscillations for the sample deposited with the energy that should produce more than 1.2 J/cm^2 fluences on the target surface. This energy was measured just outside the laser viewport (V1), but we found that the time period for one-layer deposition is now increased and matches with the time period for 0.95 J/cm^2. At the same time, this sample turned out to be insulating in nature. Metallic and insulating behavior is shown in **Fig. 3.11 (b)** where after contamination of viewports, the physical properties of the sample changed. Here, if we try to reproduce the sample of LVO-STO with the same growth conditions after multiple depositions, its physical properties change or the sample becomes insulating in nature as shown by red color dark lines. The green solid curve confirms the metallic nature of the sample at the initial stage.

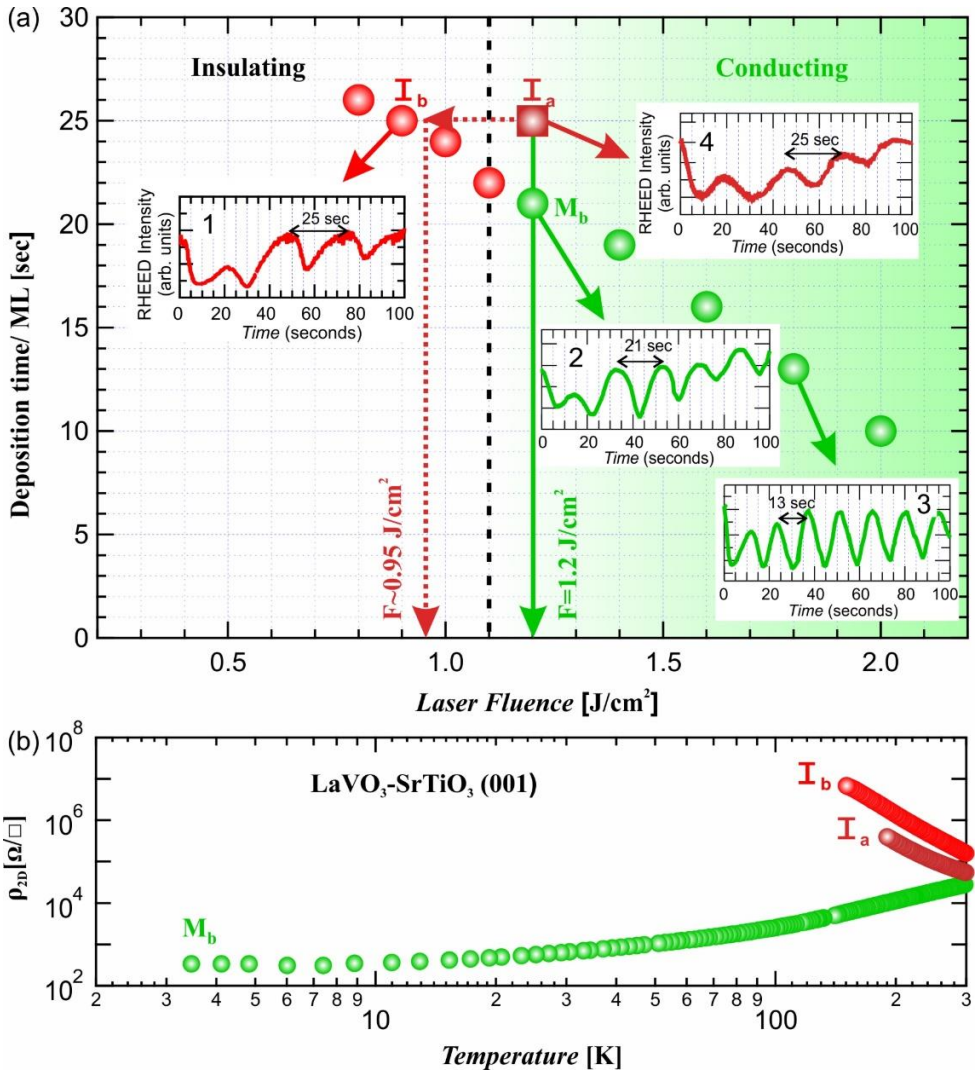

Figure 3.11**:** (a) Deposition time per monolayer as a function of laser fluence for LVO-STO system. The black dotted line represents laser fluence driven by a metal-insulating transition for LVO-STO. The circles denote the deposition time for this system when the viewport was clean. The insets 1, 2, and 3 show the RHEED oscillations for the samples grown at 0.8, 1.2, and 1.8 J/cm^2, respectively. The sample grown at 1.2 J/cm^2 is named M_b (clean viewport condition). The square represents the deposition time for the sample grown at 1.2 J/cm^2 when the viewport gets unclean and is named I_a. Inset 4 shows the RHEED oscillations of the same. The sample named I_b is grown at 0.8 J/cm^2. (b) Temperature dependence of sheet resistance for three cases discussed in (a).

These two observations clearly suggest that the laser energy on the target surface is less than expected due to the dirty laser viewport. T. Ohnishi *et al*. suggested that governing reason for transmittance fall at the entrance viewport during the film growth favours the Lambert's law

showing the change in absorption in preference to reflectivity. Also, the ablation laser fluence shows an influential impact on the lattice constant and structure of thin films [31].

Laser fluence could be tuned by both laser energy and spot size area. The stoichiometry of the deposition film could be changed by varying the fluence or by changing the laser energy and spot size. One of similar work has been done for LVO-STO heterostructure. Ruchi Tomar et al. have grown the LVO-STO interface by varying the laser fluence and they observed that the physical state of sample can be changed from insulating to conducting by varying the stoichiometry of the material. They found that La-deficiency in LVO film is mandatory to produce the conducting interface LVO and STO. They turned the stoichiometry with the help of varying laser fluence. At high fluence, the sample is La-deficit and interface turn out to be conducting. It is suggested that conducting interface with La-deficiency have a larger c-axix than stoichiometry LVO. Such expansion in crystal lattice might have produced some internal electric field that in turn has triggered the polar catastrophe to create electron-doped conducting interface.

Reproducibility is a concern due to the heavy coating on the viewports from the successive depositions. It is hard to achieve reproducibility if the actual growth temperature and ablation energy differ due to the coating on the viewports.

3.4 Conclusion

In conclusion, we have demonstrated the significance of measuring the exact growth temperature and laser energy inside the chamber to realize reproducible samples using PLD thin film growth technique. We have provided a guideline to detect deviations in growth temperature at the substrate and laser energy on the target without breaking the vacuum. With an example of the STO-STO and LVO-STO interface, we have demonstrated that the physical properties of the material can be changed significantly due to the change in growth condition inside the chamber, which may apparently appear the same when measured from outside. Our work is not restricted to any material system, but can be used as a guideline for any oxide material thin film growth using PLD technique. In particular, we would like to emphasize that the size, shape and intensity of the ablation laser on the target surface has a significant influence on the cation stoichiometry. In addition, an unintentional wrong reading of growth temperature may lead to irreproducible samples. Such irreproducibility might be avoided by employing our prescribed method. Also, by using different combinatorial method, we can grow superlattices and composition gradient thin films that is highly useful in medical industry.

Bibliography:

[1]. A. Samnri, M. Radovic, X. Wang, S. Amoruso, F.M. Granozio and R. Bruzzese, *Appl. Surf. Sci.*, **254**, 790 (2007).

[2]. D.H.A. Blank, M. Dekkers and G. Rijnders, *J. Phys. D: Appl. Phys.*, **47,** 034006 (2014).

[3]. T. Ohnishi, M. Lippmaa, T. Yamamoto, S. Meguro and H. Koinuma, *Appl. Phys. Lett.*, **87**, 241919 (2005).

[4]. H.K. Sato, C. Bell, Y. Hikita and H.Y. Hwang, *Appl. Phys. Lett.*, **102**, 251602 (2013).

[5]. S. Wicklein, A. Sambri, S. Amoruso, X. Wang, R. Bruzzese, A. Koehl and R. Dittmann, *Appl. Phys. Lett*., **101**, 131601 (2012).

[6]. R. Tomar, R.M. Varma, N. Kumar, D.D. Sarma, D. Maryenko and S. Chakraverty, *Adv. Mater. Interfaces*, **7**, 6 (2019).

[7]. E. Breckenfeld, N. Bronn, J. Karthik, A.R. Damodaran, S. Lee, N. Mason and L.W. Martin, *Phys. Rev. Lett*., **110**, 19 (2013).

[8]. A. Ohtomo and H. Y. Hwang, *J. Appl. Phys.*, **102**, 083704 (2007).

[9]. E. Breckenfeld, R. Wilson, J. Karthik, A.R. Damodaran, D.G. Cahill and L.W. Martin, *Chem. Mater*., **24**, 331 (2012).

[10]. J. H. Song, T. Susaki and H. Y Hwang, *Adv. Mater*., **20**, 2528 (2008).

[11]. R. Castro-Rodriguez, D. Coronado, A. Augusto, B. Watts, F. Leccabue and J. L. Pena, *Appl. Phys. A* , **81**, 1503 (2005).

[12]. H. N. Lee, Sung S. Ambrose Seo, W. S. Choi and C. M. Rouleau, *Sci. Rep.* , **6**, 19941 (2016).

[13]. L. Gorup, V. Bouquet, S. Députier, V. Dorcet, M. Guilloux-Viry, L. Santos, A.A. Silva, A. Nogueira, A. Kubo, E. Longo and E. Camargo, *Ceram. Int.*, **45**, 3510 (2018).

[14]. H. Krebs, M. Weisheit, J. Faupel, E. Su¨ske, T. Scharf, C. Fuhse, M. Sto¨rmer, K. Sturm, M. Seibt, H. Kijewski, D. Nelke, E. Panchenko and M. Buback, *Adv. Phys.*, **43**, 101 (2003).

[15]. X.H. Xu, R.Q. Zhang, X.Z. Dong and G.A. Gehring, *Thin Solid Films*, **515**, 2754 (2006).

[16]. C. Xu, S. Wicklein, A. Sambri, S. Amoruso, M. Moors and R. Dittmann, *J. Phys. D: Appl. Phys.*, **47,** 34009 (2014).

[17]. N. Kumar, R. Gupta, R. Kaur, D. Oka, S. Kakkar, S. Kumar, S. Singh, T. Fukumura, C. Bera and S. Chakraverty, *ACS Appl. Electron. Mater.*, **3**, 597 (2021).

[18]. V. Craciun, D. Craciun, I. N. Mihailescu, G. Socol, N. Stefan, M. Miroiu, A. C. Galca and G. Bourne, *Power Laser Ablation VII*, **vol. 7005** of *Proceedings of SPIE* (2008).

[19]. T. Koida, D. Komiyama and H. Kawasaki, *Appl. Phys. Lett.*, **80**, 565 (2002).

[20]. D.A. Tenne, I. E.Gonenli, A. Soukiassian, D.G. Schlom, S.M. Nakhmanson, K.M. Rabe and X.X. Xi, *Phys. Rev. B.*, **76**, 024303 (2007).

[21]. C. Lee, J. Destry and J. L. Brebner, *Phys. Rev. B*, **11**, 2299 (1975).

[22]. Z. Huang, Z. Q. Liu, M. Yang, S. W. Zeng, A. Annadi, W. M. Lü, X. L. Tan, P. F. Chen, L. Sun, X. Renshaw Wang, Y. L. Zhao, C. J. Li, J. Zhou, K. Han, W.B. Wu, Y.P. Feng, J. M. D. Coey, T. Venkatesan and Ariando, *Phys. Rev. B*, **90**, 125156 (2014).

[23]. D. Muller, N. Nakagawa and A. Ohtomo, *Nature*, **430**, 657 (2004).

[24]. D. J. Groenendijk, S. Gariglio, *J. Appl. Phys.***, 120**, 22 (2016).

[25]. M. Lippmaa, N. Nakagawa, M. Kawasaki, S. Ohashi and H. Koinuma, *Appl. Phys. Lett.* , **76**, 17 *(2000).*

[26]. N. Jaber, J. Wolfman, C. Daumont, B. Négulescu, A. Ruyter, T. Sauvage and F. Gervais, *Thin Solid Films*, **634**, 107 (2017).

[27]. A. Al-Tawhid, J.R. Frick, D.B. Dougherty and D.P. Kumah, *J. Vac. Sci. Technol. A.*, **37**, 2 (2019).

[28]. L. Wang, Y. Yang, J. Zhao, B. Hong, K. Hu, J. Peng, H. Zhang, Z. Luo, X. Li and C. Gao, *J. Appl. Phys.*, **119**, 14 (2016).

[29]. A. N. Khodan, S. Guyard, J.-P. Contour, D.-G. Crete, E. Jacquet and K. Bouzehouane, *Thin Solid Films***, 515**, 6422 (2007).

[30]. K. Szot, W. Speier, R. Carius, U. Zastrow and W. Beyer, *Phys. Rev. Lett*., **88**, 75508 (2002).

[31]. T. Ohnishi, H. Koinuma and M. Lippmaa, *Appl. Surf. Sci.*, **252**, 2466 (2006).

Chapter 4

Photoconductivity of EuO-KTO interface: Effect of intrinsic carrier density and temperature

4.1 Introduction

The discovery of conducting interface of LAO-STO opens up new dimensions both for fundamental and applied physics [1-3]. Besides having high mobility, this 2-dimensional electron gas (2DEG) also possesses other interesting properties like magnetism, superconductivity, quantum Hall effect, planar Hall effect, electric field tuning, etc [4-13]. This leads researchers towards the search for other novel STO-based heterostructures, and several interesting oxides conducting interfaces are realized, namely, $LaVO_3$ (LVO)-$SrTiO_3$ (STO), $LaTiO_3$ (LTO)-STO, $LaGaO_3$ (LGO)-STO, $NdGaO_3$ (NGO)-STO, etc [14-19]. The 2DEG of these STO-based heterostructures has received tremendous attention due to exotic physics and prospective applications in spintronics and optoelectronic devices.

The large spectrum of extraordinary properties at these conducting heterostructures stems from the interaction between orbital, charge, lattice, and spin degrees of freedom which may be used to integrate new electronic devices with properties different from those known today. The interplay between these degrees of freedom also leads to changes in the electronic, magnetic, and structural properties upon using external stimuli. Here, the conductivity of these interfaces can be tuned by using different external perturbations such as light illumination, back gating, applying a magnetic field, polar adsorbate, ion bombardment, stress, strain, etc [2,7,10,13-16, 20-22]. But, the most used external stimuli is the light illumination on the sample surface. Light illumination can generate electron-hole pairs, that not only contribute to the conductivity but also affect the diffusion of oxygen vacancies and hence modifies the transport properties [23,24].

Tuning the conductivity of 2DEG using light (Photoconductivity) has attracted considerable interest because of promising optoelectronic applications [12, 25-26]. Optoelectronic devices have emerged as viable candidates for a variety of applications such as energy conversion devices, memory devices, sensors, biomedical optical technologies, holography, image, array, etc [27-31]. Here various optoelectronic effects such as saturation absorption, photoconductive switching, photo-capacitive effect, and persistent photoconductivity (PPC) enable the customization of responses for the implementation of next-generation technology [32-34]. Conductivity is a crucial parameter that plays an important role in the appropriate operation and control of these types of optoelectronic devices. So, it is necessary to develop a control mechanism for various parameters such as conductivity, mobility, and a trap-assisted lifetime of electrons and holes of the component materials that are used in the manufacturing of these devices. The type of carriers that are responsible for the conductivity are free carriers. These free carriers can be incorporated using doping as well [35,36].

Photoexcitation is a type of conduction where carriers are generated by optical excitation. Photoconductivity (PC) is a well-known optical and electrical phenomenon in semiconductors. It is an effect caused by electromagnetic radiation absorption that increases electrical conductivity. Photo carriers can also be generated through sub-band gap excitation. Generally, excitation occurs when incoming light has an energy greater than or equal to the band gap of the exciting material, causing electrons to transfer to the conduction band or excitation of the impurities inside the band gap, resulting in the formation of electron-hole pairs.

Photovoltaic effect: The output electrical energy produced is proportional to the intensity of light. The effect due to which light energy is converted to electric energy in certain semiconductors materials is known as photovoltaic effect. When a cell is exposed to sun, the negatively charged electrons in the cell get energized by absorbing small energize particles in the light called photons. This cause the electrons to flow and thus electric current can be produced.

Photoconductive effect: When enough amount of light intensity falls on the semiconductor materials, the photons in the light intensity energize the electrons in the semiconductor's material to jump from its valence band to the conduction band. This cause to decrease in the resistance of the material, thereby increasing the current flow.

The percentage change in resistance increases with an increase in power intensity and decrease with an increase in the wavelength of visible light.

Persistent photoconductivity (PPC) is a photo-induced mechanism that persists even after the removal of light excitation. It means that photo-response does not cease immediately but rather stays available for a while (milliseconds to hours) after the illumination is removed. Because of the ability to control the gradual decay of charge carriers after the light is turned off, photo-response can be used in designing novel applications. PPC has already been reported in conventional semiconductors such as n-GaAs layers, AlGaAs-GaN, GaN nanowire, and silicon membranes, etc. [37-40], but their practical application is limited by low operation temperature or low amplitude of the PC and PPC. This effect has been measured in oxide systems too: photo-induced conductance value is increased by 5 orders of magnitude for LAO-STO interface at room temperature, much higher than the one observed in conventional semiconductor heterostructure [25]. So, complex oxide surfaces and interfaces are of great importance for optoelectronic applications. It is also reported that growth parameters, doping, and surface treatment play a vital role in photo-response and relaxation dynamics at different complex oxide interfaces [41-47]. Apart from this, organic compounds and materials with photoconductive properties have importance in many technological as well as biological applications such as photodetection, dye-sensitized solar cells, smart drug-delivery systems, molecular electronics, etc [48-53].

Recently, $KTaO_3$ (KTO) based conducting interfaces have gained tremendous interest because the spin-orbit coupling strength is one order of magnitude higher than STO which makes it a promising candidate for spintronic applications [54]. Out of all the conducting interfaces reported on KTO, EuO/KTO interface is only a non-perovskite/ perovskite interface. The origin of conductivity at this interface is still not clear, nevertheless, it shows very interesting phenomena like Shubnikov-de Hass oscillations, anomalous magnetoresistance, planar hall effect, and PC [55,56]. But, the effect of light on the interfacial conductivity of this interface with different intrinsic carrier densities and at low temperatures is not reported.

In this chapter, we have discussed the photo-response behavior on samples of EuO-KTO (001) with different intrinsic carrier densities prepared at different growth conditions. We

have shown that lowering the carrier density increases the photo response in this system. At room temperature, the photo response consists of two processes. But at low temperatures, it is not only governed by a single process, in addition, the response rate also becomes several orders of magnitude faster. At the same time, the magnitude of photo response is also larger at low temperatures. Our observation suggests an interplay between the carrier and phonon dynamics determines the photo-response and should be investigated theoretically in detail to design future photo-responsive cells. Surprisingly an order of magnitude larger and 2 orders of magnitude faster light response has been observed at lower temperatures in comparison to room temperature.

4.2 Experimental method

For the study of the effect of light illumination on the transport properties of the EuO-KTO interface, we have grown multiple EuO thin films on KTO (001) substrates under different growth conditions. We had seen that the carrier density of the interface can be tuned by growing at different growth conditions. Thin films of EuO were grown on Ta-terminated KTO single crystal using a pulsed laser deposition system. Before the deposition, we annealed the KTO substrate at 600 °C for 4 hours in the air. All the samples were grown using a constant fluence of 4 J/cm^2 and a repetition rate of 2 Hz. The oxygen partial pressure and temperature were varied to prepare different samples. The thickness of these films was monitored using the reflection high-energy electron diffraction (RHEED) technique and was kept to 25 monolayers (ML) corresponding to about 10 nm thickness.

The carrier density and the mobility of the samples were measured using a Dynacool Quantum Design physical properties measurement system (PPMS) and a Four probe Cryostat station was used to measure the conductance of the sample at low temperatures. For a well-defined measurement geometry, gold strips were deposited on the sample using a metal hard mask as shown in section 2.4 of chapter 2. For various electrical connections, we used an ultrasonic wire bonder with an Al wire. In this experiment, two laser beams with wavelengths of 532 nm and 405 nm (green and blue color respectively) with selected power have been used to illuminate the sample. Laser light of spot size radius 1.34 nm was irradiated on both samples with a channel size of

around 0.5 x 3.0 mm. A source meter is used to supply the voltage and current and a power meter is used for measuring the light power intensity.

4.3 Results and Discussion

4.3.1 Growth and Transport properties

The bulk EuO phase crystallizes in a cubic structure with a lattice constant of 5.145 A°. KTO is also cubic with a lattice constant of 3.989 A°. Due to this difference in the lattice constant of the two oxide materials, epitaxial growth is not possible because of the large lattice mismatch. For epitaxial growth on KTO, the EuO lattice will rotate along the (001) axis by 45° as shown in schematic **Fig. 4.1(a)** and confirmed by the RHEED pattern **Fig. 4.1(b).** Three different RHEED patterns confirm the epitaxial growth of EuO on the KTO substrate shown in **Fig. 4.1(b).** KTO (001) was the initial position, but when rotated along 45 degrees, we get KTO (110) surface. The growth of EuO thin film on KTO is shown by the nice bottom RHEED pattern in this figure.

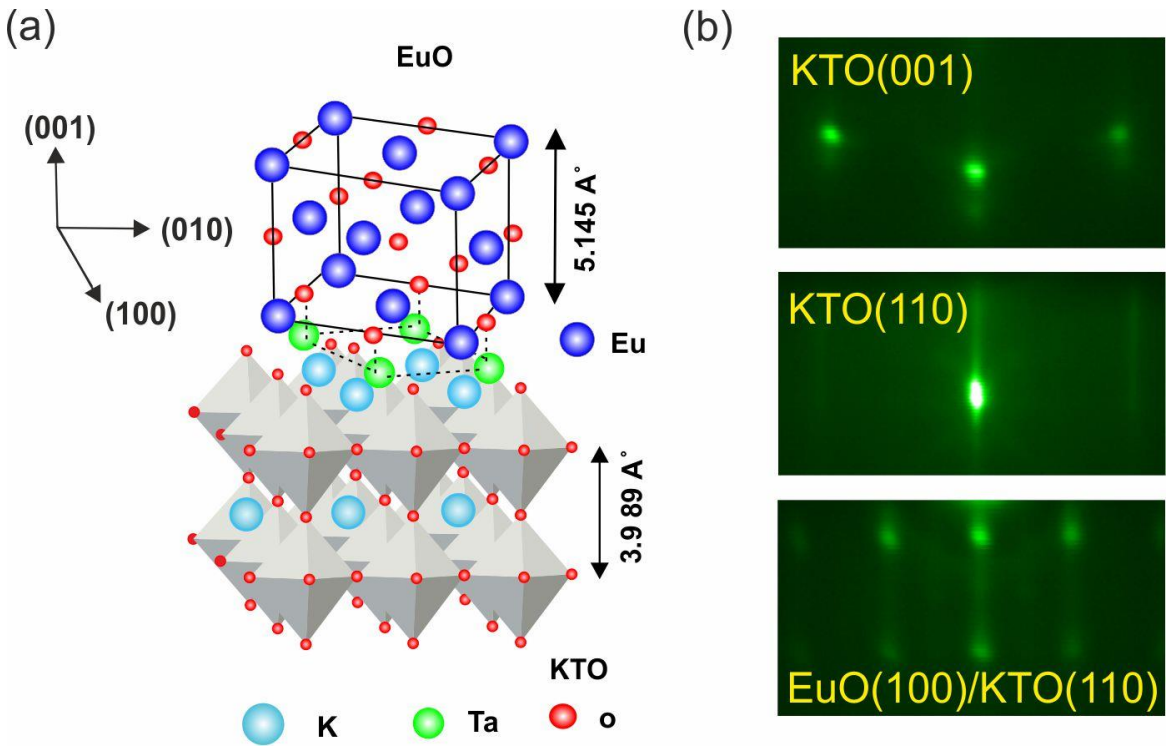

Figure 4.1: (a) Schematic of the crystal structure of EuO on KTO with 45° rotation along the (001) axis. (b) Real picture of the RHEED patterns of EuO film and KTO substrate.

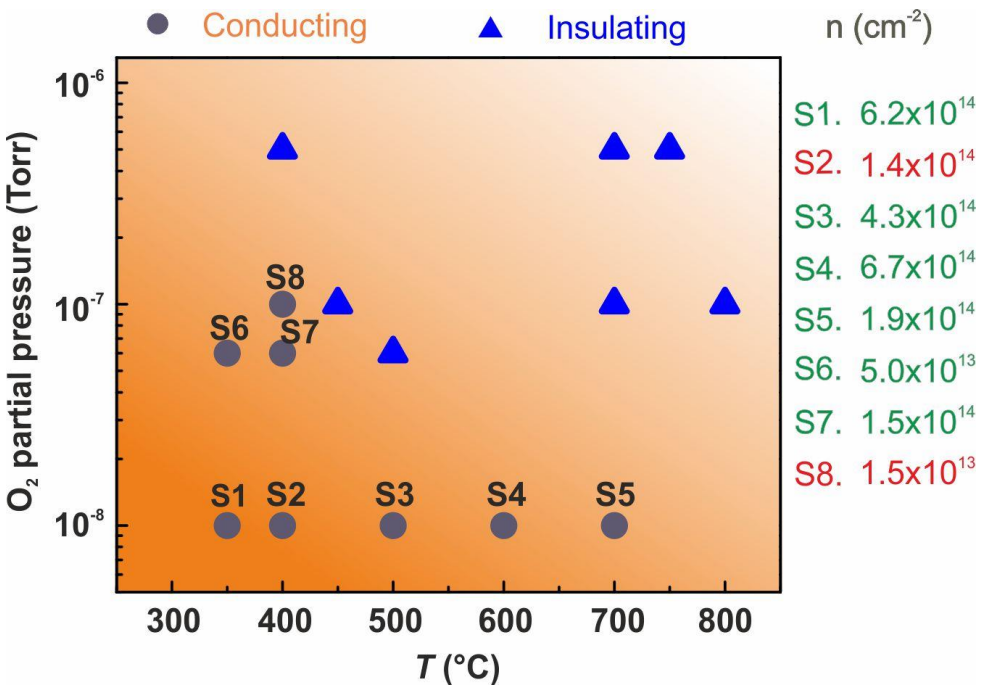

Figure 4.2: Optimization plot for growth showing the conducting and insulating region. Conducting samples are shown from S1 to S8 with solid circle points. Blue triangles denote the samples that are insulating in nature. On the right side, the carrier density value is written for each conducting sample. Photo-response study is done on samples S2 and S8 highlighted in red color.

In **Figure 4.2**, we have shown the optimization plot of the multiple samples of EuO-KTO grown at different parameters, where it is found that as we increase the growth temperature and oxygen partial pressure keeping the fluence constant, the samples turn out to be insulating in nature. Samples S1 to S8, which are found to be conducting in nature are shown by solid circles, and samples that are insulating in nature are shown by blue solid triangles. The carrier density of each sample at room temperature is written on the right side of this figure which is calculated from the Hall measurement.

The growth conditions and carrier density of all the conducting samples are mentioned in **Table 4.1**. In this chapter, we have reported the photo-response behavior of the S2 and S8 samples, one with a high carrier density and another with a low carrier density respectively (highlighted with color in Table 4.1). Both samples show the signature of the anomalous Hall effect when we do the transverse measurement. Carrier density is measured by fitting only the high field part of the Hall data as shown in **Fig. 4.3,** where we have calculated the density for samples S2 and S8.

R_H is the Hall coefficient (the slope of the curve). Here the carrier density is calculated using the formula:

$R_H = \frac{1}{ne}$, where n is the carrier density and e is the charge on the electron.

Sample no.	Growth Temperature(°)	Growth O_2 partial pressure (Torr)	Carrier density (cm^{-2})
S1	350	$1x10^{-8}$	$(6.2 \pm 0.008) \times 10^{14}$
S2	400	$1x10^{-8}$	$(1.4 \pm 0.012) \times 10^{14}$
S3	500	$1x10^{-8}$	$(4.3 \pm 0.019) \times 10^{14}$
S4	600	$1x10^{-8}$	$(6.7 \pm 0.168) \times 10^{14}$
S5	700	$1x10^{-8}$	$(1.9 \pm 0.007) \times 10^{14}$
S6	350	$6x10^{-8}$	$(5.0 \pm 0.001) \times 10^{13}$
S7	400	$6x10^{-8}$	$(1.5 \pm 0.002) \times 10^{14}$
S8	400	$1x10^{-7}$	$(1.5 \pm 0.016) \times 10^{13}$

Table 4.1: Growth parameters and carrier density of the conducting samples.

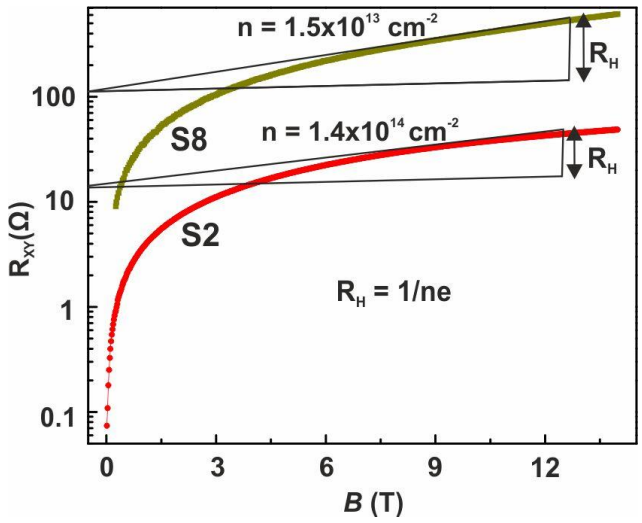

Figure 4.3: Room temperature Hall measurement of the samples S2 and S8 shown by different colors. R_H is the Hall coefficient from where carrier density can be calculated.

Next, we have done the temperature-dependent transport measurement. The normalized conductance vs temperature data for both the samples in dark and under blue light is shown in **Fig. 4.4**. This photo-response at different temperatures is studied under a laser light of wavelength 405 nm with the power of 0.5 mW. The conductance change is

observed higher for the sample with lower carrier density and this change increases continuously as we go from room temperature to lower temperature as shown in **Fig. 4.4**.

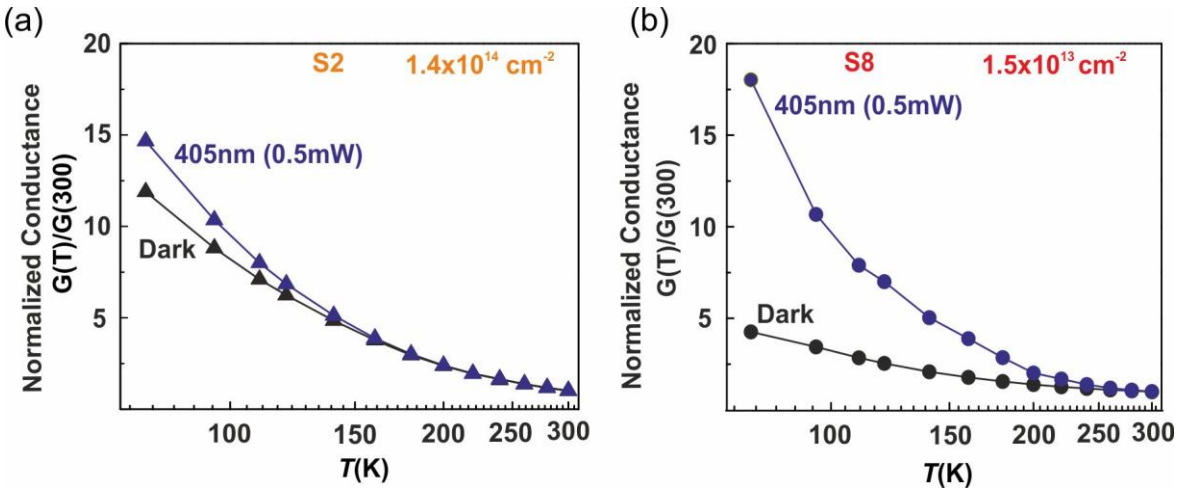

Figure 4.4: (a) Normalized conductance vs temperature curve for sample S2 with higher carrier density in dark and in presence of light (b) Conductance vs temperature curve for sample S8 with lower carrier density in dark and light mode.

4.3.2 Photo-response

In these experiments, first, the sample was kept in dark until the resistance of the sample becomes constant. Then laser light with a power of 0.5 mW was illuminated on the sample as shown in the schematic **Fig. 4.5** for 5 min and resistance was monitored. Then again laser light was turned off for 5 min to continue measuring the resistance as a function of time.

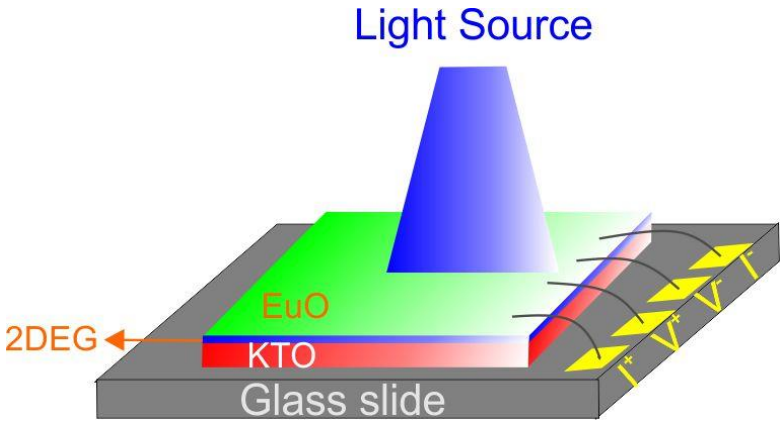

Figure 4.5: Schematic of the sample on a glass slide with light illumination. The Linear four probe method is used to measure the resistance.

The photo-response behavior of both the samples at room temperature (300 K) and low temperature (76 K) was studied with different wavelengths of light as shown in **Fig. 4.6**. In **Figure 4.6(a),** initially, the sample was in dark for 1 minute at 300 K, then the laser light of wavelength 405 nm with a power intensity of 0.5 mW was irradiated on the sample. Then the behavior of the resistance change was observed for 5 minutes in this mode. After 5 minutes of excitation, the laser light was turned off for the next 5 min and its growth behavior was observed. The same process was repeated for the next 10 minutes also. As you can see that after the removal of light, the system does not retain its original state, or some persistent remains in the conductance. This PPC has a lot of applications in designing optoelectronic devices as discussed in starting of the chapter. Percentage change in resistance (ΔR) is found to be more in the sample with lower carrier density (S8).

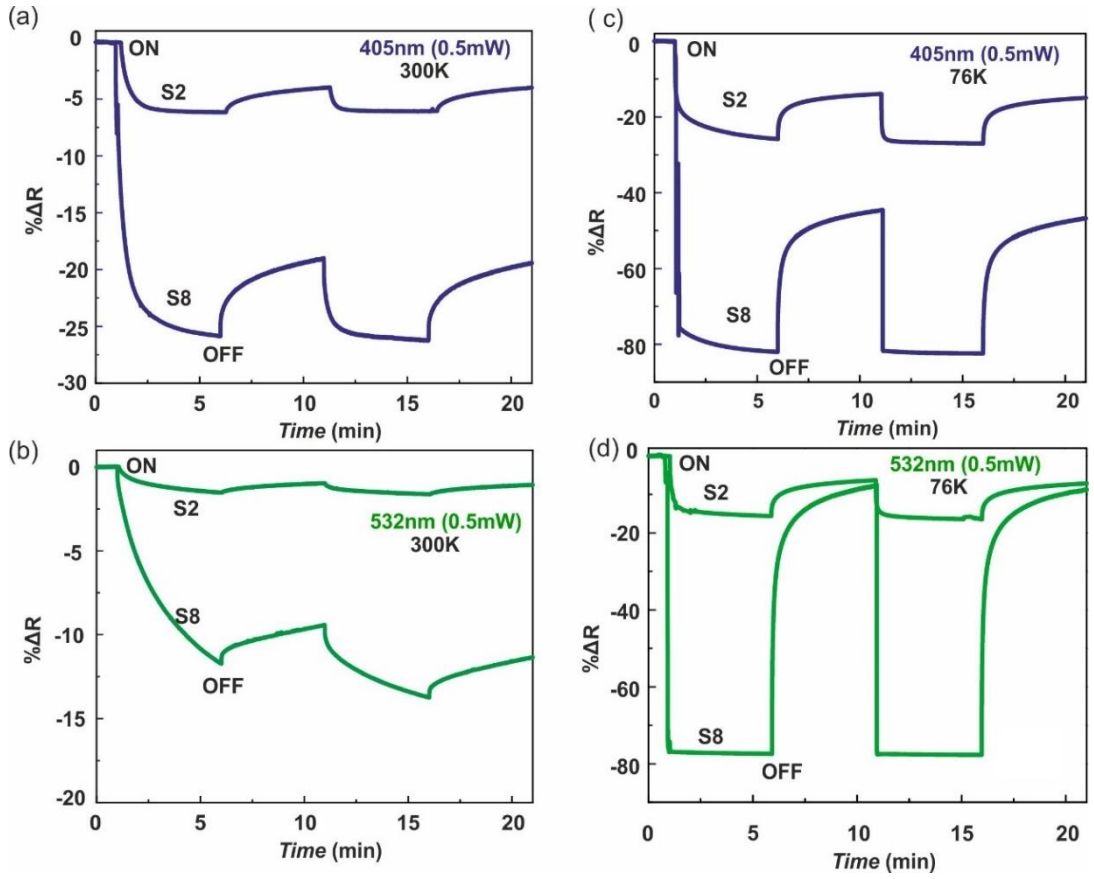

Figure 4.6: Percentage change in resistance as a function of time at 300 K for the light of wavelength (a) 405 nm (blue) and (b) 532 nm (green) for both samples (S2 and S8). Percentage change in resistance as a function of time at 76 K for the light of wavelength (c) 405 nm (blue) and (d) 532 nm (green) for both samples (S2 and S8).

The percentage change in resistance was calculated using the formula:

$$\%\Delta R = \left[\frac{R(t)-R(0)}{R(0)} \times 100\right]$$

Here R(t) is the resistance of the sample at any time t during the measurement and R(0) is the resistance value when the sample was initially in the dark mode.

In **Figure 4.6(b),** a similar process is repeated for both samples at room temperature under the presence of green light of wavelength 532 nm with the same power intensity. Here you can see that the percentage change in resistance is decreased for both samples in comparison to the blue light. **Figures 4.6(c)** and **(d)** shows the photo-response behavior at a lower temperature (76 K). Here, it is observed that a faster and larger magnitude response takes place for both samples in comparison to the room temperature. A clear signature of PPC is observed for both the sample at 76 K and 300 K and it decreases with an increase in the carrier density. The maximum change in resistance was found to be nearly 82% in the case of a sample with low carrier density with the illumination of blue light.

It is important to note that even a very low power such as 0.5 mW can produce significant photoconductivity, which might have important technological applications. For blue light (405 nm), a larger percentage of PC and PPC are observed compared to green light (532 nm). This could be because blue light has energy (3.06 eV) approximately similar to the KTO (~3.5 eV) band gap and larger than the band gap of EuO (~1.1 eV), the electron from both the valence band edge state of the KTO as well as from the valence band of EuO is excited.

In the next **Figure 4.7**, we have shown the photoconductivity and persistent photoconductivity change with the illumination of increasing power intensity of light. As power intensity is increased, more electron-hole pair generation takes place and hence conductivity is increased. In **Figure 4.7(a)**, the percentage change in photoconductivity is increasing with the excitation of the increasing power density of light for both the samples S2 and S8 at 300 K. This study is shown for blue light (405 nm) only. **Figure 4.7(b)** shows the change in persistent photoconductivity for the sample with lower carrier density found to be nearly 20% at 300 K. From **Figures 4.7(c) and (d),** we observe that the maximum PC and PPC are found to be nearly 82% and 50% respectively for the sample with lower carrier density at 76 K.

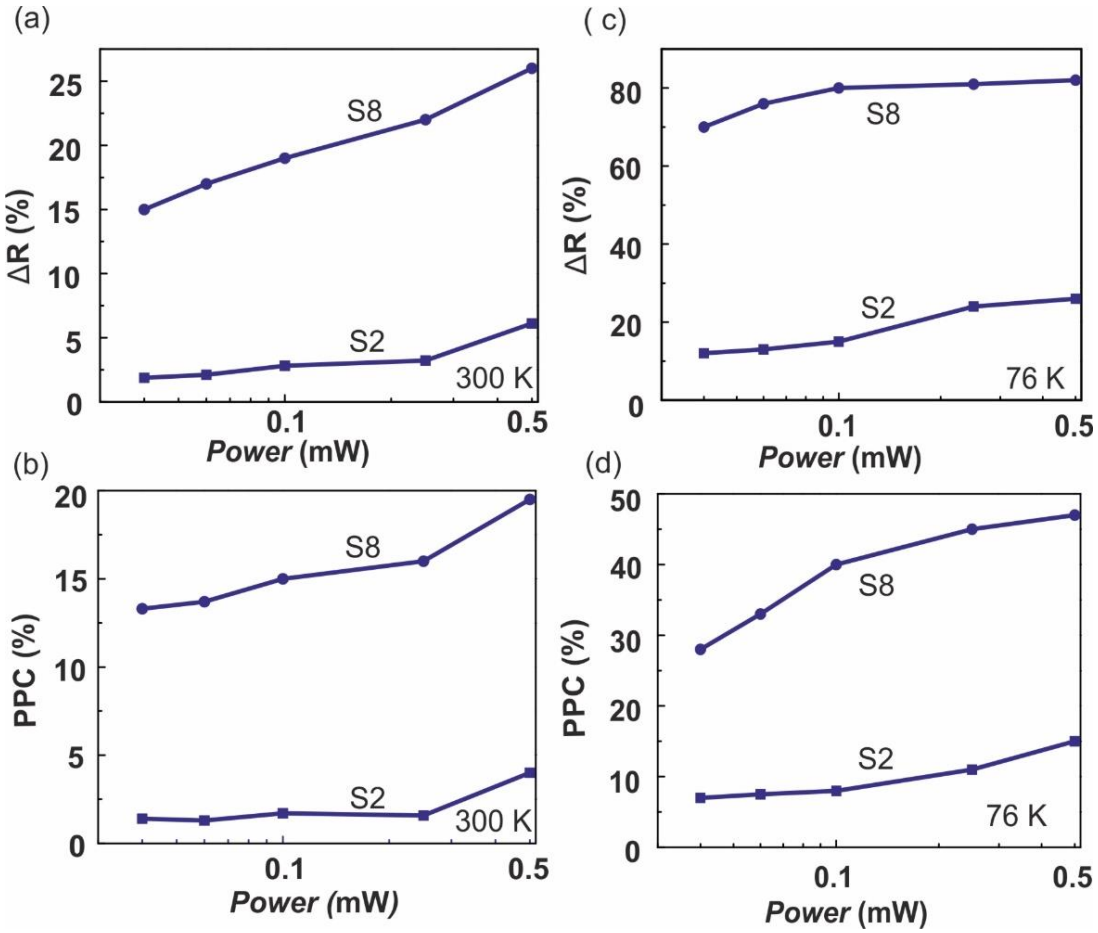

Figure 4.7: (a) PC and (b) PPC change with power intensity for both samples at room temperature. (c) PC and (d) PPC change with power intensity for both samples at 76 K.

Further, to get a more detailed description of the photo-response, it is essential to study the dynamic behavior of the signals at low and high temperatures. Here, we have studied the response behavior of sample S8 exhibiting higher PC and PPC under 405 and 532 nm light at a power of 0.1 mW. The plots of normalized percentage change in resistance with time are shown in **Fig. 4.8(a)** and **Fig. 4.8(b)** at 300 K. Here, we have fitted the data for 5 min response with two different components using the double exponential equation as given:

$$\Delta R_N = A \exp(-t/\tau_1) + B \exp(-t/\tau_2)$$

$$\Delta R_N = R_1(\tau_1) + R_2(\tau_2)$$

Here, the photo-response behavior is followed by two different processes: one is the fast process and another is the slow response.

Where $R_1(\tau_1)$ is the fast component, A and τ_1 are the relative weight and response time for this component and $R_2(\tau_2)$ is the slow component, B and τ_2 are the relative weight and response time for the slow component. The fitted data is shown by the black solid line at all temperatures and wavelengths. The different colors in the figure show the fast and slow components.

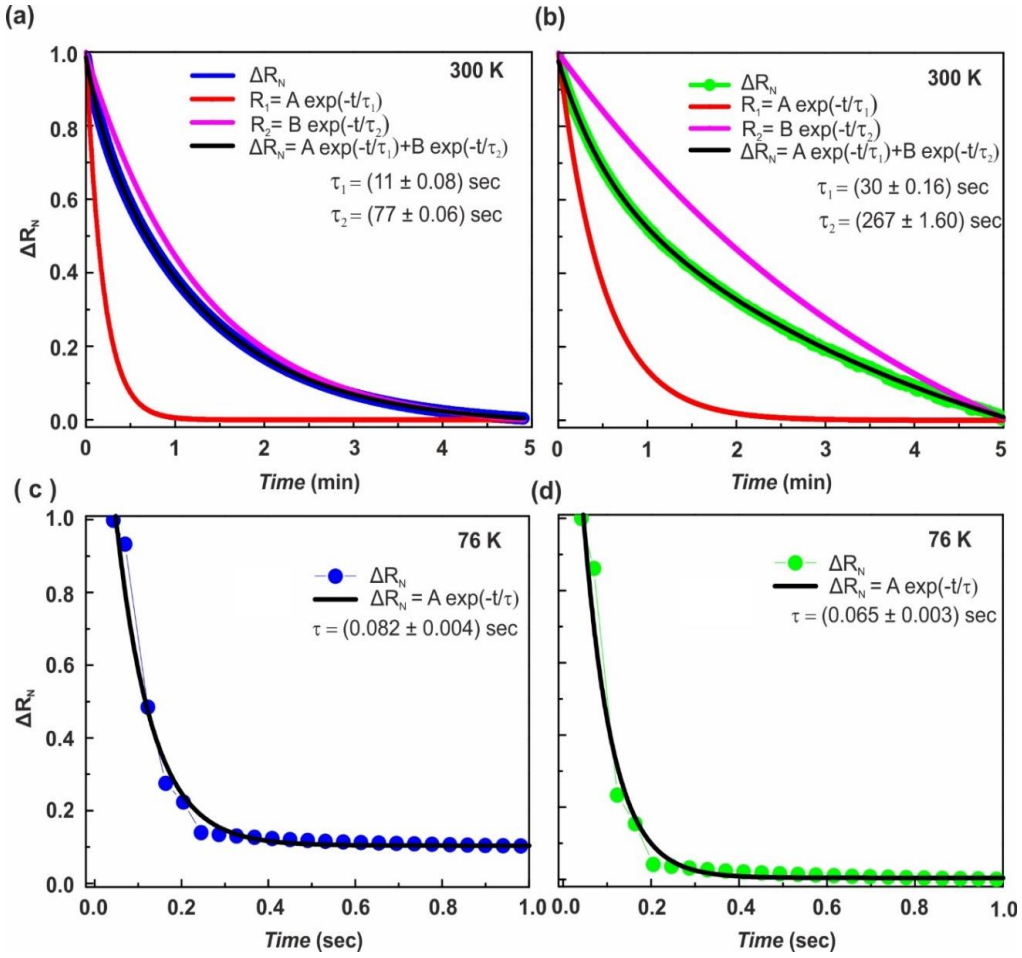

Figure 4.8: Normalized percentage change in resistance with time under the illumination of (a) 405 nm and (b) 532 nm wavelength light having power intensity of 0.1 mW at 300 K respectively. Normalized percentage change in resistance with time under the illumination of (c) 405 nm and (d) 532 nm wavelength light having power intensity of 0.1 mW at 76 K respectively.

In comparison to this, the response behavior in **Fig. 4.8(c)** and **Fig. 4.8(d)** at 76 K was well defined by a single exponential decay function (for both wavelengths of light) with the equation.

$$\Delta R_N = A \exp(-t/\tau)$$

Where τ comes out to be (0.082 ± 0.004) sec and (0.065 ± 0.003) sec for blue and green light respectively. This suggests that at low temperatures (76 K), single exponential behavior is followed by the photo response under both types of light illumination. In addition, it is surprising to note that the response rate at low temperature is at least two-order of magnitude faster than that at room temperature. The two slow relaxation times at room temperature suggest that these two processes suppress the intrinsic fast response of the system. The detailed understanding of the dynamics and photogenerated carrier is still unclear. This is important to mention that the relaxation time is much larger than what is expected from the usual electron-phonon mechanism [57-60]. To achieve a detailed understanding of the processes and this unusually longer relaxation time, further theoretical and experimental studies are needed. On the other hand, at low temperatures, the effect of phonons is negligible and a fast and large PC has been observed.

In one of the studies of the EuO-KTO interface by S. Goyal et al., where they had already presented the photo-dynamics of this sample of carrier density 8.5 x 10^{13} cm^{-2} [56]. In our study, we have presented the photo-dynamics of samples with carrier density (1.5 ± 0.016) x 10^{13} cm^{-2} and (1.4 ± 0.012) x 10^{14} cm^{-2}. The photo dynamics of this large range of carrier density give us a fair idea about the effect of light on the carrier density of a material.

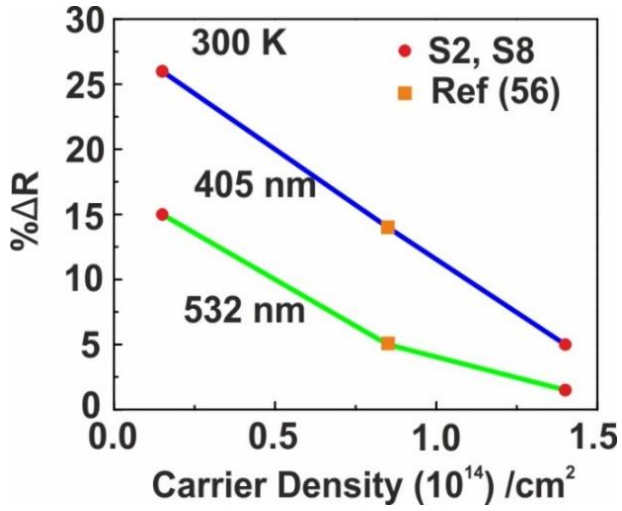

Figure 4.9: Percentage Resistance change with carrier density at 0.5 mW laser power for both blue and green light at 300 K comparing the three samples (S2, S8, and sample from reference 56).

Percentage resistance change vs carrier density plot (**Fig.4.9**) at room temperature indicates that with the increase in carrier density, change in photo resistance decreases, and hence, the effect of light decreases. corresponding to laser power P. α is the exponent, when α =1, the effect is purely photoconductive but for α >1 or <1, the response is not purely photoconductive. Here in this report of EuO-KTO, we have taken data only for lower laser intensity, and for this we have observed the linear behavior of photoresponse with laser power at room temperature. So, the process is dominated by the photoconductive effect only at room temperature. But at lower temperature value, α is less than one and hence dominated by the photovoltaic effect. It is worth mentioning that the actual process could be far more complex. Also, the sizable persistence is coming from the defects and impurities present in the system. This phenomenon finds application in storage devices.

4.4 Conclusion

In conclusion, we have found that conducting interface of EuO-KTO shows a large PC, the lower the carrier density higher the effect is. The room temperature PC response data is fitted using a double exponential function with a rather large response time. This suggests the presence of two types of photodynamic processes at the interface. The significantly faster and larger responses at lower temperatures suggest that phonon dynamics play an important role in PC. It is also observed that the photo-response and carrier density change with the deviation in the growth parameters of the sample. Our results give an important clue to design future-generation solar cells and holographic storage media.

Bibliography

[1]. A. Ohtomo and H.Y. Hwang, *Nature* **427**, 423 (2004).

[2]. S. Thiel, G. Hammerl, A. Schmehl, C.W. Schneider and J. Mannhart, *Science*, **313**, 5795 (2006).

[3]. J. Mannhart, and D.G. Schlom, *Science*, **327**, 5973 (2010).

[4]. H.Y. Hwang, Y. Iwasa, M. Kawasaki, B. Keimer, N. Nagaosa and Y. Tokura, *Nat. Mater*., **11**, 2 (2012).

[5]. B. Förg, C. Richter and J. Mannhart, *Appl. Phys. Lett.*, **100**, 5 (2012).

[6]. N. Reyren, S. Thiel, A.D. Caviglia, L.F. Kourkoutis, G. Hammerl, C. Richter, C.W. Schneider, T. Kopp, A.S. Rüetschi, D. Jaccard, M. Gabay, D. A. Muller, J.M. Triscone and J. Mannhart, *Science*, **317**, 5842 (2007).

[7]. A.D. Caviglia, S. Gariglio, N. Reyren, D. Jaccard, T. Schneider, M. Gabay, S. Thiel, G. Hammerl. J. Mannhart and J.M. Triscone, *Nature*, **456**, 7222 (2008).

[8]. A.D. Caviglia, M. Gabay, S. Gariglio, N. Reyren, C. Cancellieri and J.M. Triscone, *Phys. Rev. Lett.*, **104**, 126803 (2010).

[9]. A.D. Caviglia, S. Gariglio, C. Cancellieri, B. Sacépé, A. Fete, N. Reyren, M. Gabay, J.F. Morpurgo and J.M. Triscone, *Phys. Rev. Lett.*, **105**, 236802 (2010).

[10]. Y.Z. Chen, J.L. Zhao, J.R. Sun, N. Pryds and B.G. Shen, *Appl. Phys. Lett.*, **97**, 123102 (2010).

[11]. J.A. Bert, B. Kalisky, C. Bell, M. Kim, Y. Hikita, H.Y. Hwang and K.A. Moler, *Nat. Phys.*, **7**, 767−771 (2011).

[12]. Y. Lei, Y. Li, Y.Z. Chen, Y.W. Xie, Y. S. Chen, S.H. Wang, J. Wang, B.G. Shen, N. Pryds, H.Y. Hwang and J. R. Sun, *Nat. Commun.*, **5**, 5554 (2014).

[13]. Y. Xie, Y. Hikita, C. Bell and H.Y. Hwang, *Nat. Commun.*, **2**, 494 (2011).

[14]. Y. Hotta, T. Susaki and H.Y. Hwang, *Phys. Rev. Lett.*, **99**, 236805 (2007).

[15]. R. Tomar, R.M. Varma, N. Kumar, D.D. Sarma, D. Maryenko and S. Chakraverty, *Adv. Mater. Interfaces*, **7**, 1900941− 1900946 (2020).

[16]. S. Goyal, A. Singh, R. Tomar, C. Bera and S. Chakraverty, *AIP Conf. Proc*., 030275 (2019).

[17]. E.N. Jin, L. Kornblum, D.P. Kumah, K. Zou, C.C. Broadbridge, J.H. Ngai, C.H. Ahn and F.J. Walker, *APL Mater.*, **2**, 116109 (2019).

[18]. P. Perna, D. Maccariello, M. Radovic, U. Scotti di Uccio, I. Pallecchi, M. Codda, D. Marré, C. Cantoni, J. Gazquez, M. Varela, S. J. Pennycook and F. M. Granozio, *Appl. Phys. Lett.*, **97**, 152111 (2010).

[19]. C. Li, Q. Xu, Z. Wen, S. Zhang, A. Li and D. Wu, *Appl. Phys. Lett.*, **103**, 201602 (2013).

[20]. R. Tomar, N. Wadehra, S. Kumar, A. Venkatesan, D.D. Sarma, D. Maryenko and S. Chakraverty. *J. Appl. Phys*., **126**, 0353031-0353037 (2019).

[21]. S. W. Bedell, A. Khakifirooz and D. K. Sadana, *MRS Bull.*, **39**, 131(2014).

[22]. Y. Cao, X. Liu, P. Shafer, S. Middey, D. Meyers, M. Kareev, Z. Zhong, J.W. Kim, P. J. Ryan, E. Arenholz and J. Chakhalian, *Npj Quantum Mater*., **1**, 16009 (2016).

[23]. H. Yan, Z. Zhang, S. Wang and K. Jin, *Chin. Phys. B*, **27**, 117804 (2018).

[24]. F. V. E. Hensling, D. J. Keeble, J. Zhu, S. Brose, C. Xu, F.Gunkel, S. Danylyuk, S. S. Nonnenmann, W. Egger, R.Dittmann, *Sci. Rep.*, **8**, 8846 (2018).

[25]. A. Tebano, E. Fabbri, D. Pergolesi, G. Balestrino and E. Traversa, *ACS Nano*, **6**, 2 (2012).

[26]. S. Goyal, A. Singh, R. Tomar, R. Kaur, C. Bera and S. Chakraverty, *Solid State Commun*., **316-317**, 113930 (2020).

[27]. T. Dixit, A. Tripathi, K.L. Ganapathi, M.S.R. Rao and V. Singh, *IEEE Photonics Technol. Lett.*, **32**, 6 (2020).

[28]. P.J. Snyder, P. Reddy, R. Kirste, D.R. LaJeunesse, R. Collazo and A. Ivanisevic, *ACS Omega*, **3**, 1 (2018).

[29]. F. K. Bruder, R. Hagen, T. Roelle, M.S. Weiser and T. Faecke, *Angew. Chem. Int. Ed.*,**50**, 20 (2011).

[30]. S.H. Song, J. M. Kim and B.S. Yoo, *Opt. Lett.*,**16**, 22 (1991).

[31]. Q. Wang, J. Yang, S. Braun, M. Fahlman and X. Liu, *Org. Electron.*, **100**, 106375 (2022).

[32]. E. Majda-Zdancewicz, M. Suproniuk, M. Pawłowski and M. Wierzbowski, *Opto-Electron. Rev*., **26**, 2 (2018).

[33]. L. Zhao, Z. Fan, S. Cheng, L. Hong,Y. Li, G. Tian, D. Chen, Z. Hou, M. Qin, M. Zeng, X. Lu, G. Zhou, X. Gao and Jun-Ming Liu, *Adv. Electron. Mater.* **6**, 2 (2020).

[34]. J. Bao, I. Shalish, Z. Su, R. Gurwitz, F. Capasso, X. Wang and Z. Ren, *Nanoscale Res. Lett*., **6**, 404 (2011).

[35]. K. Boer and U.W. Pohl, *Cham: Springer*, pp 1181–2050 (2018).

[36]. S. Bhattacharyya, K.S.R. Koteswara Rao, S.V. Subramanyam and D. Kanjilal, *Appl. Phys. Lett.*, **68**, 2079–81 (1996).

[37]. H.J. Queisser and D.E. Theodorou, *Phys. Rev. Lett*., **43**, 5 (1979).

[38]. J.Z. Li, J.Y. Lin, H.X.Y. Jiang, M. Asif Khan and Q. Chen, *J. Appl. Phys*., **82**, 3 (1997).

[39]. R. Calarco, M. Marso, T. Richter, A.I. Aykanat, R. Meijers, A.V.D. Hart, T. Stoica and H.Lüth, *Nano Lett*., **5**, 5 (2005).

[40]. P. Feng, I. Monch, S. Harazim, G. Huang, Y. Mei and O.G. Schmidt. *Nano Lett*., **9**, 10 (2009).

[41]. M. Huijben, A. Brinkman, G. Koster, G. Rijnders, H. Hilgenkamp and D. H. A. Blank, *Adv. Mater*., **21**,1665 (2009).

[42]. A. Rastogi, J. J. Pulikkotil and R. C. Budhani, *Phys. Rev. B*, **89**, 125127 (2014).

[43]. H. Yan, Z. Zhang, S. Wang, H. Zhang, C. Chen and K. Jin, *ACS Appl. Mater. Interfaces*, **9**, 39011 (2017).

[44]. Y. Xie, Y. Hikita, C. Bell and H. Y. Hwang, *Nat. Commun.*, **2**, 494 (2011).

[45]. D. C. Vaz, E. Lesne, A. Sander, H. Naganuma, E.Jacquet, J. Santamaria, A. Barthélémy and M. Bibes, *Adv.Mater*., **29**, 28 (2017).

[46]. K. A. Brown, S. He, D. J. Eichelsdoerfer, M. Huang, I.Levy, H. Lee, S. Ryu, P. Irvin, J. Mendez-Arroyo, C.-B.Eom, C. A. Mirkin and J. Levy, *Nat. Commun.*, **7**,10681 (2016).

[47]. N. Y. Chan, M. Zhao, N. Wang, K. Au, J. Wang, L. W. H.Chan and J. Dai, *ACS Nano*, **7**, 8673 (2013).

[48]. Y. Zhang, R.Tao, X. Zhao, Z. Sun, Y. Wang and L. Xu, *Chem. Commun.*, **52**, 16 (2016).

[49]. L. Zhang, X.Yang, W. Wang, G.G. Gurzadyan, J. Li, X. Li, J. An, Z. Yu, H. Wang, B. Cai, A. Hagfeldt and L. Sun, *ACS Energy Lett.*, **4,** 4 (2019).

[50]. P.C. Huang, W.C. Yang and M.W. Lee, *J. Phys. Chem. C***, 117**, 36 (2013).

[51]. R. Papadakis, I. Deligkiozi and H. Li, *Intech Open*, United Kingdom, **2018**.

[52]. J. Shi, Y. Xu, X. Wang, L. Zhang, J. Zhu, T. Pang and X. Bao, *Org. Biomol. Chem*., **13**, 27 (2015).

[53]. R.F. Khairoutdinov, L.V. Doubova, R.C. Haddon and L. Saraf, *J. Phys. Chem. B*, **108**, 52 (2004).

[54]. N. Wadehra, R. Tomar, R.M. Varma, R.K. Gopal, Y. Singh, S. Dattagupta and S. Chakraverty, *Nat. Commun*., **11**, 874 (2020).

[55]. N. Kumar, N. Wadehra, R. Tomar, S. Dattagupta, S. Kumar and S. Chakraverty, *Adv. Quantum Technol.*, **4**, 2000081 (2020).

[56]. S. Goyal, R. Tomar and S. Chakraverty, *ACS Appl. Electron. Mater.*, **3**, 2 (2021).

[57]. H. Yan, S.H. Wang, Z.T. Zhang, H.R. Zhang, C.L. Chen and K.X. Jin, *J. Appl. Phys.*, **124**, 035302 (2018).

[58]. E. Mikheev, B. Himmetoglu, A.P. Kajdos, P. Moetakef, T.A. Cain, C.G. Van de Walle and S. Stemmer, *Appl. Phys. Lett*., **106**, 6 (2015).

[59]. K.X. Jin, B.C. Luo, Y.F. Li, C.L. Chen, T. Wu, *J. Appl. Phys*.**, 114**, 3 (2013).

[60]. A. Rose. *Phys. Rev*., **97**, 1727 (1955).

Chapter 5

Light-enhanced gating effect at conducting EuO-KTO interface

5.1 Introduction

The two-dimensional electron gas (2DEG) at complex oxide interfaces has attracted great interest in recent years due to exceptional observed properties, such as 2D superconductivity, enhanced Rashba spin-orbit coupling, 2D magnetism, etc [1-3]. These properties can be tuned by electrostatic gating which leads to several interesting observations such as metal-to-insulator transition, tunable superconductivity, and unusual variation in the magneto-transport behavior [4-6]. So, it is possible to electrostatically modulate the complex oxide interfaces by applying an external electric field. This tuning pathway is of great interest and it is one of the operating principles of nearly all electronic devices. Gating can be done in several different ways such as top gating, back gating, ionic liquid gating, by the tip of a conducting atomic microscope (c-AFM), and so on [7-12]. Among all the gating geometries, back gating is a commonly used gating process, where the substrate (STO or $KTaO_3$ (KTO)) is used as a dielectric material. Both KTO and STO have high-dielectric constants. The back gate voltage applied across the typically 0.5 mm thick substrate ranges from 1 V to several hundred volts. . However, problems with top-gating frequently occur as a result of electrical breakdown caused by defects in the gate dielectric, which causes leakage currents to shunt the gate and interface electronic system.

For conventional semiconductor devices, the gate field takes effect through charging or discharging a capacitor formed by the conducting interface and gate electrode. But, for complex oxide 2DEG, the gating effect is much more complex. Apart from the charge transfer, many processes such as charge trapping/ de-trapping, migration of ionic defects, and ferroelectric instabilities could be involved, which may affect the gating effect. Light illumination and electrostatic gating field are two widely used stimuli for controlling electronic processes in low-dimension systems. In the previous reports [13-15], it has

been found that lattice deformation of STO and lattice polarization can be induced by the simultaneous application of light illumination and gate field, yielding a greatly enhanced gating effect on the LAO-STO interface. The maximum increase in the sheet resistance caused by the combined effect of light and gating was 200-fold larger than that produced by the gate field only. This work opened a wide space to explore the various emergent phenomena at complex oxide interfaces that may be helpful to design various optoelectronic and spintronic devices. However, several issues remain to be addressed. The foremost is, what will happen to this metallic interface or how the carrier dynamics change under the joint effect of light illumination and gate field. It was observed that for semiconducting LAO-STO, the decrease in photo-illuminated resistance played a vital role in enhancing the gating effect, especially at low temperatures [14]. They give confirmed evidence of occurance of lattice polarization by monitoring the discharging process after removal of gate field. This lattice polarization was responsible for the strong affect of this 2DEG. Another issue is related to the effects associated with the kinetic process of anion migration. As reported, the enhanced gating effect stemmed from the lattice polarization due to the electro-migration of oxygen vacancies [13]. They tried to explain the migration of oxygen vacanies under light and gate field with the help of theoretical modelling.

In this chapter, we present a systematic investigation of the joint effect of light illumination and gate bias on the metallic EuO-KTO interface. An unusual illumination-enhanced gating effect (3-order change in resistance) is observed for this metallic system at room temperature. This enormous change in conductance is observed even with visible light of very low power intensity of 0.5 mW along with the back gate. There are very few reports on STO-based heterostructures, where unusual enhancement in the resistance was observed with the combined effect of light and back gate [13,16]. In 2020, S. Goyal et al. tuned the conducting interface of $LaVO_3$-KTO in presence of both light and back gate and observed a maximum change in resistance of nearly 130 % [17]. Here, in our EuO- KTO system, the maximum enhancement in the resistance was observed to be nearly 1.0 x 10^5 %. So, this is the first study on KTO-based heterostructure with the large tuning of the conductivity (3-order change) using both light and back gate. This unusual effect offers a new perspective for tuning the

photoelectrical properties at the oxide interfaces, which may help design advanced photoelectric devices.

5.2 Experimental Method

The sample was prepared by depositing EuO layers (25unit cells in thickness), using the technique of pulsed laser (248 nm) ablation, on TaO_2 terminated (001) KTO substrate with a dimension of 2 x 2 x 0.5 mm^3. The deposition temperature was 400 °C and the oxygen partial pressure was $1x10^{-7}$ Torr. The fluence of the laser pulses was 4 J/cm^2 and the repetition rate was 2 Hz. After deposition. The sample was naturally cooled down to room temperature without changing oxygen pressure. Ultrasonic Al-wire bonding was adopted for electrical contacts. The applied current for the resistance measurement was 1.6 μA. The standard four-probe technique was employed for resistance measurements. The leakage current was less than 4 nm for all the measurements. For the gating effect study, a gate voltage was applied to the back side of the KTO substrate while the interface of EuO-KTO was grounded and the resistance was recorded by a multimeter (DMM 7510, Keithley) in the presence/absence of light illumination.

5.3 Results and discussion

Figure 5.1(a) represents the schematic of the EuO-KTO sample with light and back-gating configurations. **Figure 5.1(b)** and **(c)** shows the resistance change of the conducting interface upon illumination of the light and back gate respectively. Here, we have observed that with an increase in the energy of the illuminated light, the percentage change in resistance increases. A maximum change in resistance was observed to be nearly 40% in the case of blue light (405 nm) illumination. This response behavior was recorded for 5 minutes under light illumination and the same protocol was followed for all further studies. With the application of back gate voltage only, in **Fig. 5(c),** the sample response is shown, where a maximum change in resistance is observed to be nearly 20% upon applying a negative back gate voltage of -120 V. Here, we have observed that with the application of

back gate voltage only, two distinct processes take place: the sudden jump that is followed by a slow increase in the sample resistance [4,18]. As reported by previous investigations [13,16], the first process stems from the conventional capacitive effect that depletes the charge carriers of the 2DEG, and the following slow resistance growth is due to the electro-migration of the oxygen vacancies, which results in lattice polarization.

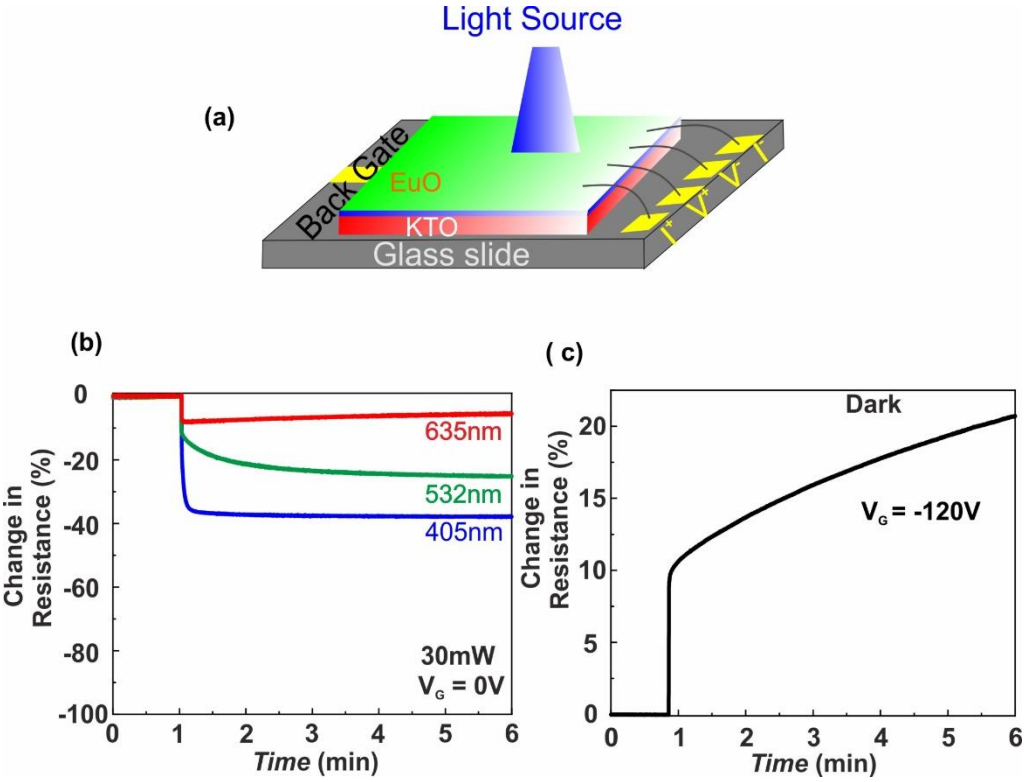

Figure 5.1: (a) Schematic of the EuO-KTO sample with the light illumination and back gating configurations. (b) Percentage change in resistance vs time is shown in presence of the light of different wavelengths of power intensity 30 mW without any back gate. (c) Percentage change in resistance with the application of back gate voltage only.

Further, if we shine the laser light (λ= 405 nm) of power 30 mW simultaneously with the negative gate field (V_G from -6 V to -120 V), then we see a giant change in the resistance of the interface is observed as shown in **Fig. 5.2(a).** The maximum change in resistance was found to be nearly 100000 % under application of 30 mW light in presence of -120 V of applied voltage. A possible explanation for this is that without illumination, the negative bias slightly polarizes the interface region of KTO yielding slow resistance growth, following the first sudden jump but when we illuminate the light it accelerates the interface polarization by enhancing the electromigration of oxygen vacancy. These two

effects reduce sample carrier density and hence amplify the gating effect. A similar unusual phenomenon was also observed in the past for the semiconducting LAO-STO interface [13]. The same study was also done with the positive back gate voltage and light illumination. Not much change in resistance was observed in comparison to that occurs under the application of light only and the maximum change in resistance was found to be nearly 45% as shown in **Fig. 5.2(b). Figure 5.2(c) and (d)** shows the original value of the resistance change on the application of light and back gate. The maximum resistance value changes from ~85 kΩ to above 100000 kΩ on application of light and negative electrostatic gate. While the resistance value decreases to a minimum value of nearly 47 kΩ on 5 minutes of application of light and positive electrostatic gate.

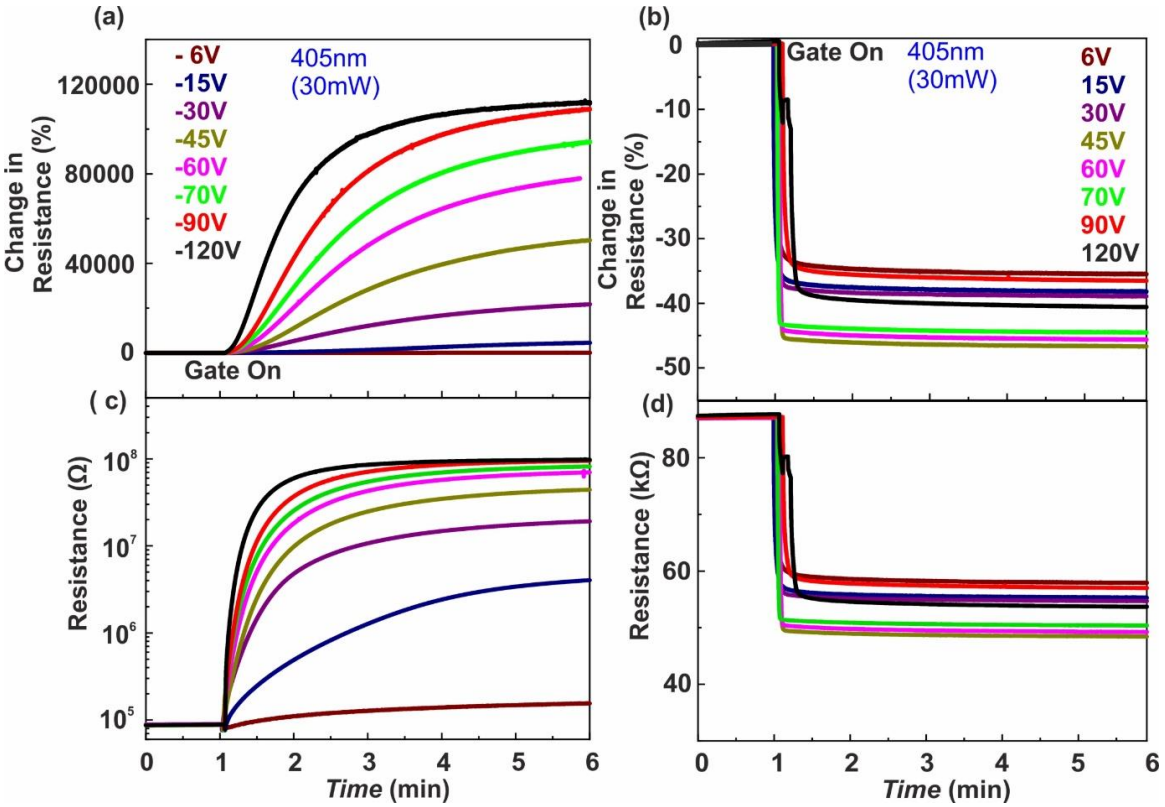

Figure 5.2: (a) Change in resistance with simultaneous application of light and negative back gate(varying) at a constant laser light (405 nm) of power intensity of 30 mW (b) Resistance change with joint effect of light (405 nm) and different positive back gate voltage. (c) resistance value changes from ~ 10^5 to above 10^8 with application of light and negative gate voltage. (d) the behaviour of resistance with positive gate voltages and constant power of light intensity.

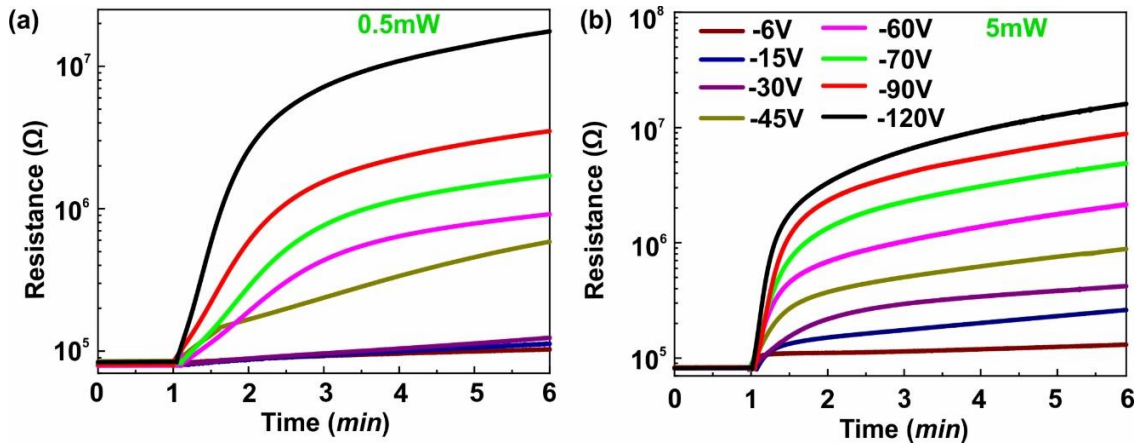

Figure 5.3:(a) and (b) shows the evolution of resistance with time after the simultaneous application of light and negative back gate voltage for green light (532 nm) at different power intensities of 0.5 and 5 mW respectively.

We have also performed the same measurement with the green and red light laser with different power intensities. Resistance behaviour of the samples is shown with green laser light (532 nm) in **Fig. 5.3.** Here, in all the experiments, initially, the sample was kept in dark for nearly 1 minute and then the resistance behavior was monitored for 5 minutes upon simultaneous application of light and back gate voltage as shown in **Fig. 5.3(a) and (b)**. It was observed that with the increase in power intensities of light, the resistance increases much faster initially just after the illumination of light and back gate.

In **Figure 5.4 (a),** we have shown the resistance of the sample that was recorded for the 5 minutes of application of both the blue light (405 nm) and different negative back gate voltages. Here, you can see that there is a sudden huge jump in the resistance value and it goes from 10^5 to above 10^8 Ω. After 5 minutes, if we switch off both the external stimuli, then this higher resistance state remains in the system which can be bring down to its original state within seconds by applying a laser light only. **Figure 5.4(b) and (c)** shows the behaviour of the resistance with green (532 nm) and red laser (635 nm) light along with different voltages, while keeping the power intensity constant respectively. **In Figure 5.4 (d),** normalized resistance vs negative back gate voltage behavior is shown, where in comparison to the dark, the maximum change was

observed to be above 3 orders for blue light of 30 mW and the negative back gate voltage of -120 V.

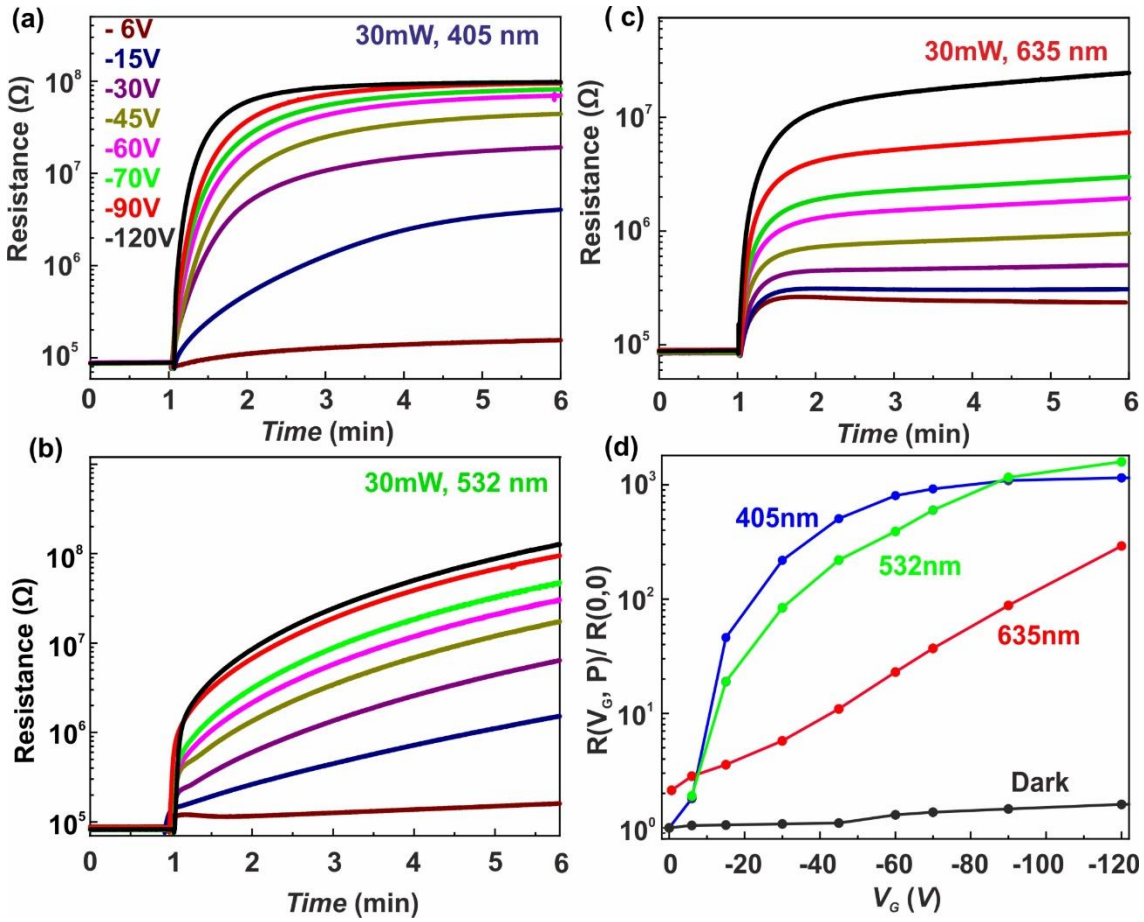

Figure 5.4: (a), (b) and (c) are the resistance vs time plot in presence of both light and different negative back gate voltages at constant power of different lights of wavelengths 405, 532 and 635 nm respectively. (d) Normalized resistance vs back gate voltage curve for laser light of different wavelengths at a constant power supply of 30 mW recorded after 5 minutes of application of light and back gate.

Here, a light of power intensity 30 mW, pushes the sheet resistance ratio R (V_G, P)/ R (0, 0) from 1 to ~ 1150 and hence amplifying the gating effect. Here R (V_G, P) and R (0, 0) represents the resistance recorded after 5 minutes of application of back gate voltage and light illumination at power intensity of 30 mW, and resistance of the sample initially when it was unperturbed by any light and back gate voltage respectively. Here, even a

back gate voltage as low as -15 V can cause a resistance growth of 48-fold as shown in **Fig. 5.4(d).**

In LAO-STO case, the oxygen vacancy concentration at the interface is high due to the outward oxygen in diffusion from the STO substrate during the deposition of the LAO layers and the resulted electron doping leads to the 2DEG at the a-LAO/STO and might also contribute to the conduction of the c-LAO/STO interface. Without illumination, negative bias only slightly polarizes the interface region of STO, yielding the slow R_S growth following the first sudden jump. Light illumination accelerates interface polarization by enhancing the electromigration of oxygen vacancies, probability by exciting the trapped electrons in deep oxygen vacancy states. This polarization yields an extra tuning to carrier density and weakening of the interfacial confining well of 2DEG. These two effects reduce carrier density and enhance the gating effect. But in EuO-KTO, the growth condition is different from the LAO-STO case. Here, the sample is grown at 400° C and oxygen partial pressure of 10^{-7}. Here, the reason for the interfacial conductivity is either oxygen vacancy or substitution of Eu with K site ions. Here also, it is assumed that this large tuning of conductivity may be due to the electromigration of the oxygen vacancies. The exact reason is still not clear to understand this illumination effect, we further examined the carrier density of the sample by Hall measurement for both under dark as well as under light illuminations.

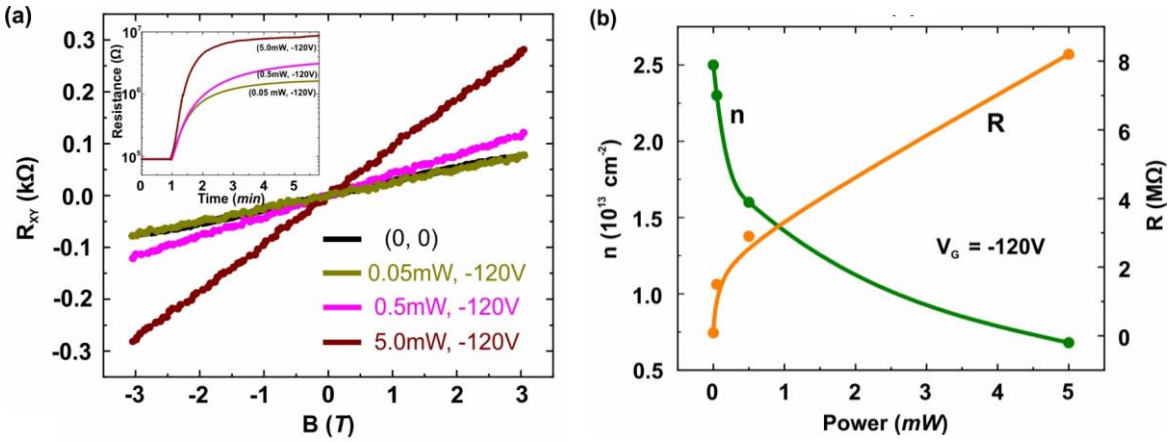

Figure 5.5: (a) Hall measurement after application of light and back gate. In the inset, we have shown the saturated resistance after 5 minutes of light illumination and back gate voltage. (b) Carrier density (left axis) and resistance (right axis) of the sample with different power intensity of light at a constant back gate voltage of -120 V.

From the linear R_{XY} vs B relation as shown in **Fig. 5.5 (a),** we deduce the initial carrier density and change in carrier density after the simultaneous application of light and back gate. Here R_{XY} is the Hall resistance measured with the magnetic field (B). In the inset, the saturated resistance value is shown after the 5 minutes of application of light and back gate voltage. It is observed that with the increase in power intensity of light from 0.05 to 5 mW at a constant negative back gate voltage of -120 V, the slope of the Hall resistance changes, which confirms the change in carrier density. In light of power intensity 5 mW and the gate voltage of -120 V, the intrinsic carrier density reduces from 2.5 x 10^{13} cm^{-2} (initial value without any light and back gate) to 6.8 x 10^{12} cm^{-2} as shown in **Fig.5.5(b)**. It is worth noting that the change in carrier density observed from Hall under light illumination and back gate is at least one order of magnitude lower than the samples original carrier density. This suggests that the actual process of increase in resistance under the simultaneous application of light and gate is far more complicated.

In **Figure 5.5 (b),** the vertical left axis shows the carrier density and the right axis shows the resistance value with an increasing power intensity of light at a constant negative back gate voltage of -120 V. Here, the carrier density decreases with the illumination of light of increasing power intensity and the resistance increases with the increase in power intensity. However, illumination enhancement is almost absent, when the interface is positively gated.

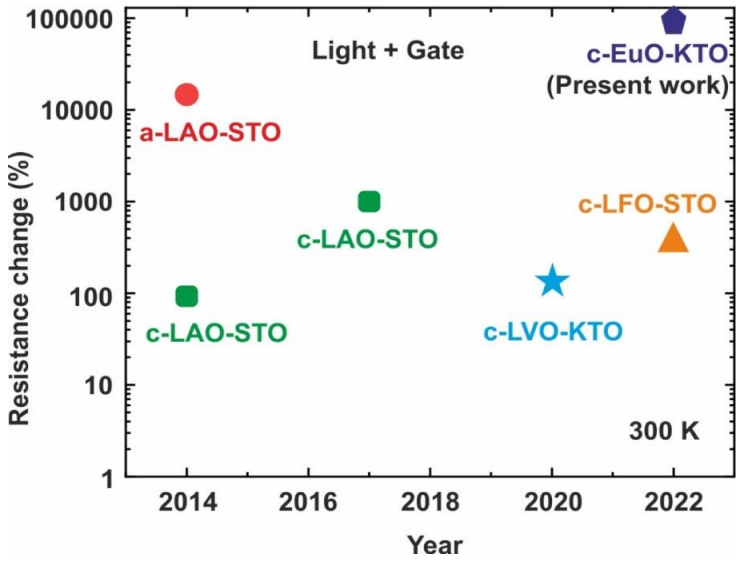

Figure 5.6: Percentage change in resistance with joint effect of light and back gate voltage for different samples reported.

Figure 5.6 shows the comparison of our data with the different reported work with application of both light and gate on crystalline and amorphous samples of different oxide materials. As you can see that, till now the maximum tuning of the resistance is observed in our c-EuO-KTO system. There is very unusual change in the resistance (100000 %) compared to the previous studies [14,16,17].

In addition to the resistance change under the application of light or gate, the signature of persistence current has also been observed. In **Figure 5.7(a),** we have shown that after the withdrawal of light illumination (405 nm, 532 nm), the system does not retain its original state. It means there is always some persistent remains in the system. **Figure 5.7(b)** shows that some persistent current remains even after 25 hours**.** Here, we have shown this persistence only for blue light (405 nm). Nearly 3.5% persistent photoconductivity (PPC) was recorded after 25 hours of removal of light.

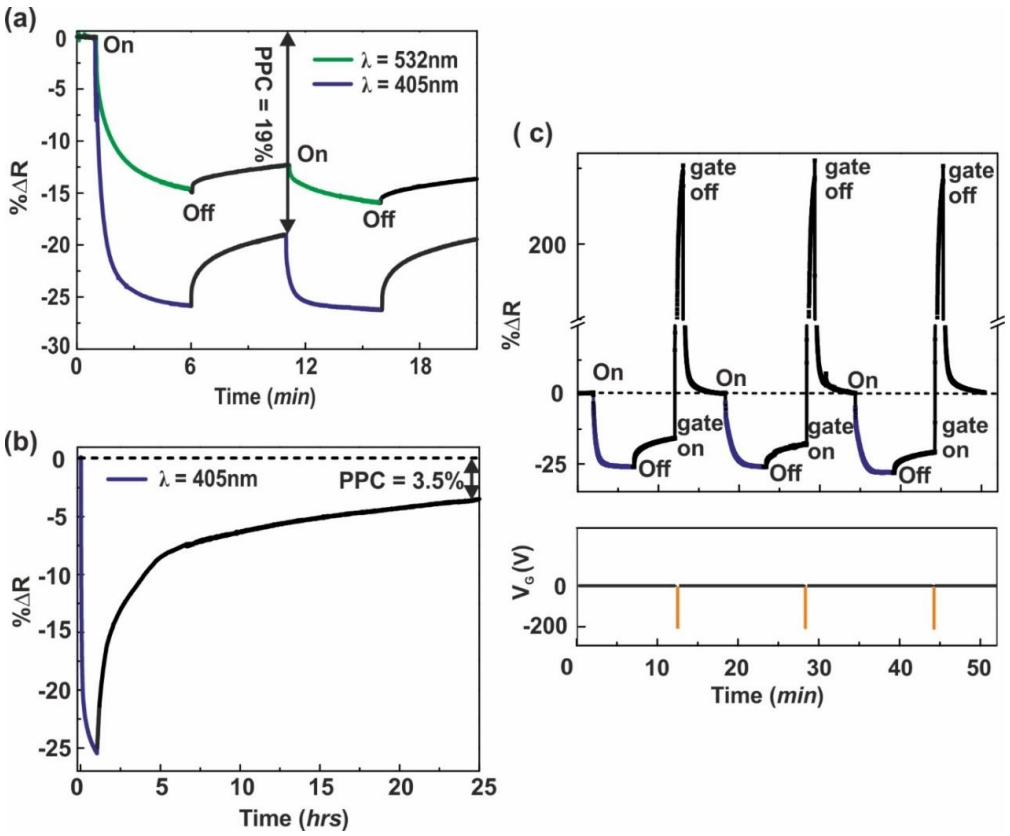

Figure 5.7: (a) Percentage change in resistance with time with different wavelengths of light showing the PPC effect. (b) Percentage change in resistance with time showing 3.5% PPC after 25 hours of removal of blue light. (c) Percentage change in sheet resistance with time under sequential application of 405 nm light and back gate -200 V.

Due to the presence of the PPC, this system might be used as a volatile memory. In **Figure 5.7 (c),** we have proposed and implemented some protocols to write and erase such memory**.** The protocol: application and then removal of light sent to a lower resistive state which persists, then an application of negative voltage erases that memory, bringing back to the initial resistance state. The lower panel shows the protocol used to get the data of the above panel.

First, the sample is illuminated with light (405 nm) of power intensity 5 mW for 5 minutes, then the light is removed and the system remained in its lower resistance state (ON state). A negative gate pulse of -200 V (turned on and off within 1 min) brings this lower state to its original resistance state (OFF state). We have repeated this process 3 times. For light of wavelength 405 nm, the system retains its original state with negative pulse of -200 V, but for light of wavelength 532 nm, a negative pulse of -80 V can bring the system to its original state as shown in **Fig. 5.8.**

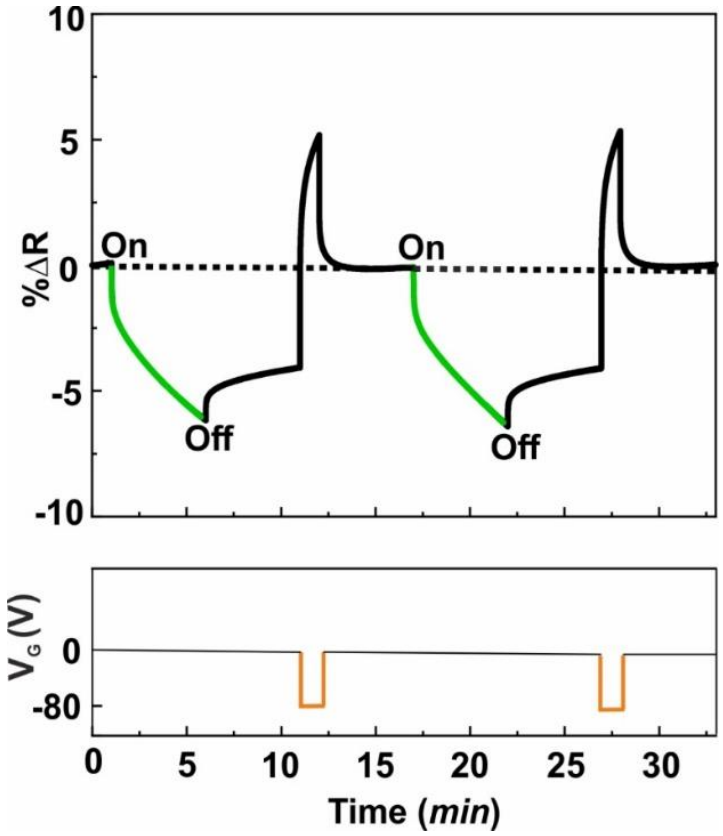

Figure 5.8: Percentage change in sheet resistance with time under sequential application of 532 nm light and back gate voltage of -80 V.

5.4 Conclusion

A systematic investigation of the joint effect of the light and gate bias on the metallic EuO-KTO interface is performed. An unusual enhancement of the gating effect by light illumination is observed. This enhancement is due to the migration of oxygen vacancies under an electrical field and light illumination, which leads to the depletion of the carrier density at the interface. We have seen the PPC effect at this interface. We have also demonstrated that by applying light and back gate in an appropriate sequence, this system can be used in memory device applications. Detailed theoretical modelling is needed to understand the behavior of charge dynamics under the effect of light, back gate voltage and joint effect of light and back gate voltage at this interface. This work deepens the understanding of photoexcitation enhanced gating effect at EuO-KTO interface. The principle proven here could also be extended to other complex oxide interfaces.

Bibliography

[1]. N. Reyren, S. Thiel, A. D. Caviglia, L. F. Kourkoutis, G. Hammerl, C. Richter, C. W. Schneider, T. Kopp, A. S. R€uetschi, D. Jaccard, M. Gabay, D. A. Muller, J. M. Triscone and J. Mannhart, *Science*, **317**, 1196 (2007).

[2]. A. D. Caviglia, M. Gabay, S. Gariglio, N. Reyren, C. Cancellieri, and J. M. Triscone, *Phys. Rev. Lett.* **104**, 126803 (2010).

[3]. A. Brinkman, M. Huijben, M. van Zalk, J. Huijben, U. Zeitler, J. C. Maan, W. G. van der Wiel, G. Rijnders, D. H. A. Blank and H. Hilgenkamp, *Nat. Mater*. **6**, 493 (2007).

[4]. S. Thiel, G. Hammerl, A. Schmehl, C. W. Schneider and J. Mannhart, *Science* **313**, 1942 (2006).

[5]. C. Bell, S. Harashima, Y. Kozuka, M. Kim, B. G. Kim, Y. Hikita and H. Y. Hwang, *Phys. Rev. Lett.* **103**, 226802 (2009).

[6]. M. Diez, A. Monteiro, G. Mattoni, E. Cobanera, T. Hyart, E. Mulazimoglu, N. Bovenzi, C. W. J. Beenakker and A. D. Caviglia, *Phys. Rev. Lett.* **115**, 016803 (2015).

[7]. S. Wang, Y. Bai, L. Xie, C. Li, J. D. Key, D. Wu, P. Wang and X. Pan, *ACS Appl. Mater. Interfaces* **10**, 1374 (2018).

[8]. S.-I. Kim, D.-H. Kim, Y. Kim, S. Y. Moon, M.-G. Kang, J. K. Choi, H. W. Jang, S. K. Kim, J.-W. Choi, S.-J. Yoon, H. J. Chang, C.-Y. Kang, S. Lee, S.-H. Hong, J.-S. Kim and S.-H. Baek, *Adv. Mater*. **25**, 4612 (2013).

[9]. V. T. Tra, J.-W. Chen, P.-C. Huang, B.-C. Huang, Y. Cao, C.-H. Yeh, H.-J. Liu, E. A. Eliseev, A. N. Morozovska, J.-Y. Lin, Y.-C. Chen, M.-W. Chu, P.-W. Chiu, Y.-P. Chiu, L.-Q. Chen, C.-L. Wu and Y.-H. Chu, *Adv. Mater.* **25**, 3357 (2013).

[10]. S. Zeng, W. Lü, Z. Huang, Z. Liu, K. Han, K. Gopinadhan, C. Li, R. Guo, W. Zhou, H. H. Ma, L. Jian, T. Venkatesan and Ariando, *ACS Nano* **10**, 4532 (2016).

[11]. C. Cen, S. Thiel, G. Hammerl, C. W. Schneider, K. E. Andersen, C. S. Hellberg, J. Mannhart and J. Levy, *Nat. Mater.* **7**, 298 (2008).

[12]. C. Cen, S. Thiel, J. Mannhart and J. Levy, *Science* **323**, 1026 (2009).

[13]. Y. Lei, Y. Li, Y. Z. Chen, Y. W. Xie, Y. S. Chen, S. H. Wang, J. Wang, B. G. Shen, N. Pryds, H. Y. Hwang and J. R. Sun, *Nat. Commun.* **5**, 5554 (2014).

[14]. Y. Li, H. R. Zhang, Y. Lei, Y. Z. Chen, N. Pryds, B. G. Shen and J. R. Sun, *Sci. Rep.* **6,** 22418 (2016).

[15]. Y. Li, Y. Lei, B. G. Shen and J. R. Sun, Sci. Rep. **5**, 14576 (2015).

[16]. Z. Yang, Y. Chen, H. Zhang, H. Huang, S. Wang, S. Wang, B. Shen and J. Sun, Appl. Phys. Lett. **111**, 231602 (2017).

[17]. S. Goyal, N. Wadehra and S. Chakraverty, Adv. Mater. Interfaces **7**, 2000646 (2020).

[18]. D. V. Christensen, F. Trier, Y.Z. Chen, A. Smith, J. Nygard and N. Pryds, Appl. Phys. Lett. **102**, 021602 (2013).

Chapter 6

High-field magneto-transport in a spin-polarized quasi-two-dimensional electron gas at EuO-$KTaO_3$ interface

6.1 Introduction

Oxide heterojunctions provide excellent platforms for investigating a wide range of emergent phenomena. Because of its numerous intriguing characteristics and potential applications in new-generation semiconductor and spintronic devices, the two-dimensional electron gas (2DEG) formed at the interfaces between two insulating transition metal oxides has triggered significant attention in the past decade [1-4]. The 2DEG at the perovskite oxide interface was first discovered for $LaAlO_3$-$SrTiO_3$ (LAO-STO) [5]. Previous research has shown that the conductive interfaces in the STO-based heterojunctions exhibit an unexpectedly richer cascade of peculiar features, such as the coexistence of ferromagnetism and superconductivity, and pseudogap-like behavior [6,7]. Numerous attempts have been made by replacing STO with other perovskite oxides in order to better understand how the Ti-ions contribute to emergent phenomena and to generate 2DEG with higher mobility [8,9]. In the last few years, the 2DEG of even stronger spin-orbit coupling and higher mobility with electrons originating from the Ta 5d orbitals has been discovered at a few perovskite oxide interfaces based on $KTaO_3$ (KTO) [10-12]. The KTaO3 is a band insulator with bandgap ~ 3.6 eV and also a polar perovskite oxide. Furthermore, it has been discovered that the KTO surface and KTO-based interfaces with large carrier densities exhibit 2D-superconductivity with a higher critical temperature in comparison to STO-based interfaces or surfaces [13-15]. KTO is a 5d transition metal oxide that exhibits a lighter effective mass of electrons and a stronger spin-orbit coupling (SOC) at its conducting surface/interface than STO-based interfaces. As a result of strong SOC, the low-lying Ta:t_{2g} band splits at the Γ point and forms the light and heavy bands having the mixed character of d_{xy}, d_{xz}, and d_{yz} orbitals [16-18]. KTO-based 2DEG is comparable to the STO-2DEG from the standpoint of electronic band structure, where electrons primarily occupy t_{2g} orbitals of transition metal ions. Recent density functional theory calculations, spectroscopy measurements, and

Shubnikov-de Haas oscillations (SdH) study confirms the lighter effective mass of KTO-2DEG (~ 0.3-0.6 m_e) formed at the interface of EuO and KTO compared to STO based 2DEG (~ 0.6-1.8 m_e) [19-21].

EuO is a highly spin-polarized ferromagnetic semiconductor that has been examined as a potential candidate for spintronics and optoelectronic devices. Below the curie temperature (69 K), it shows ferromagnetic nature [22], but at room temperature, stoichiometric EuO behaves like a paramagnetic semiconductor with a band gap of 1.2 eV [23,24]. EuO has been known due to its prominent response to Faraday and magneto-optic Kerr effects [25,26]. Recently, doped EuO has been deposited on Si and GaN, which can be used in spintronics [27]. The enrichment of Eu in EuO can convert it into half metal that can be used as a spin injector. EuO is an interesting candidate to study the quantum phenomenon of conducting interface of EuO-KTO.

The quantum oscillations are observed at high magnetic field and low temperature in magneto-transport measurements. So, why these quantum oscillations occurs ?. The electrons in the bulk regions of a 2DEG move in a circular motion when a magnetic field is applied to it. The electrons in the samples border areas are unable to move in complete circles because they are reflected back from the interface. These scattering incidents increase the energy of the electrons. The current flows without resistance in the edge channels because the magnetic force pushes electrons to move in forward direction. The eigen values of these circularly moved electrons are the same as of a harmonic oscillator with cyclotron frequency w_c, $w_c = \frac{qB}{m^*}$, here m^* is the effective mass of electrons parallel to circular motion. Due to the magnetic field, the quantization of the energy bands take place. These energy bands are called Landau levels.

We know that Lagrangian for a particle of charge q and mass m moving in electromagnetic field is,

$$L = \frac{m\dot{x}^2}{2} + q\dot{x}.A - q\phi$$

where A is vector potential and ϕ is scalar potential. Therefore, classical equation of motion arising from this Lagrangian is,

$$m\ddot{x} = q(E + \dot{x} \times B)$$

This is Lorentz force law. Now, we know that canonical momentum in presence of gauge field is,

$$p = \frac{\partial L}{\partial \dot{x}} = m\dot{x} + qA$$

And total Hamiltonian is

$$H = \dot{x}p - L = \frac{1}{2m}(p - qA)^2 + q\phi$$

If E=0 and B is a constant magnetic field, then the Hamiltonian becomes,

$$H = \frac{1}{2m}(p - qA)^2$$

Now, we need a gauge potential A, which obeys $\nabla \times A = B$, therefore, we choose $A = (0, xB, 0)$.

we have Hamiltonian as $H = \frac{1}{2m}\left(p_x^2 + (p_y - qBx)^2 + p_z^2\right)$, By using time independent Schrodinger equation, $H\psi = E\Psi$ and inserting $p_y = -i\hbar\frac{\partial}{\partial y}$ and $p_z = -i\hbar\frac{\partial}{\partial z}$,

The energy eigen values comes out to be:

$$E = \hbar\omega_c\left(n + \frac{1}{2}\right) + \frac{\hbar^2 k_z^2}{2m} \quad , \mathrm{n} = 0,1,2....$$

Here n indicates the no. of landau levels. The energy gap between two landau levels is $\hbar\omega_c$.

If the highest landau level is far away from Fermi energy level, then there are no state available for scattering, so magnetoresistance value goes to zero. Here, electron transport in edge state is in ballistic mode. But, as the magnetic field value increases, the highest landau level gets near Fermi energy and there are states available for scattering in the bulk region. This causes the peak in resistance value. So, we get the valleys and peaks in the magnetoresistanc, which is called quantum Shubnikov de-Hass oscillations (SdH). So, when a Landau level crosses the Fermi energy and gets de-occupied, the density of state changes. In all physical quantities, where density of state changes, we get this type of oscillations.

The energy of a given Landau level increases linearly with the magnetic field. This leads to the so-called Landau-Fan. If an electron gas has the electron density n_s, the number $\nu = \frac{n_s}{n_L}$, tells us how many Landau levels are occupied at a given magnetic field at zero temperature. This is called filling factor, where $n_L = \frac{eB}{h}$. Therefore, $\nu = \frac{hn_s}{eB}$ is called the filling factor corresponding to the magnetic field B. At a fixed electron density n_s, the Fermi level of the electron gas oscillates as a function of B. The filling factor ν vs 1/B

plot is termed as the Landau-Fan diagram. The analysis of the non-linear Landau plot can be explained with the help of Roth-Gao-Niu quantization condition [28]. This analysis gives us the information about the phase of the oscillation and deviation from the linearity of the landau plot. The generalized Onsager's relation is given as:

$$n = \frac{f(\varepsilon)}{B} - \gamma_0(\varepsilon) + c(\varepsilon)B + \ldots\ldots$$

Where, the frequency $f(\varepsilon)$ is directly related to the density of the carriers. It is the slope of n vs 1/B landau plot. The second term $\gamma_0(\varepsilon)$ is the phase shift in the zero-field limit and the third term gives the deviation from the linearity in the Landau plot.

In this chapter, we will present a detailed magnetotransport investigation of a EuO-KTO heterostructure, as a function of temperature and in a range of magnetic field (up to 60 T) orientation from perpendicular to parallel direction of this system. By applying this large magnetic field at a very low temperature down to 0.7 K, we were able to attain high amplitude and well-resolved Shubnikov de Has oscillations (SdH). This is the first report of SdH oscillations in a EuO-KTO system at such a magnetic field. Here, multiple 2D conduction subbands were identified and characterized, that have different effective masses and mobilities. The analysis of temperature-dependent out-of-plane SdH oscillations yields average effective masses ranging from m^* ~ 0.77 m_e to 1.81 m_e from the low field to high field range which confirms the occupancy of light and heavy subbands. Similar mass enhancement with a magnetic field was observed for in-plane measurements.

6.2 Experimental Details

Twenty five monolayers of EuO was prepared on TaO_2 terminated (001) KTO substrate using a pulsed laser deposition technique. The deposition temperature was 400 °C and the oxygen partial pressure was 6 x 10^{-8} Torr. The fluence of the laser pulses was 4 J/cm^2 and the repetition rate was 2 Hz. After deposition, the sample was naturally cooled down to room temperature without changing the oxygen partial pressure. Ultrasonic Al-wire bonding was used for electrical contacts. The transport measurement under high magnetic field and low temperatures were carried out at Los Alamos National Laboratory, National High Magnetic Field Laboratory, USA. Simultaneous measurements of longitudinal and Hall resistance were carried in a high pulsed magnetic field (B_{max} = 60 T with a duration of 300 ms) at a constant minimum temperature of 0.7 K. Low-temperature measurement was performed in a ^{3}He

system and dilution refrigerator. For pulsed field measurements, a dc current excitation of 300 μA was applied. To change the angle between magnetic field orientation and the normal direction of the interface, an *in-situ* rotation mechanism was used.

6.3 Results and Discussion

Figure 6.1(a) shows the Hall resistance with a magnetic field up to 60 T at the temperature of 0.7 K. The Hall carrier density and mobility estimated from the linear fit of R_{XY} (B) is n = 2.2 x 10^{14} cm^{-2} and μ = 640 cm^2/Vs. The schematic shows the EuO-KTO sample in Hall geometry, where voltage is measured in the transverse direction of the applied current and magnetic field.

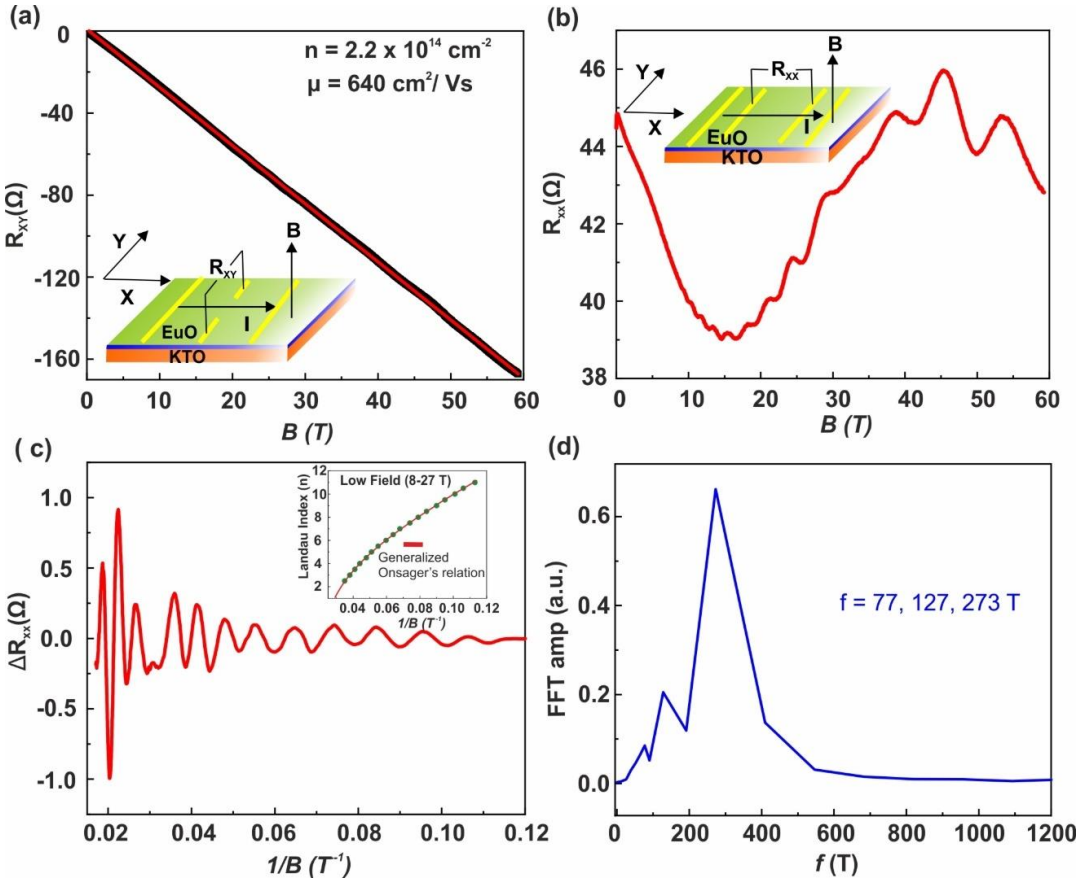

Figure 6.1: (a) Hall resistance (R_{XY}) data with respect to the magnetic field shown with linear fit (red colour). (b) Longitudinal resistance (R_{XX}) with respect to B. In the insets, the schematic of the EuO-KTO sample is shown with Hall and longitudinal geometry. (c) Oscillatory resistance (ΔR_{XX}) with respect to 1/B after subtracting a second and fifth-order polynomial background at low and high fields respectively. In the inset, Landau

plot is shown for low field region fitted with Generalized Onsager's relation. (d) fast Fourier transform (FFT) amplitude as a function of frequency confirms the oscillation having different periods.

Here, to avoid geometric admixture, we measured R_{XY} and R_{XX} for both negative and positive magnetic field direction and calculated the anti-symmetrised R_{XY} and symmetrised R_{XX} by using the formula $R_{xy} = \frac{R_{xy}(+B) - R_{xy}(-B)}{2}$ and $R_{xx} = \frac{R_{xx}(+B) + R_{xx}(-B)}{2}$, respectively. **Figure 6.1(b)** shows the longitudinal resistance with the magnetic field measured at 0.7 K while sweeping the magnetic field oriented perpendicular to the interface. From, this positive magnetoresistance, clear quantum oscillations that are superimposed on it are observed. After subtracting a non-oscillating resistance from the R_{XX} (B) data, the oscillatory resistance ΔR_{XX} is shown with an inverse magnetic field (1/B) in **Fig. 6.1(c)**. The occurrence of the quantum oscillations was ascertained by subtracting a second-order polynomial fit and a fifth-order polynomial fit to the R_{XX}^{Exp} data (raw data) at low and high magnetic field ranges respectively. Here, we observed the quantum Shubnikov de Hass oscillations (SdH) in the subtracted magnetoresistance ($\Delta R_{XX} = R_{XX}^{Exp} - R_{XX}^{Fit}$) as shown in **Fig. 6.1(c).** In the inset, we have shown the Landau-fan diagram fiited with Generalized Onsager's relation for the aperiodic quantum oscillations as discussed above. From this, the frequency of the magnetic oscillation f, phase shift in zero field limit($\gamma_0(\varepsilon)$) and deviation from the linearity $(c(\varepsilon))$ comes out to be 71.76, -4.24 and -0.15 respectively. Similar non-periodic oscillations has been observed recently by KM Rubi et al. in LAO-STO interface [29]. For our system, oscillation starts to develop around 8 T, and as expected, their amplitude starts to increase with the increase in the magnetic field. The fast Fourier transform of ΔR_{XX} vs 1/B is shown in **Fig. 6.1(d),** which indicates three frequencies in these oscillations with periods f_1=77, f_2= 123, and f_3=273 T. So, here we observed 3 electronic sub-bands corresponding to three different frequencies. The total 2D carrier density estimated from these frequencies as

$$n = \frac{2e}{h} \Sigma_i f_i$$, where factor 2 allows the spin degeneracy.

Using the above frequencies value, the carrier density from these SdH oscillations comes out to be n_{SdH}^{2D} = 2.3 x 10^{13} cm^{-2}, that is nearly one order lower than the value measured from Hall n_H = 2.2 x 10^{14} cm^{-2} for this system.

The magnetoresistance of this interface was also measured at different fixed tilt angles ranging from 0° to 90° (out-of-plane to in-plane) at a base temperature of 0.7 K. The tilt angle θ is measured between the normal to the interface and magnetic field (B) direction as illustrated in the schematic of **Fig. 6.2(a).** For in-plane field orientation (θ = 90°), the magnetic field is parallel to the direction of the current, and for out-of-plane measurement (θ = 0°), both are perpendicular.

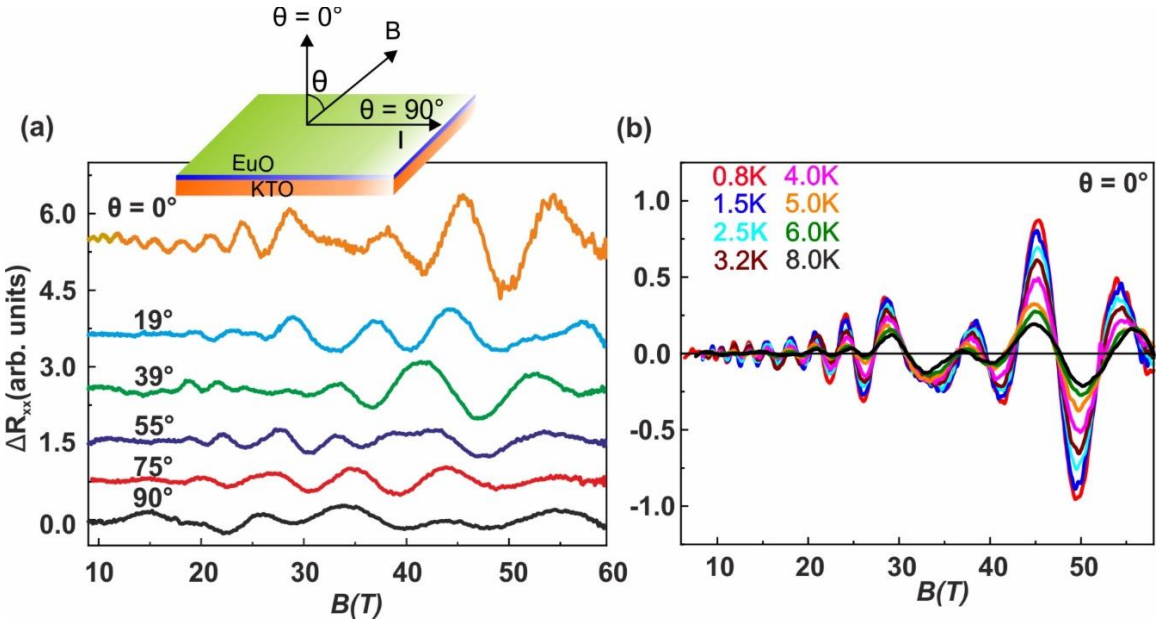

Figure 6.2: Angular and temperature dependence of the quantum oscillations. (a) ΔR_{XX} as a function of magnetic field for different tilt angles (θ = 0° to θ = 90°) at a constant temperature of 0.7 K. θ is the angle between the normal to KTO (001) plane and magnetic field direction as depicted in the inset above of this figure. (b) ΔR_{XX} with respect to the magnetic field for a range of temperatures from 0.8 K to 8 K for out-of-plane measurement (θ = 0°).

This angular dependence measurement was studied to check the dimensionality of the electronic states at the interface. **Figure 6.2(a)** shows the oscillations in the resistance (ΔR_{XX}) with background subtractions at different tilt angles. It is evident that as we go from out-of-plane to in-plane magnetic field orientation, the amplitude of these

oscillations starts to decrease, and also the number of oscillations decreases which indicates the 2D confinement of the the conduction electron at interface. So, the oscillations show a complex angle-dependent evolution. At larger tilt angles, the parallel field couples to the orbital motion of electrons, therefore amplify inter-subband scattering in the quasi-2D electron system. This phenomena is well explained by the Thomas Ihn [30]. The enhancement in scattering rate generates additional Landau-level broadening which decrease the peak density of states that leads to damping of the oscillations amplitude. The small amplitude oscillations that are still visible at higher angles do not depend on the tilt angle i.e.they are only scale with the total magnetic field So, this confirms that apart from the 2D conduction channel , we observed an additional 3D conduction channel parallel to this channel at the interface [29].

Figure 6.2(b) shows the temperature dependent out-of-plane magnetoresistance: the SdH oscillations with a constant background subtraction at selected temperatures. Here, the amplitude of these oscillations increases continuously with increase the magnetic field and lowering of the temperature.

6.3.1 Out-of-plane magneto-transport measurement

In order to get detailed information about the charge carriers from the SdH oscillations, we isolated and analyzed the two oscillating component of ΔR_{XX} , separately in the lower (6-30 T) and higher magnetic field (30-60 T) range. **Figure 6.3(a)** shows the out-of-plane ($\theta = 0°$) temperature-dependent oscillations amplitude in a lower magnetic field up to 30 T. The SdH oscillations are sinusoidal in an inverse magnetic field (1/B) and are described by the general expression (Lifshitz-Kosevich theory [31,32])

$$\Delta R_{xx} = \sum_{i,p} R_{i,p}\, e\, (-\lambda_i T_{D_i}) \frac{\lambda_i T}{sinh((\lambda_i T)} \sin\left(\frac{2\pi p f_i}{B} + \frac{\pi}{4} \right)$$

Where T is the temperature, f_i is the frequency of the oscillations corresponding to the ith subband and p is the harmonic number. R_{ip} is a field and temperature independent amplitude and other amplitude factors contains the term $\lambda = \frac{2\pi^2 p k_B m^*}{\hbar e B}$, from which the effective mass $m^*$and dingle temperature T_D of the charge carriers to be extracted by using the temperature and magnetic field dependence of the signal [32].

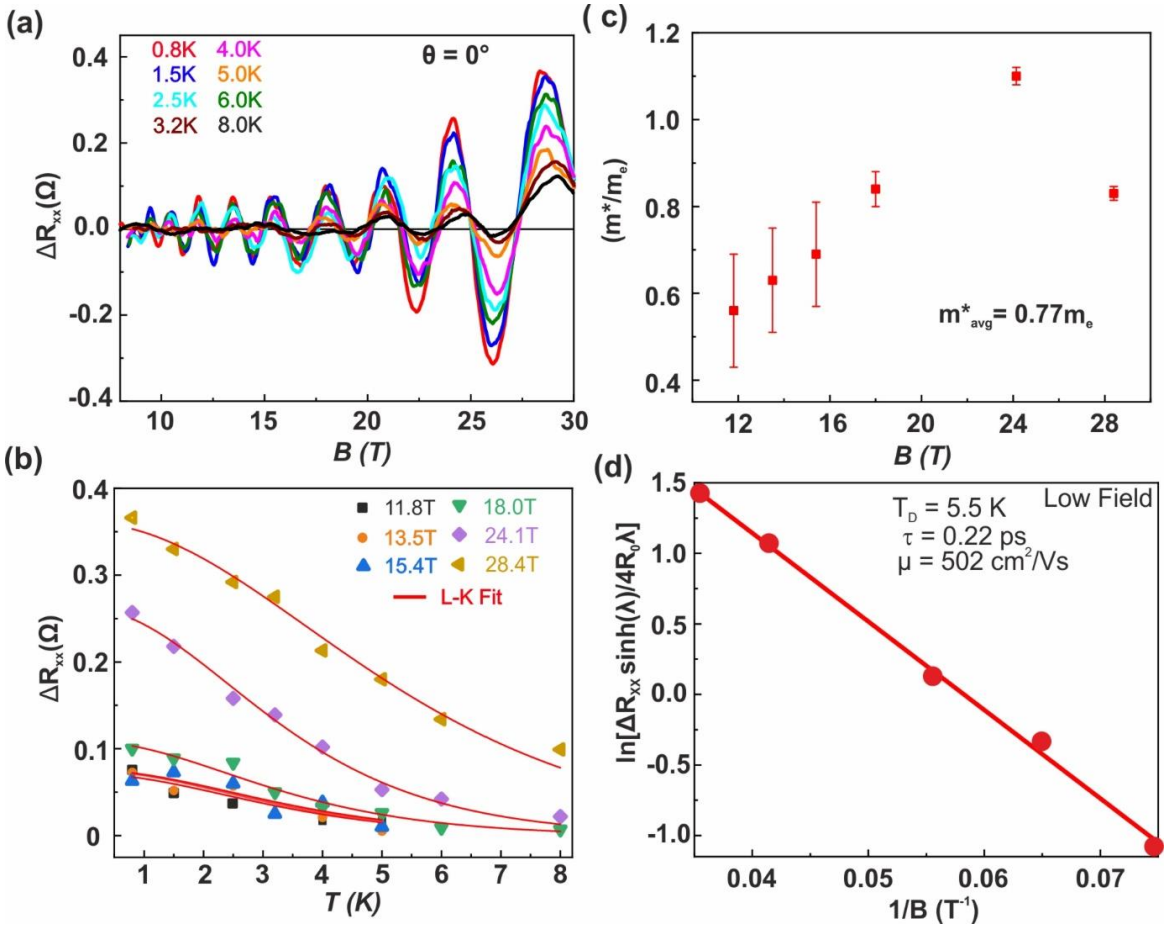

Figure 6.3: (a) Oscillatory resistance amplitude with respect to magnetic field at different temperatures for out-of-plane measurement (b) Temperature dependence of oscillations amplitude for low field (6-30 T). Solid dot points at different magnetic field value represents the experimental data and solid line denotes the data fitted with $\frac{\lambda T}{\sinh(\lambda T)}$. (c) Effective mass ($m^*/m_e$) with error bar as a function of magnetic field B. (d) Dingle plot of the SdH oscillations in the lower field at T =0.8 K.

The effective mass (m^*) was calculated from the temperature-dependent oscillations amplitude at different fields after fitting with the formula derived from Lifshitz-Kosevich theory as shown in **Fig. 6.3(b):**

$$\frac{\Delta R_{xx}(T)}{\Delta R_{xx}(0)} = \frac{\lambda(T)}{\sinh(\lambda(T))}$$

Here, $\lambda(T) = \frac{2\pi^2 k_B m^* T_D}{\hbar e B}$, m* is the effective mass, k_B is the Boltzmann's constant, T_D is the dingle temperature, e is the electric charge and $\hbar$ is reduced plank's constant. **Figure**

6.3(c) shows the effective mass (m^*/m_e) values with the magnetic field B(T). Here, corresponding to different magnetic field values as shown in **Fig. 6.3(b),** the effective mass (m^*) values are calculated with their error bars. **Figure 6.3(c)** suggests that for electrons exhibiting low-field oscillations, the average effective mass comes out to be nearly $m^* = 0.77\ m_e$, where m_e is the mass of the free electron.

The scattering time of the carriers contributing to the SdH oscillations is estimated by the Dingle plot. According to the Lifshitz-Kosevich theory, the oscillations amplitude ΔR_{xx} is given by:

$$\Delta R_{xx} = \frac{4R_0\lambda e^{-\lambda_D}}{\sinh(\lambda)}$$

Where R_0 is the non-oscillatory part of the resistance at zero fields and λ_D is $\frac{2\pi^2 k_B m^* T_D}{\hbar e B}$, T_D is the Dingle temperature, $T_D = \frac{\hbar}{2\pi k_B \tau}$, where τ is the total scattering time. **Figure 3.3(d)** represents the plot of $ln[\Delta R_{xx} sin\ h(\lambda)\ /\ 4R_0\lambda]$ with (1/B) for low field region at 1.5 K. Now for the lighter subband corresponding to low fields range, we have calculated the moblity and scattering time. The value of Dingle temperature and total scattering time comes out to be 5.5 K and 0.22 ps respectively. Also, the mobility can be calculated from here by using $\mu = \frac{e\tau}{m^*}$, that is μ = 502 cm^2 / Vs.

In **Figure 6.4(a),** we have shown the higher amplitude oscillation in high magnetic field regions with different temperatures. In **Figure 6.4 (b)**, the amplitude of the oscillations is plotted with temperature for constant values of the magnetic field. For the higher magnetic field region (30-60 T), we again fitted the temperature-dependent oscillations amplitude by L-K theory discussed above at different magnetic fields and calculated the effective mass. The average effective mass comes out to be 1.81 m_e for the high field range plotted in **Fig. 6.5.**

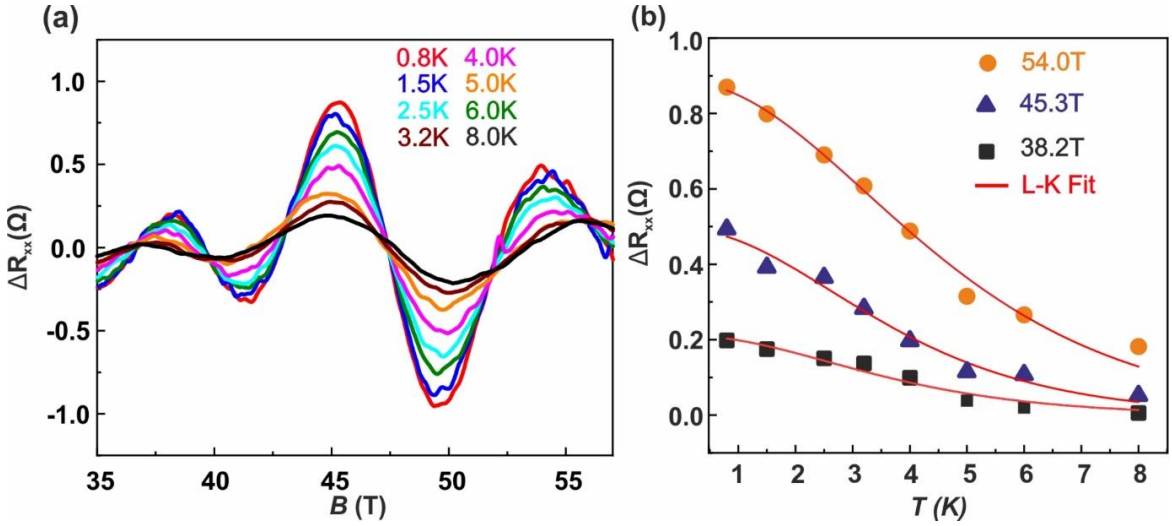

Figure 6.4: (a) ΔR_{xx} with magnetic field for different values of temperatures. (b) ΔR_{xx} as a function of temperature with L-K fitting at different fields.

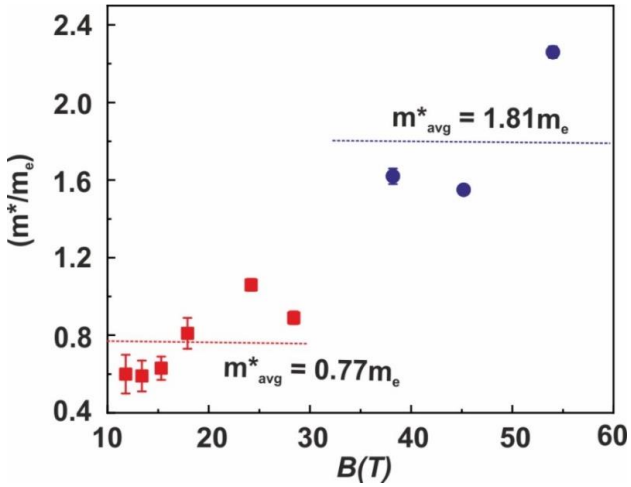

Figure 6.5: The m^*/m_e values as a function of B for low and high magnetic field regions. The average effective mass for the electron in the low magnetic field is 0.77 m_e and that in the high magnetic field range is 1.81 m_e.

The effective mass vs magnetic field behavior is shown in **Fig. 6.5** for the whole range of magnetic field up to 60 T. This figure suggests that for electrons exhibiting low field oscillations, the effective mass is ~0.77 m_e and that for the high field is ~1.81 m_e, where m_e is the mass of the electron. It is found that effective mass is increasing linearly with the increase in the magnetic field value. In earlier reports for semiconductor heterostructures, it is reported that this mass enhancement may be a consequence of the non-parabolicity of the subbands. An increasing magnetic field corresponds to the larger

value of the wave vector in the plane of the 2DEG, and increasing flattening of the energy vs wave vector curve of the lowest subband because of the interaction with higher subbands [33,34].

6.3.2 In-plane magneto-transport measurement

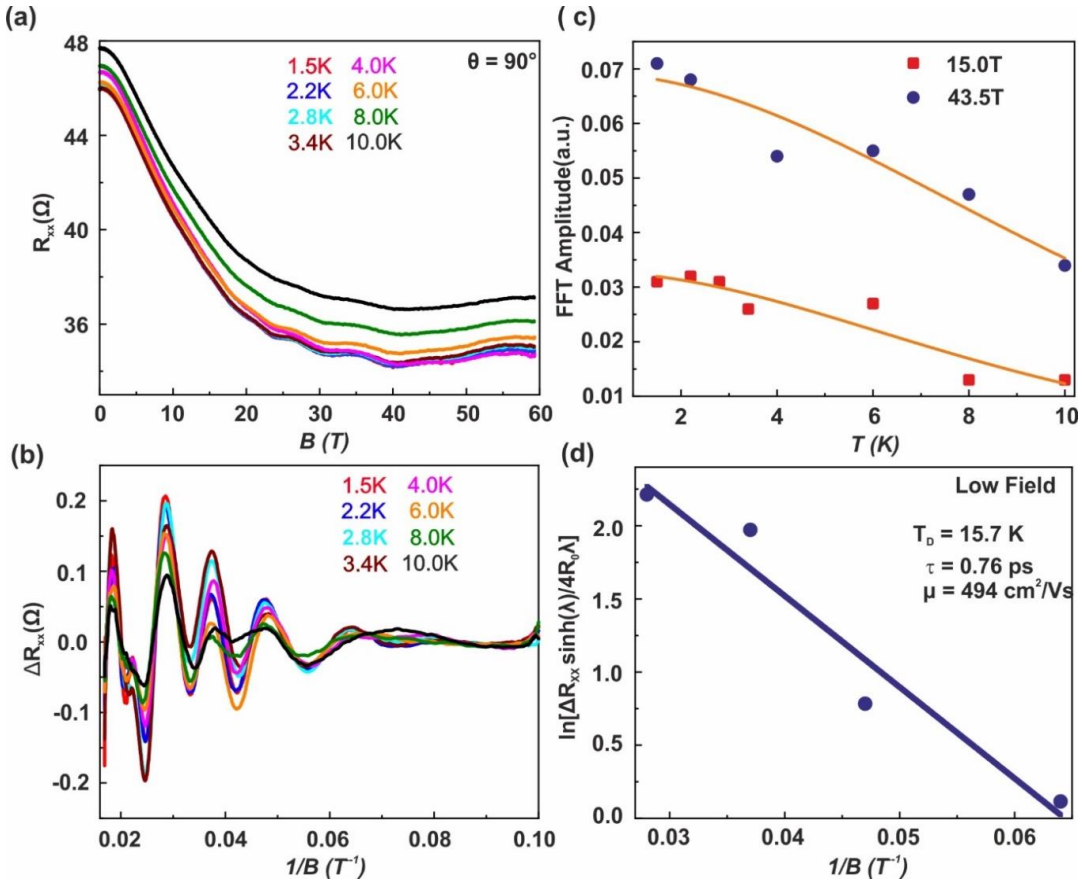

Figure 6.6: In plane temperature dependent data for effective mass calculation. (a) R_{XX} with magnetic field for different temperatures. (b) ΔR_{XX} as a function of 1/B at different temperatures. (c) Temperature dependence of the oscillation amplitudes with values of B_{eff} magnetic field. The solid lines are fit to $\frac{\lambda T}{\sinh(\lambda T)}$. (d) Dingle plot of the SdH oscillation in low magnetic field (10-33 T) range at 1.5 K.

Figure 6.6(a) shows the MR data with magnetic field applied along the direction of the current and measured for different temperatures. Here, the clear quantum oscillations with strongly temperature-dependent amplitudes are apparent when we do the smooth background subtraction as visible in **Fig. 6.6(b).** Here, ΔR_{XX} is plotted with the inverse magnetic field up to 60 T. By fitting the temperature-dependent of FFT peak amplitude to

$\frac{\lambda T}{\sinh(\lambda T)}$, we extracted the carrier effective mass for each subband (**Fig. 6.6(c)**). FFTs were performed over two different overlapping magnetic field ranges, where effective magnetic field B is calculated with $(\frac{1}{2} + (\frac{1}{B_{min}} + \frac{1}{B_{max}}))^{-1}$ for each range. This was repeated for each temperature and effective masses were extracted for both field ranges. The effective mass (m^*) calculated for low (10-33T) and high field (33-60T) ranges are (0.27 ± 0.031) m_e and (0.63 ± 0.021) m_e respectively. Here, we also calculated the scattering time for in-plane SdH oscillations by dingle plot (shown in **Fig. 6.6 (d)**) in the lower magnetic field range (10-33 T) using equations (L-K theory) discussed above in case of out-of-plane measurement. Here, the dingle temperature was calculated to be 15.7 K corresponding to the oscillations at temperature 1.5 K The mobility and scattering time was calculated to be 494 cm^2/Vs and 0.76 ps respectively for the lighter suband in low magnetic field range.

6.4 Conclusions

In summary, we have investigated magneto-transport properties of the cconducting interface of EuO-KTO under ultra-high magnetic fields and at low temperatures for the first time. We observed the 1/B-aperiodic SdH oscillations over the full magnetic field range (8-60 T). The SdH oscillations observed even in the high tilt angles of the magnetic field indicate the coexistence of a 3D conduction channel apart from 2D conduction channel. Observation of multiple frequencies of 2D oscillations confirms the occupancy of multiple subbands with light and heavy electrons. It is found that the effective mass increases linearly with the increase in the magnetic field value. Apart from fine observation of the electronic properties of the KTO-2DEG, this study demonstrates a possible route of studying quantum transport in 2DEG based on 5d-oxides for which creating an epitaxial heterointerface and thereby attaining the high-mobility electron gas is difficult.

Bibliography:

[1]. H. Y. Hwang, Y. Iwasa, M. Kawasaki, B. Keimer, N. Nagaosa and Y. Tokura, *Nat. Mater.*, **11**, 103 (2012).

[2]. S. Stemmer and S. James Allen, *Annu. Rev. Mater. Res.*, **44**, 151 (2014).

[3]. Z. Huang, X. Renshaw Wang, A. Rusydi, J. Chen, H. Yang,and T. Venkatesan. *Adv. Mater.*, **30**, 1802439 (2018).

[4]. P. Noël, F. Trier, L. M. V. Arche, J. Bréhin, D. C. Vaz, V. Garcia, S. Fusil, A. Barthélémy, L. Vila, M. Bibes and J. P. Attane, *Nature*, **580**, 483 (2020).

[5]. A. Ohtomo and H. Hwang, *Nature*, **427**, 423 (2004).

[6]. L. Li, C. Richter, J. Mannhart and R. Ashoori, *Nat. Phys.* **7**, 762 (2011).

[7]. J. A. Bert, B. Kalisky, C. Bell, M. Kim, Y. Hikita, H. Y. Hwang and K. A. Moler, *Nat. Phys.*, **7**, 767 (2011).

[8]. X.R. Liu, D. Choudhury, Y. Cao, M. Karrev, S. Middey and J. Chakhalian. *Appl. Phys. Lett.*, **107**, 191602 (2015).

[9]. K. Zou, S. Ismail-Beigi, K. Kisslinger, X. Shen, D. Su, F. J. Walker and C. H. Ahn. *APL Mater.*, **3**, 036104 (2015).

[10]. H. Zhang, H. Zhang, X. Yan, X. Zhang, Q. Zhang, J. Zhang, F. Han, L. Gu, B. Liu, Y. Chen, B. Shen and J. Sun, *ACS Appl. Mater. Interfaces*, **9**, 11 (2017).

[11]. H. Zhang, Y. Yun, X. Zhang, H. Zhang, Y. Ma, X. Yan, F. Wang, G. Li, R. Li, T. Khan, Y. Chen, W. Liu, F. Hu, B. Liu, B. Shen, W. Han and J. Sun, *Phys. Rev. Lett.*, **121**, 116803 (2018).

[12]. N. Wadehra, R. Tomar, R. M. Varma, R. Gopal, Y. Singh, S. Dattagupta and S. Chakraverty, *Nat. Commun.*, **11**, 874 (2020).

[13]. K. Ueno, S. Nakamura, H. Shimotani, H. Yuan, N. Kimura, T. Nojima, H. Aoki, Y. Iwasa and M. Kawasaki, *Nat. Nanotechnol.*, **6**, 408 (2011).

[14]. C. Liu, X. Yan, D. Jin, Y. Ma, H.-W. Hsiao, Y. Lin, T. M. Bretz-Sullivan, X. Zhou, J. Pearson, B. Fisher, J. S. Jiang, W. Han, J.-M. Zuo, J. Wen, D. D. Fong, J. Sun, H. Zhou and A. Bhattacharya, *Science*, **371**, 716 (2021).

[15]. Z. Chen, Z. Liu, Y. Sun, X. Chen, Y. Liu, H. Zhang, H. Li, M. Zhang, S. Hong, T. Ren, C. Zhang, H. Tian, Y. Zhou, J. Sun and Y. Xie, *Phys. Rev. Lett.,* **126**, 026802 (2021).

[16]. P.D.C. King, R. H. He, T. Eknapakul, P. Buaphet, S.K. Mo, Y. Kaneko, S. Harashima, Y. Hikita, M. S. Bahramy, C. Bell, Z. Hussain, Y. Tokura, Z.X. Shwn, H.Y. Hwang, F. Baumberger and W. Meevasana, *Phys. Rev. Lett.,* **108**, 11 (2012).

[17]. H. Uwe, J. Kinoshita, K. Yoshihiro, C. Yamanouchi and T. Sakudo, *Phys. Rev. B,* **19**, 6 (1979).

[18]. T. Neumann, G. Borstel, C. Scharfschwerdt and M. Neumann, *Phys. Rev. B,* **46**, 17 (1992).

[19]. K.M. Rubi, S. Zeng, F. Bangma, M. Goiran, A. Ariando, W. Escoffier and U. Zeitler, *Phys. Rev. Research, **3***, 033234 (2021).

[20]. V. R. Cooper, *Phys. Rev.* B***, 85***, 23 (2012).

[21]. W. Meevasana, P.D.C. King, R. H. He, S.K. Mo, M. Hashimoto, A. Tamai, P. Songsiriritthigul, F. Baumberger and Z. X. Shen, *Nat. Mater.* ,**10**, 114-118 (2011).

[22]. T. R. McGuire and M. W. Shafer, *J. Appl. Phys.* ,**35**, 984 (1964).

[23]. P. Wachter Helv, *Phys. Acta.,* **37**, 637 (1964).

[24]. M. J. Freiser, F. Holtzberg, S. Methfessel, G. D. Pettit, M. W. Shafer and J. C. Suits. Helv, *Phys. Acta*, **41**, 832 (1968).

[25]. J. H. Greiner and G. J. Fan, *Appl. Phys. Lett*, **9**, 27 (1966).

[26]. K. Ahn, *J. Appl. Phys.,* **39**, 5061 (1968).

[27]. A. Schmehl, V. Vaithyanathan, A. Herrnberger, S. Thiel, C. Richter, M. Liberati, T. Heeg, M. Rockerath, L. F. Kourkoutis, S. Muhlbauer, P. Boni, D. A. Muller, Y. Barash, J. Schubert, Y. Idzerda, J. Mannhart and D. G. Schlom, *Nature Mater.*, **6**, 882 (2007).

[28]. J. N. Fuchs, F. Piéchon and G. Montambaux, *SciPost Phys*., **4**, 024 (2018).

[29]. Km Rubi, J. Gosteau , R. Serra , K. Han , S. Zeng , Z. Huang , B. Warot-Fonrose , R. Arras , E. Snoeck , Ariando, M. Goiran and W. Escoffier, *npj Quantum Materials* , **5** , 9 (2020).

[30]. Thomas Ihn, Oxford University Press, *Oxford*, (2010).

[31]. D. Shoenberg, Cambridge University Press, (1984).

[32]. I. M. Lifshitz and A. M. Kosevich, *Sov. Phys. JETP* **2**, 636 (1956).

[33]. E. D. Palik, S. Teitler, and R. F. Wallis, *J. Appl. Phys.*, **32**, 2132 (1961).

[34]. T. E. Whall, A. D. Plews, N. L. Mattey, P. J. Phillips, and U. Ekenberg, *Appl. Phys. Lett*., **66**, 2724 (1995).

Chapter 7

Summary of thesis work and Future Scope

7.1 Summary

The well-known and most widely explored oxide interface is LAO-STO heterointerface that was discovered in 2004 to exhibit high mobility quasi two-dimensional electron gas. It shows various exotic properties such as superconductivity, enhanced Rashba spin-orbital coupling, magnetism, strong electric field effect and so on. The transport behaviour at the conducting interface of such oxides is controllable by using various external stimuli such as light irradiation, electrostatic back gating, by using both light and back gate simultaneously, external magnetic field and so on. These external perturbations have shown its potential in unravelling the emergent phenomena at complex oxide interface.

In the first chapter, we have discussed that how the oxide electronics is dominating with time over the conventional semiconductor electronics and why the thin film technology is important for the future optoelectronics and spintronic devices. Here, we have also given a brief introduction of all materials and interfaces used in this thesis work. Next, we have discussed that how we can tune the interfacial properties of these oxides with the help of light and electrostatic gate comparing with the previous studies. In the next chapter of this thesis, we have discussed about all the instrumentation and experimental techniques that were used to carry out the research work. We have given a brief overview of the pulsed laser deposition technique (PLD) assisted with RHEED, for the growth and control of the thin film. We have also briefly discussed all the characterization techniques such as AFM, RHEED, PPMS etc. Apart from these, we have also given the details of all other experimental tools used in light and back gating study such as four probe cryogenic station, source meter, multimeter and DPSS lasers. In chapter three of the thesis, we have focussed on the optimization and standardization of the pulsed laser deposition (PLD) system. We have done the combinatorial study, where multiple samples can be grown with different growth parameters in a single shot method. Thin film growth using PLD hinges on various parameters that decide the

composition, structure, quality, and finally the physical properties of the films, interfaces, and superlattices. Here, we have demonstrated that how the growth conditions inside the chamber during the growth can be judged from outside by combining *in-situ* and *ex-situ* techniques. In the next chapter, the highly spin-polarized ferromagnetic semiconductor, EuO has been examined as a potential candidate for spintronics and optoelectronic applications and is chosen as a depositing material on KTO substrate. We optimized the EuO-KTO interface and then studied its opto-electrical properties at different temperature. We have shown how the photoconductivity changes with temperature, carrier density, and wavelength of light. The sample with lower carrier density, shows the maximum photo-response as compared to sample with higher carrier density. The maximum change in resistance was observed to be nearly 82% at 76 K temperature. The larger and faster photo-response behaviour was observed at lower temperature that fits with a single exponential function as compared to room temperature where it was fitted by double exponential function.

In the next chapter of this thesis, we have investigated the combined effect of light irradiation and electrostatic back gate for EuO-KTO conducting interface at room temperature. Here, we have observed the unusual tuning in the conductivity, where nearly 120000 % change in resistance is observed with the combined effect of light and back gate voltage. Also, the higher resistance state can be change down within seconds to its lower initial state on application of light only. We found that maximum change is observed in case of blue light, its energy is nearby to the band gap of KTO substrate (~ 3.5 eV). Our results give an important clue to design future generation solar cells and holographic storage media devices.

In the last and final work of the thesis, we have presented the magneto-transport data of the EuO-KTO conducting interface with magnetic field up to 60 T. Here, the clear quantum oscillations (SdH) with high amplitude were observed at low temperature and high magnetic field value. These oscillations were studied at different tilt angles and it was found that an additional 3D conduction channel exist apart from the 2D conduction channel. The multiple frequencies of 2D oscillations confirms the occupancy of multiple sub-bands with light and heavy electrons. It was also found that effective mass of the electrons increases linearly with the increase in magnetic field.

7.2 Future Scope

With the advancement in the field of technology, there is huge scope to utilize the exotic properties of these conducting interfaces of oxide materials for device applications in our daily life. Although there are vast challenges to realize the practical applications of these 2DEG-based oxide electronics and optoelectronic devices. In this thesis, the opto-electrical properties are studied on the conducting interface of EuO-KTO heterostructure. Apart from this, there are other KTO-based heterostructures where conducting interfaces has been realized such as $LaTiO_3$-KTO, LVO-KTO, and LAO-KTO. These all conducting interfaces are new and not well explored with the light and back gate application. So far, the STO based heterostructures are mainly explored with effect of light and electrostatic gate. In our work, we have explored the conducting interface of EuO-KTO with external stimuli such as light, back gate, magnetic field and combined effect of light and back gate. However, there is still a great need to completely examine this interface from the perspectives of experimental as well as theoretical modelling in order to understand how the mechanism of charge dynamics is changing in response to these external stimuli. The large persistent photoconductivity observed at low-temperature need to explore theoretically to reveal the mechanism of the charge carriers at EuO-KTO interface. Also, to find the exact origin of the conductivity and to study the band structure of this interface, further measurements can be done such as scanning transmission electron microscopy (STEM) and angle resolved photoemission spectroscopic (ARPES). There are couple of reports on KTO based heterostructure that have been studied with joint effect of light and back gate. So, there is a huge scope to explore the KTO based interfaces or heterostructures with back gating and light illumination.

The combined effect of light and back gate on this interface can be explored at lower temperature. We can also see the photo-response behaviour of this interface with change in the different growth parameters such as fluence, oxygen partial pressure and temperature, from there we can observe how the carrier dynamics is changing with different conditions.

Numerous perovskite oxides with various physical characteristics allow for countless combinations, which pave the path for all-oxide electrical devices with improved functions in the future. So, the superlattices of EuO/LVO/KTO oxides can be explored to realize different exotic properties. The high mobility 2DEG at LVO-KTO interface was

recently discovered and holds large number of exciting features such as Planar Hall effect, Large Rashba spin-orbital coupling, anisotropic magnetoresistance etc. So, the combination of EuO and LVO superlattices can be tuned with the light, back gate and joint effect of both. Also, due to the large photovoltaic properties of EuO-KTO interface, the dynamical behaviour of the carrier at this interface can be explored using ultrafast spectroscopy.

The ability of these heterostructure to be used in device applications may be further increased by studying the tuning of the spin-orbit coupling strength as a function of charge carriers and examining how this affects the Rashba physics of the heterostructure.

The magneto-transport study can be done with the effect of light illumination at different temperatures. Recently, the quantum oscillations were observed at LAO-STO interface with the illumination of light. So, for our system also, we have the possibility to explore these high amplitude oscillations under the effect of light.

Simple cubic transition metal perovskite oxides with strong spin-orbit coupling are a rich source of newly discovered features that have begun to distinguish them as potential replacement materials for electronic device applications. They offer a wide range of alternative processes to accomplish a certain goal in addition to being alternative materials for use in various applications, which can revolutionise the entire sector if they are used further. This increases the degrees of freedom to tweak the required attributes. Therefore, as oxides constitute the foundation of the upcoming generation of electronic gadgets, they should be used to the utmost extent possible.

List of Publications

(A) Included in the thesis

(a). Published

(1). **Manish Dumen**, Ripudaman Kaur, Saveena Goyal, Ruchi Tomar, Neha Wadehra and Suvankar Chakraverty. ***Crystal Research and Technology***, 56, 2000186 (2021).

(2). **Manish Dumen**, Ajit Singh, Saveena Goyal, Chandan Bera and Suvankar Chakraverty. ***The Journal of Physical Chemistry C***, 125, 28 (2021).

(b). Not published

(1). **Manish Dumen**, Ajit Singh, Chandan Bera and Suvankar Chakraverty, Light-enhanced unusual gating effect at conducting interface of EuO-$KTaO_3$.

(2). KM Rubi, **Manish Dumen**, Suvankar Chakraverty, Mun K. Chan, Neil Harrison. "High-field magneto-transport in a spin-polarized quasi-two-dimensional electron gas at EuO-$KTaO_3$ interface.

(B) Not included in thesis

(1). Anshu Gupta, Harsha Silotia, Anamika Kumari, **Manish Dumen**, Saveena Goyal, Ruchi Tomar, Neha Wadehra, Pushan Ayyub and Suvankar Chakraverty. ***Advanced Materials***, 34, 2106481 (2022).

Research Conferences and Workshops

1. Presented a poster in "Emergent phenomena in Quantum Materials (E-QMAT) 2022" organized by Department of Physics, IIT Roorkee held from 12-14th October, 2022.
2. Participated in "PNM-II: Conference on Physics of Nano-Materials" organized by QMaD unit, INST Mohali held from 7-8th July 2022.

3. Presented a research paper in “International Conference on Materials-Properties, Measurements and Applications (ICMPMA 2022)” organized by Fatima Mata National College, Kerala held from 9-13th May 2022.

4. Presented a poster in “Indo Japan workshop on interface phenomena for Spintronics (IJW-IPS 2022)” organized by National Institute of Science Education and Research, Bhubaneshwar held from 8-10th March, 2022.

5. Attended a training programme titled “Nanophotonics: Materials, Devices and Applications” organized by Central Institute of Petrochemicals Engineering and Technology (CIPET) held at Bhubaneshwar from 6-7th February 2021.

6. Participated in “10th Chandigarh Science Congress” organized by Panjab University, Chandigarh from 29th February– 2nd March 2016.